Technical Physics Letters, Vol. 31, No. 4, 2005, pp. 267–269. Translated from Pis'ma v Zhurnal Tekhnicheskoĭ Fiziki, Vol. 31, No. 7, 2005, pp. 1–6.

Application of the Darboux Transform to Spectral Problems in Ocean Acoustics

A. I. Gudimenko and A. D. Zakharenko

Pacific Institute of Oceanology, Far-Eastern Division, Russian Academy of Sciences, Vladivostok, Russia

e-mail: secret@poi.dvo.ru

Received September 14, 2004

Abstract—We propose a generalization of the *n*-order Darboux transform, which can be applied to solving spectral problems in ocean acoustics in cases when the medium can be considered stratified with respect to density. For a second-order Darboux transform with the boundary conditions characteristic of a single-layer shallow sea model, conditions are determined under which the spectra of the initial and transformed spectral problems coincide. It is demonstrated that, within the framework of this model, it is possible to use the *n*-order Darboux transform for constructing sound velocity profiles admitting exact solutions. *© 2005 Pleiades Publishing, Inc.*

The Darboux transform is widely used in quantum mechanics for constructing potentials admitting exact solutions of the Schrödinger equation [1]. Unfortunately, this approach still does not find proper application in one-dimensional wave acoustics, despite evident analogy of the corresponding spectral problems. This refers, in particular, to the one-dimensional wave acoustics of the ocean, where, in the absence of flows, the role of the spectral problem operator is played by the Helmholtz operator:

$$L_0 := \rho\frac{d}{dz}\frac{1}{\rho}\frac{d}{dz} + k_0^2 \quad \left(k_0 := \frac{\omega}{c_0}\right), \tag{1}$$

where $\rho(z)$ is the density, $k_0(z)$ is the acoustic wavenumber, ω is the circular frequency, and $c_0(z)$ is the velocity of sound. The boundary conditions in the general case are selected in the arbitrary impedance form, while, in the case of a discrete-stratified medium, they are formulated as the internal boundary conditions [2]. It should be emphasized that the difference between these acoustic spectral problems and those considered in quantum mechanics consists in stratification of the medium with respect to the density and in the more general boundary conditions.

In this paper, the *n*-order Darboux transform for the Schrödinger equation [3] is generalized to the case of operators of type (1). Under the boundary conditions characteristic of spectral problems of shallow sea acoustics, the sound velocity profiles that admit exact solutions are constructed. It is demonstrated that the proposed *n*-order transform can be used for modeling the sound velocity profiles typical of shallow sea conditions, including the profiles with a "fine" structure. For a second-order Darboux transform, it is shown that two families of exactly solvable sound velocity profiles exist for which the spectra of the initial and transformed spectral problems coincide.

Let us define the *n*-order Darboux transform of operator L_0 as follows. Using the Liouville transform [4] (in our case, this operator reduces to the simple substitution $\varphi \longrightarrow \varphi/\sqrt{\rho}$ for functions from the domain of definition of L_0), we convert L_0 to the Helmholtz operator with a constant density. Then, let us apply the usual *n*-order Darboux transform [3] to the obtained Helmholtz operator. Finally, we return to the initial density in the resulting operator with the aid of the inverse Liouville transform.

The operator defined above and denoted L_n has the same form (1), but with a new acoustic wavenumber k_n. This wavenumber and the eigenfunctions φ_{n_ξ} of operator L_n can be represented as

$$k_n^2 = k_0^2 + 2D^2\ln\frac{\{\varphi_{\eta_1}, \ldots, \varphi_{\eta_n}\}}{\rho^{n/2}}, \tag{2}$$

$$\varphi_{n_\xi} = \frac{\{\varphi_\xi, \varphi_{\eta_1}, \ldots, \varphi_{\eta_n}\}}{\{\varphi_{\eta_1}, \ldots, \varphi_{\eta_n}\}}, \tag{3}$$

where φ_ξ, φ_{η_1}, …, φ_{η_n} are the eigenfunctions of operator L_0 corresponding to the eigenvalues ξ^2, η_1^2, …, η_n^2, respectively; braces denote the Wronskian of the enclosed functions.

Thus, the *n*-order Darboux transform of operator L_0 is determined by *n* eigenfunctions φ_{η_1}, …, φ_{η_n}. Following [3], we call these quantities the transformation functions. For ρ = const, formulas (2) and (3) reduce to the conventional representations [3].

1063-7850/05/3104-0267$26.00 © 2005 Pleiades Publishing, Inc.

The transformation functions are, generally speaking, the arbitrary eigenfunctions of operator L_0, and their selection is related neither to the initial spectral problem nor to the problem for the transformed operator. If the boundary conditions are fixed, the spectra of the initial and the new operator are different in the general case. However, the conservation of the spectrum is frequently among important conditions. Below, we consider how this possibility can be realized for a second-order Darboux transform and a spectral problem with the domain of definition of the eigenfunctions $z \in [0, h]$ and the boundary conditions $\varphi_\xi = 0$ and $D\varphi_\xi(h) = 0$.

Essentially, we have to find the conditions for φ_{η_1} and φ_{η_2} under which $\varphi_{2\xi}$ and φ_ξ simultaneously meet the boundary conditions. At the upper boundary, we have $\varphi_{2\xi} = \varphi_\xi = 0$. Calculating the Wronskian

$$\{\varphi_\xi, \varphi_{\eta_1}, \varphi_{\eta_2}\} = \begin{Vmatrix} \varphi_\xi & \varphi_{\eta_1} & \varphi_{\eta_2} \\ \varphi'_\xi & \varphi'_{\eta_1} & \varphi'_{\eta_2} \\ (\xi^2 - k_0^2)\varphi_\xi & (\eta_1^2 - k_0^2)\varphi_{\eta_1} & (\eta_2^2 - k_0^2)\varphi_{\eta_2} \end{Vmatrix},$$

we obtain $\varphi_{\eta_1}(0)\varphi_{\eta_2}(0) = 0$. At the lower boundary, we have $D\varphi_{2\xi} = 0$ and $D\varphi_\xi = 0$. Taking into account that

$$D\varphi_{2\xi} = \frac{D\{\varphi_\xi, \varphi_{\eta_1}, \varphi_{\eta_2}\}}{\{\varphi_{\eta_1}, \varphi_{\eta_2}\}} - \frac{\{\varphi_\xi, \varphi_{\eta_1}, \varphi_{\eta_2}\}D\{\varphi_{\eta_1}, \varphi_{\eta_2}\}}{\{\varphi_{\eta_1}, \varphi_{\eta_2}\}^2},$$

the former condition is automatically fulfilled, provided that $D\{\varphi_{\eta_1}, \varphi_{\eta_2}\}(h) = 0$ and $D\{\varphi_\xi, \varphi_{\eta_1}, \varphi_{\eta_2}\}(h) = 0$. Calculating these derivatives in terms of the representation

$$D\{\varphi_{\eta_1}, \varphi_{\eta_2}\} = \begin{Vmatrix} \varphi_{\eta_1} & \varphi_{\eta_2} \\ (\eta_1^2 - k_0^2)\varphi_{\eta_1} & (\eta_2^2 - k_0^2)\varphi_{\eta_2} \end{Vmatrix},$$

$$D\{\varphi_\xi, \varphi_{\eta_1}, \varphi_{\eta_2}\} = \begin{Vmatrix} \varphi_\xi & \varphi_{\eta_1} & \varphi_{\eta_2} \\ \varphi'_\xi & \varphi'_{\eta_1} & \varphi'_{\eta_2} \\ (\xi_2^2 - k_0^2)\varphi'_\xi & (\eta_1^2 - k_0^2)\varphi'_{\eta_1} & (\eta_2^2 - k_0^2)\varphi'_{\eta_2} \end{Vmatrix},$$

we obtain $\varphi_{\eta_1}(h)\varphi_{\eta_2}(h) = 0$ and $D\varphi_{\eta_1}(h)D\varphi_{\eta_2}(h) = 0$. Thus, the necessary conditions are as follows:

$$\varphi_{\eta_1}(0)\varphi_{\eta_2}(0) = 0, \quad \varphi_{\eta_1}(h)\varphi_{\eta_2}(h) = 0,$$
$$D\varphi_{\eta_1}(h)D\varphi_{\eta_2}(h) = 0.$$

As can be seen, the requirement of conservation of the spectrum in the case of a second-order Darboux transform leads to two families of the transformation functions determined by the conditions

$$\varphi_{\eta_1}(0) = 0, \quad \varphi_{\eta_1}(h) = 0, \quad D\varphi_{\eta_2}(h) = 0, \qquad (4)$$

$$\varphi_{\eta_1}(0) = 0, \quad D\varphi_{\eta_1}(h) = 0, \quad \varphi_{\eta_2}(h) = 0. \qquad (5)$$

It should be noted that the aforementioned "conservation of the spectrum" is rather conditional. Indeed, in the case of the n-order Darboux transform, the requirement that $\varphi_{n\xi}$ and φ_ξ satisfy the same boundary conditions ensures that the spectrum is retained only to within a finite (not exceeding n) number of points. More precisely, the spectrum is conserved if the points $\eta_1^2, \ldots, \eta_n^2$ do not belong to this spectrum; otherwise, the conservation can be violated at these points [1, 3]. In particular, for a second-order Darboux transform, the complete conservation of the spectrum takes pace under condition (4), while a shift of the spectral value is observed under condition (5).

Now, we will present the results of numerical calculations of the exactly solvable sound velocity profiles for a single-layer shallow sea model with $z \in [0, h]$ stratified with respect to density $\rho(z) = \rho_0\exp(2\gamma z)$, where ρ_0 and γ are the constants obtained via second- and fourth-order Darboux transforms of the profile $c_0 = \text{const}$. We consider only the profiles for which the spectrum is conserved. The boundary conditions of the corresponding spectral problems are formulated as $\varphi_\xi(0) = 0$ and $D\varphi_\xi(h) = 0$. It should be noted that, in the absence of the conservation requirement, the possibilities of using the Darboux transform for constructing the solvable sound velocity profiles are much broader.

The transformation functions are as follows:

$$\varphi_{\eta_i}(z) = e^{\gamma z}\cos(k_{\eta_i} z + \alpha_i), \quad i = 1, \ldots, n,$$

where the coefficients k_{η_i} satisfy the relation $-k_{\eta_i}^2 + k_0^2 - \gamma^2 = \eta_i^2$ and $\alpha_i \in [0, 2\pi]$. The eigenfunctions φ_{ξ_j} of the initial spectral problem have the same form, with $\alpha_i = \pi/2$ and k_{ξ_j} such that

$$\tan(k_{\xi_j} h + \pi/2) = \gamma/k_{\xi_j}, \quad j = 1, 2, \ldots . \qquad (6)$$

The numerical calculations have been performed for a depth of $h = 100$ m and a frequency varied from 50 to 150 Hz. The initial velocity of sound was varied from 1460 to 1565 m/s; the coefficient γ was changed from 0 to 0.001 m^{-1}; and the η_i^2 values were selected in the interval corresponding to several initial modes of the initial spectral problem.

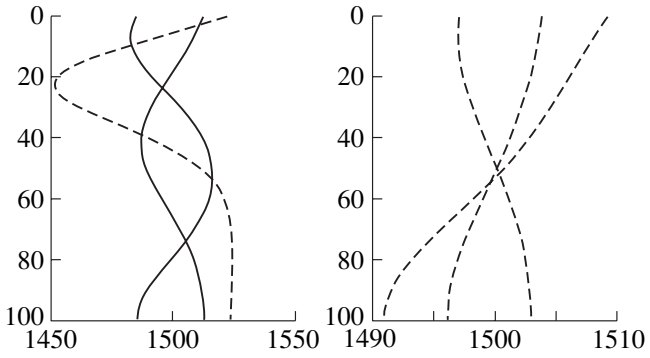

Fig. 1. Sound velocity profiles calculated using the second-order Darboux transform with $\gamma = 0.001$ m^{-1}, $c_0 = 1500$ m/s, and $\omega = 50$ Hz.

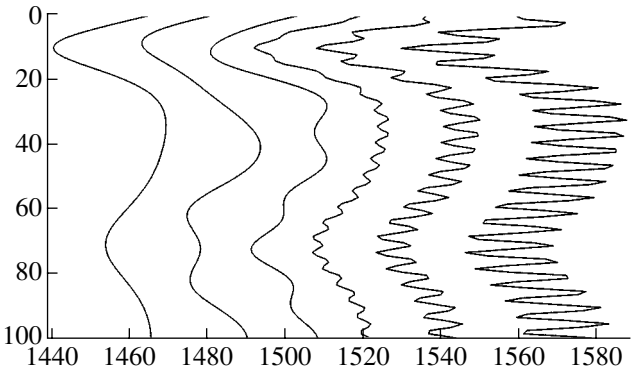

Fig. 2. "Fine" structure in the sound velocity profiles obtained via fourth-order Darboux transformation of the profiles with c_0 = 1460, 1480, 1500, 1515, 1535, and 1565 m/s for $\gamma = 0.001$ m^{-1} and $\omega = 150$ Hz.

Figure 1 shows the sound velocity profiles characteristic of the second-order Darboux transform in the case with η_i^2 corresponding to the first mode of the initial spectral problem for L_0 with the left and right boundary conditions (4) and (5), respectively. An increase in this parameter leads to a growth in the number of extrema on the profile. Note that the profiles exhibit different sensitivity with respect to a change in γ: dashed profiles are more sensitive to this parameter.

Figure 2 illustrates another interesting feature of the *n*-order Darboux transform, namely, the possibility of modeling a "fine" structure of the sound velocity profile. This structure appears when a given profile is perturbed by superposition of another profile with a greater number of oscillations. The initial profile is depicted first from the left. Here, the transformation functions were selected as follows: φ_{η_1} and φ_{η_2} satisfied condition (4) with fixed values of the parameters, while φ_{η_3} and φ_{η_4} satisfied condition (5), in which the free parameters were varied. In particular,

$$\varphi_{\eta_1}(z) = e^{\gamma z}\sin(2\pi z/h), \quad \varphi_{\eta_3}(z) = e^{\gamma z}\sin(k_{\xi_j} z),$$

$$j = 1, 4, 6, 21,$$

where k_{ξ_j} is found from Eq. (6).

In conclusion, it should be noted that the Darboux transform offers a simple and effective method for constructing solvable sound velocity profiles in model problems and for approximating real profiles by exactly solvable ones.

REFERENCES

1. B. N. Zakhar'ev and V. M. Chabanov, *Friendly Quantum Mechanics: New Status of the Theory in the Inverse Problem Approach* (Institute of Computer Research, Moscow, 2002) [in Russian].
2. L. M. Brekhovskikh and O. A. Godin, *Acoustics of Layered Media* (Nauka, Moscow, 1989; Springer-Verlag, New York, 1990).
3. V. G. Bagrov and B. F. Samsonov, Teor. Mat. Fiz. **104**, 356 (1995).
4. B. M. Levitan and I. S. Sargsjan, *Sturm-Liouville and Dirac Operators* (Nauka, Moscow, 1988; Kluwer, Dordrecht, 1991).

Translated by P. Pozdeev

Technical Physics Letters, Vol. 31, No. 4, 2005, pp. 270–273. Translated from Pis'ma v Zhurnal Tekhnicheskoĭ Fiziki, Vol. 31, No. 7, 2005, pp. 7–13.

Maximum Size of a Gas Bubble in the Regime of Automodel Pulsation

A. O. Maksimov

Pacific Institute of Oceanology, Far-Eastern Division, Russian Academy of Sciences, Vladivostok, Russia
e-mail: maksimov@poi.dvo.ru

Received October 4, 2004

Abstract—A complete symmetry group for the Rayleigh equation used as a basis for the theoretical description of acoustic cavitation is found, which allows the form of an external drive giving rise to internal dynamic symmetry in gas bubble pulsation to be determined. The efficiency of bubble extension under the action of a periodically prolonged scale-invariant external acoustic field is studied. It is demonstrated that this action, having the form of a train of shock waves, does not lead to a significant decompression. This circumstance significantly reduces the probability of damaging biological tissues as a result of cavitation caused by the extension phase of a shock pulse. © *2005 Pleiades Publishing, Inc.*

Theoretical analysis of the acoustic cavitation is based on the Rayleigh equation describing the behavior of a gas bubble in an external acoustic field:

$$R\ddot{R} + \frac{3}{2}\dot{R}^2 + \frac{P_0}{\rho_0}\left[1 - \left(\frac{R_0}{R}\right)^{3\gamma}\right] = \frac{P(t) - P_0}{\rho_0}. \quad (1)$$

Here, P_0, P and R_0, R are the equilibrium and current values of the pressure in the liquid medium and the bubble radius, respectively; ρ_0 is the liquid density; γ is the polytrope exponent. Traditionally, cavitation phenomena have been studied for the external field in the form of a harmonic signal $P(t) = P_0 - P_m\cos(\omega t)$, where P_m and ω are the amplitude and frequency of the acoustic field.

Previously, a complete symmetry group for the Rayleigh equation was found, which allowed the form of an external action giving rise to internal dynamic symmetry in gas bubble pulsation to be determined [1, 2]. In particular, scale invariance takes place when the external pressure has the following form: $P(t) = P_m[t_0/(t + t_0)]^{6\gamma/(2+3\gamma)}$, where t_0 is the fall time. Then, a quite natural question arises concerning the efficiency of the bubble extension and collapse under exposure to a periodically prolonged scale-invariant external field,

$$P(t) = \sum_{k=0}^{\infty} P_m\left[\frac{t_0}{(t - Kt) + t_0}\right]^{6\gamma/(2+3\gamma)} \times [\theta(t - kT) - \Theta(t - (k+1)T)] \quad (2)$$

(T is the prolongation period), in comparison to the harmonic case.

Periodically prolonged external field (2) may correspond to a real pressure field in an experimental cell only provided that the total flux over the period is zero [3]:

$$\int_t^{t+T} dt'[P(t') - P_0] = 0. \quad (3)$$

This condition established a certain relationship between the pressure drop P_m at the leading edge, the period T, and the characteristic fall time t_0:

$$\frac{P_m}{P_0} = \frac{3\gamma - 2}{3\gamma + 2}\left(\frac{T}{t_0}\right)[1 - (1 + T/t_0)^{-(3\gamma-2)/(3\gamma+2)}]^{-1}. \quad (4)$$

Relation (4) is graphically illustrated in Fig. 1 for the

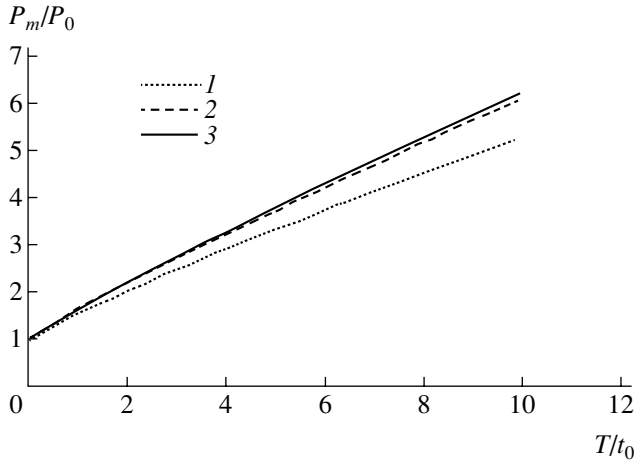

Fig. 1. Plots of the relative pressure drop at the leading edge versus prolongation period according to relation (4) for $\gamma = 1$ (*1*), 4/3 (*2*), and 1.4 (*3*).

1063-7850/05/3104-0270$26.00 © 2005 Pleiades Publishing, Inc.

polytrope exponent values $\gamma = 1$, 4/3, and 1.4 (curves *1*–*3*, respectively).

It should be noted that expression (2) reduces in the limiting cases to the well-known objects of nonlinear acoustics. In particular, for $T/t_0 \ll 1$ we deal with a sawtooth wave with the pressure varying over a period ($0 \le t \le T$) as

$$P(t) \approx P_0[1 - (6\gamma/3\gamma + 2)(t - T/2)t_0^{-1}]. \qquad (5)$$

For $T/t_0 \ge 1$, expression (2) describes a sequence of shock waves similar to those used in shock wave lithotripsy [4]. The character of the nonlinear pulsation of a bubble depends on the shape of the envelope of a high-power ultrasonic wave. This dependence can be studied in the general case only by numerically solving the Rayleigh equation. The results of such a comparative analysis for the cases of harmonic, symmetric, and asymmetric sawtooth waves were reported in [5]. In the present study, the system is analyzed predominantly by analytical methods.

If the period is shorter than the fall time (i.e., $T/t_0 \ll 1$), the wave amplitude in (5) is also small, and we can find an exact solution of a linearized Rayleigh equation. Following the method developed in [6], we obtain

$$R = R_0 + \Delta R, \quad \xi = \dot{R} + i\Omega_0 \Delta R, \quad \frac{d\xi}{dt} - i\Omega_0 \xi = F,$$

$$F = \frac{6\gamma P_0}{\rho_0 R_0 (2 + 3\gamma)} \sum_{k=0}^{\infty} \frac{[t - (k + 1/2)T]}{t_0}$$

$$\times \{\Theta(t - kT) - \Theta[t - (k + 1)T]\},$$

$$\xi(t) = e^{i\Omega_0 t}\left[\int_0^t dt' F(t') e^{-i\Omega_0 t'} + \xi_0\right]$$

$$= \frac{6\gamma P_0}{\rho_0 R_0 (2 + 3\gamma)} e^{i\Omega_0 (lT + \Delta t)}\left\{\frac{e^{-il\Omega_0 T} - 1}{e^{-i\Omega_0 T} - 1}\int_0^T dt'\left(\frac{t' - T/2}{t_0}\right)e^{-i\Omega_0 t'}\right.$$

$$\left. + e^{-il\Omega_0 T}\int_0^{\Delta t} dt'\left(\frac{t' - T/2}{t_0}\right)e^{-i\Omega_0 t'} + \xi_0\right\}, \quad t = lT + \Delta t, \qquad (6)$$

$$\Delta R = \Omega_0^{-1}\mathrm{Im}\xi = \frac{2R_0}{(2 + 3\gamma)}$$

$$\times\left\{\left(\frac{\Delta t - T/2}{t_0}\right) + \left[\frac{T}{2t_0}\cos(\Omega_0 \Delta t) - \frac{\sin(\Omega_0 \Delta t)}{2(t_0\Omega_0)}\right]\right.$$

$$+ \frac{[(\Omega_0 T)\cos(\Omega_0 T/2) - 2\sin(\Omega_0 T/2)]}{(t_0\Omega_0)}$$

$$\times\left[\cos(\Omega_0 \Delta t)\left(\frac{\sin(l\Omega_0 T)}{2\sin(\Omega_0 T/2)}\right)\right.$$

$$\left.\left. - \sin(\Omega_0 \Delta t)\left(\frac{1 - \cos(l\Omega_0 T)}{2\sin(\Omega_0 T/2)}\right)\right]\right\}.$$

Here, $\Omega_0 = (3\gamma P_0 \rho_0^{-1} R_0^2)^{1/2}$ is the natural frequency of linear pulsation of the bubble. In the case of a resonance between the *n*th harmonic of the external periodic field and the natural frequency, $\Omega_0 T = 2\pi n$, the coefficients in the third term (describing the contribution from *l* complete periods) linearly increase with time (i.e., with the number of periods *l*). This growth is naturally limited if we take into account the damping. For $\Omega_0 T \ll 1$, the bubble does not substantially change its size during the period (in the first order in $\Omega_0 T \ll 1$). For $\Omega_0 T \gg 1$, the maximum size $R_{\max} \sim R_0 + 2R_0(2 + 3\gamma)^{-1}(T/t_0)$ (differing little from the equilibrium radius) is attained by the moment of completion of the phase of extension under exposure to the external field.

When the field period increases, the wave amplitude also grows according to relation (5). In the case of $T/t_0 > 1$, we have to analyze a substantially nonlinear pulsation regime. If the drive varies slowly in comparison to the period of natural oscillations $2\pi/\Omega_0 < t_0$, we can obtain an analytical solution using the condition of existence of the adiabatic invariant. It was shown [1] that variation in the bubble radius in the asymptotic limit $t \gg t_0$ can be considered as a superposition of two motions:

$$R(t) = R_0\left(\frac{P_0}{P_m}\right)^{1/4}\left(\frac{t + t_0}{t_0}\right)^{1/3} + 0.01R_0\left(\frac{P_m}{P_0}\right)(t_0\Omega_0)^{1/3}$$

$$\times \sin\left\{\left(\frac{P_m}{P_0}\right)^{3/4}(t_0\Omega_0)\ln[\Omega_0(t + t_0)] + \alpha\right\}. \qquad (7)$$

Here, the first motion (the first term) represents the invariant (automodel) solution of Eq. (1) describing the power growth with an exponent different from that in the Rayleigh law. The second motion has the form of oscillations with a constant amplitude and a logarithmically increasing period. Expression (7) corresponds to $\gamma = 4.3$ for a bubble occurring at rest at the moment of the shock wave front propagation. In all the subsequent periods of external action, the structure of solution (7) is retained; only the amplitude and phase of the second term exhibit variation. At a sufficiently large time *t* (for $T \gg t_0$), such that transient processes are accomplished during the period, the first term in (7) predominates and the maximum bubble size is attained before arrival of

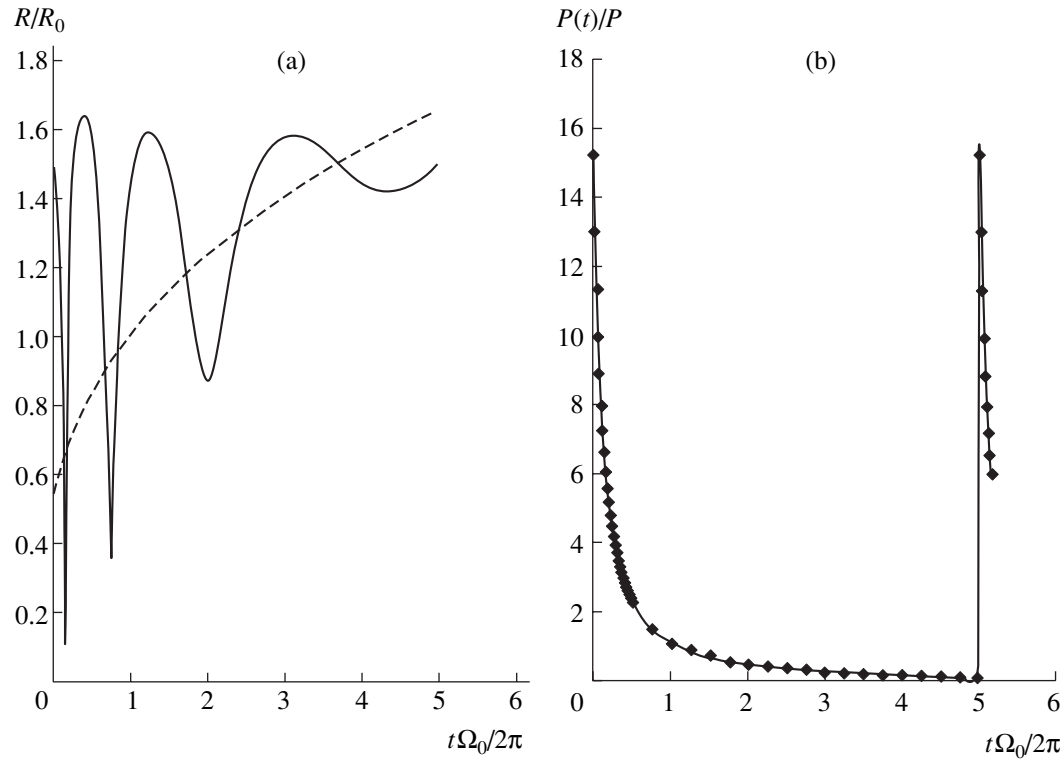

Fig. 2. Time variation of (a) the bubble size in a stationary regime and (b) the external pressure inducing these oscillations.

the next shock wave front. For an arbitrary γ, the maximum radius is

$$R_{\max} = R(T) = R_0(P_0/P_m)^{1/3\gamma}(T/t_0)^{2/2+3\gamma}. \quad (8)$$

Using relation (4) between the field amplitude P_m and the period T, we obtain $R_{\max} \sim R_0(P_m/P_0)^{(3\gamma-2)/[3\gamma(3\gamma+2)]}$. An extremely small exponent (for $\gamma = 4.3$, $R_{\max} \sim R_0(P_m/P_0)^{1/12}$) and the natural restrictions imposed on the ratio P_m/P_0 by the condition of applicability of the Rayleigh equation result in that the maximum radius cannot significantly exceed the equilibrium value ($R_{\max} \sim R_0$).

The case when the time t_0 is comparable with or shorter than the period of natural oscillations ($t_0 < 2\pi/\Omega_0$) and the external action is rather intense ($P_m/P_0 \geq 1$) does not admit analytical description. This case will be illustrated by the results of numerical calculations. Let us take the following values of the main parameters: $\gamma = 4.3$ and $T = 10\pi t_0$. Substituting these values into relation (4), we obtain an expression for the pressure amplitude:

$$(P_m/P_0) = (10\pi/3)[1-(1+10\pi)^{-1/3}]^{-1} \approx 15.26. \quad (9)$$

The results of numerical calculations of the time variation of the bubble radius in a stationary regime with $t_0\Omega_0 = 1$ are presented in Fig. 2a, where the dashed line shows the corresponding scale-invariant solution. Figure 2b shows the time variation of external pressure (2) for the amplitude determined by formula (9). Although analytical solution (7) in this case is formally inapplicable ($t_0 < 2\pi/\Omega_0$), it still qualitatively correctly reflects the behavior of the curve in Fig. 2a.

The most important feature of this numerical calculation is that (similar to all the cases considered above) the periodically prolonged scale-invariant drive is relatively inefficient in extending the bubble, even at a pressure on a megapascal level. This circumstance, on the one hand, makes the action considered here not very promising from the standpoint of investigation of the stable sonoluminescence of a single bubble—the acoustic cavitation effect most extensively studied in recent decades [7]. On the other hand, it is the relatively low efficiency of extension that makes the use of this pulse shape attractive from the standpoint of lithotripsy (noninvasive crushing of calculi in the kidney under the action of shock waves). The signal employed in medical practice comprises a train of about 1000 shock waves with a pressure jump of up to 60 MPa at the leading edge and a fall time of several microseconds [8]. A relatively small extending pressure (as compared to the pressure jump at the leading edge) in the scale-invariant drive does not significantly increases the bubble size, thus appreciably reducing the probability of tissue damage as a result of cavitation caused by the extension phase of the shock pulse.

Acknowledgments. This study was supported by the Russian Foundation for Basic Research, project no. 04-02-16412.

REFERENCES

1. A. O. Maksimov, Akust. Zh. **48**, 805 (2002) [Acoust. Phys. **48**, 713 (2002)].
2. A. O. Maksimov, Commun. Nonlinear Sci. Numer. Simul. **9**, 83 (2004).
3. L. D. Landau and E. M. Lifshitz, *Course of Theoretical Physics*, Vol. 6: *Fluid Mechanics* (Nauka, Moscow, 1986; Pergamon, New York, 1987).
4. C. C. Church, J. Acoust. Soc. Am. **86**, 215 (1989).
5. A. A. Chulichkov, V. A. Khokhlova, and M. R. Beĭli, in *Proceedings of the 11th Session of the Russian Acoustical Society, Moscow, 2001* (GEOS, Moscow, 2001), Vol. 1, pp. 56–59.
6. L. D. Landau and E. M. Lifshitz, *Course of Theoretical Physics*, Vol. 1: *Mechanics* (Nauka, Moscow, 1982; Pergamon, New York, 1988).
7. M. Brener, S. Hilgenfeldt, and D. Lohse, Rev. Mod. Phys. **74**, 425 (2002).
8. S. Barnet *et al.*, Ultrasound Med. Biol. **24**, 11 (1998).

Translated by P. Pozdeev

Technical Physics Letters, Vol. 31, No. 4, 2005, pp. 274–276. Translated from Pis'ma v Zhurnal Tekhnicheskoĭ Fiziki, Vol. 31, No. 7, 2005, pp. 14–18.

Acoustic Quality of Hydrogenated Low Carbon Steels

I. N. Burnyshev, O. M. Valiakhmetova, and V. F. Lys

Institute of Applied Mechanics, Urals Division, Russian Academy of Sciences, Izhevsk, Udmurtia, Russia

e-mail: lfp@fti.udm.ru

Received July 15, 2004; in final form, November 19, 2004

Abstract—The effect of electrolytic saturation with hydrogen on the acoustic quality factor (Q) of low carbon steels has been studied. As the hydrogenation time is increased, the Q value decreases at a rate that depends on the structural state of the steel. The change in Q is reversible: the removal of hydrogen from the material restores the Q value on a level close to that in the initial state (characteristic of a nonhydrogenated metal). © *2005 Pleiades Publishing, Inc.*

Investigation of the acoustic emission (AE) from tube steels tested for bending showed that the AE intensity exhibits a severalfold decrease upon hydrogenation of the material [1]. The possible reasons for this behavior are (i) a decrease in power of the AE sources under the action of hydrogen and (ii) the AE signal decay caused by a decrease in the acoustic quality of a hydrogenated steel.

This Letter reports on a change in the acoustic quality of a hydrogenated low-carbon steel (steel 20) depending on its structural state and on the cathode current in the course of electrolytic saturation with hydrogen. The experiments were performed in a specially designed setup described elsewhere [2]. The acoustic quality Q was measured using a method based on the sample resonance in the ultrasonic frequency range. The sample oscillations were excited by an electromagnetic-acoustic technique.

The effect of hydrogen on internal friction in metals has been extensively studied. However, the published experimental data mostly represent the results of low-frequency tests and refer to single-phase metals and alloys (predominantly ferrite—in particular, doped) at temperatures below room temperature [3]. In the present investigation, the tests were performed at room temperature on steel 20 samples having the form of cylinders with a length of 100 mm, a diameter of 5.6 mm, and a resonance frequency of 26 kHz. We studied the samples of steel 20 in various states, including the initial (as-received rolled rod material), as-quenched, and quenched with subsequent annealing at various temperatures. In order to study the influence of the amount of absorbed hydrogen on the acoustic quality of samples, the process of electrolytic hydrogenation was carried out at various cathode current densities. The treatment was performed in 0.1-N aqueous sulfuric acid solution containing 1.5 g/l of thiourea (an additive stimulating the hydrogenation process).

Previously, we studied [4] the effect of hydrogen on of the acoustic quality Q of steel 20 hydrogenated at a cathode current density of $j = 5$ mA/cm^2. Below, we describe the behavior of Q in the course of hydrogenation and dehydrogenation. The dependence of Q on the structural state of samples saturated with hydrogen at various cathode current densities were identical to those observed in [4] for $j = 5$ mA/cm^2. The maximum damping of ultrasonic oscillations was observed (irrespective of the cathode current) in the samples upon quenching followed by low-temperature (200°C) annealing. In contrast, virtually no changes in the

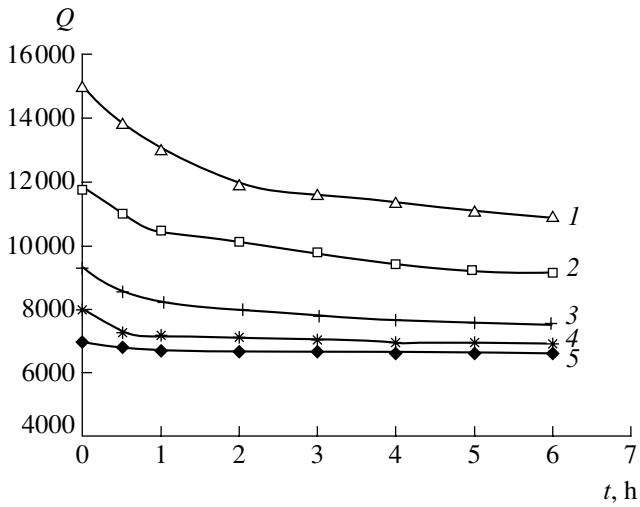

Fig. 1. Hydrogenation kinetics monitored by ΔQ measurements in steel 20 samples in various states: (*1*) quenched and annealed at 200°C; (*2*) as-quenched; (*3*) quenched and annealed at 300°C; (*4*) quenched and annealed at 400°C; (*5*) as-received.

1063-7850/05/3104-0274$26.00 © 2005 Pleiades Publishing, Inc.

acoustic quality were observed in the initial samples hydrogenated under the same conditions. As the annealing temperature is increased, the Q value of the nonhydrogenated samples decreases. This tendency is retained upon hydrogenation, and the effect of hydrogen on the damping of oscillations decreases with increasing annealing temperature (Fig. 1).

Figure 2 shows the dependence of a change in the acoustic quality $\Delta Q = Q_0 - Q_H$ on the cathode current density. Here, Q_0 and Q_H are the acoustic quality of a nonhydrogenated sample and that of the sample saturated with hydrogen for 6 h at a given current density, respectively. As can be seen, the curve in Fig. 2 exhibits a maximum at j = 5–10 mA/cm^2, while an increase in the cathode current density above this level leads to a decrease in ΔQ. In the literature, it is frequently accepted that the amount of hydrogen absorbed in the course of electrolytic hydrogenation is proportional to $\sqrt{j}$. If we assume that the degree of damping of the acoustic oscillations is proportional to the amount of absorbed hydrogen, the obtained results imply that the hypothesis concerning proportionality of the amount of absorbed hydrogen to the $\sqrt{j}$ value is valid only in the region of small currents. The observed behavior of ΔQ in the samples hydrogenated at large current densities can be explained in two ways. According to the first variant, an increase in the current density above 10 mA/cm^2 does not lead to a further increase in the amount of absorbed hydrogen. The second variant assumes that there is a certain critical hydrogen content in the steel, above which the excess hydrogen does not additionally influence the damping. The excess hydrogen (occurring in pores and crevices) does not influence the motion of dislocations, which is one of the mechanisms responsible for a decrease in the acoustic quality of the system.

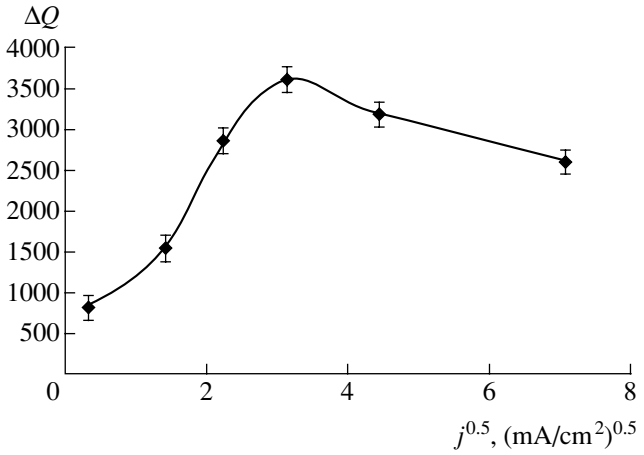

Fig. 2. A plot of the acoustic quality increment ΔQ versus current density $j^{0.5}$ for hydrogenated steel 20.

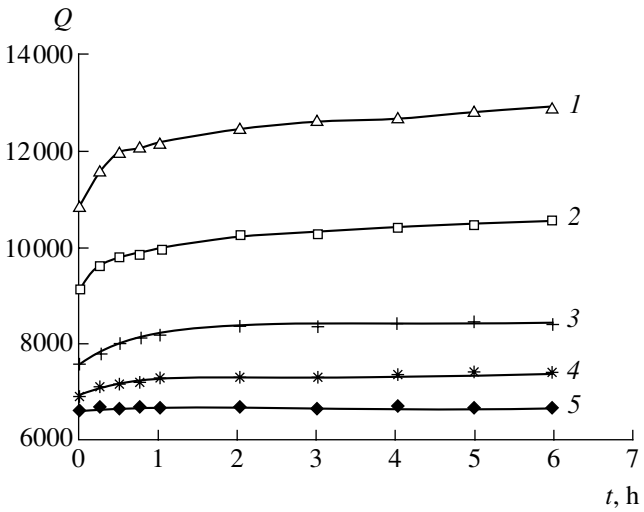

Fig. 3. Dehydrogenation kinetics in steel 20 samples kept in air at room temperature (sample notation is the same as in Fig. 1).

In the course of hydrogen removal (dehydrogenation), which was achieved by keeping a hydrogenated sample at room temperature, the Q value showed a tendency to be restored on the initial level (Fig. 3). The most rapid increase in Q takes place in the first hours of dehydrogenation. The rate of hydrogen evolution (as well as the rate of hydrogen absorption) in the initial stage depends on the structural state of a sample. The most pronounced increase in Q was observed for the samples upon quenching and annealing at 200°C, that is, in the same state where the maximum decrease in Q was observed upon hydrogenation. The rate of acoustic quality restoration gradually decreases. The initial Q value was not completely restored even after keeping the samples at room temperature for 20 h. The maximum difference between the initial Q value and that upon dehydrogenation was observed for a sample characterized by maximum damping, that is, for the sample upon quenching and annealing at 200°C. An increase in the dehydrogenation time leads to a decrease in this difference, but complete restoration was not observed even after 140 h. This can be explained by the presence of residual hydrogen, which can be retained in hydrogen traps (where it occurs in equilibrium with the alloy components); the complete removal of hydrogen from the metal may require a much longer time.

The data on the damping of acoustic oscillations in low-carbon steels can be explained using two mechanisms, namely, scattering on dislocations (which act as hydrogen traps) and scattering due to friction forces arising when hydrogen atoms move in the ultrasonic field. It is difficult to separate the contributions of these mechanisms to the total damping effect.

Acknowledgments. This study was supported by the Russian Foundation for Basic Research, project nos. 01-01-96436 and 04-01-96020.

REFERENCES

1. I. N. Burnyshev and E. A. Pechina, Vestn. Tambovsk. Univ. **5**, 351 (2000).
2. E. S. Makhnev, I. N. Burnyshev, N. A. Glukhov, *et al.*, *Investigation of the Damping Properties of Metals by the Electromagnetic-Acoustic Method* (Institute of Applied Mechanics, Izhevsk, 1999) [in Russian].
3. P. V. Gel'd, R. A. Ryabov, and E. S. Kodes, *Hydrogen and Metal Structure Imperfections* (Metallurgiya, Moscow, 1979) [in Russian].
4. I. N. Burnyshev, O. M. Valiakhmetova, N. A. Glukhov, *et al.*, in *Proceedings of the 16th Ural School for Physical Metallurgy and Thermal Treatment of Metals, Ufa, 2002*, p. 182.

Translated by P. Pozdeev

Technical Physics Letters, Vol. 31, No. 4, 2005, pp. 277–279. Translated from Pis'ma v Zhurnal Tekhnicheskoĭ Fiziki, Vol. 31, No. 7, 2005, pp. 19–24.

X-ray Optic Characteristics of Microchannel Plates Studied by X-ray Absorption Spectroscopy

M. I. Mazuritskii*, A. V. Soldatov, and M. Kasrai

Rostov State University, Rostov-on-Don, Russia

** e-mail: mazurmik@aaanet.ru*

Received June 2, 2004; in final form, October 12, 2004

Abstract—The X-ray absorption spectra of white and black microchannel plates (MCPs) have been studied in the energy range from 80 to 250 eV. Data on the fine X-ray absorption near edge structure are presented. A new approach is described, which allows the effect of various treatments on the X-ray optic characteristics of MCPs to be studied. In particular, it is established that the thermal reduction of MCPs in hydrogen increases the critical reflection angle for long-wavelength X-rays in the channels. © *2005 Pleiades Publishing, Inc.*

Microchannel plates (MCPs) are widely used in X-ray reflection, focusing, and filtration devices [1–3]. In this respect, the channel surface reflection characteristics are extremely important, in particular in the case of low-energy radiation. In this Letter, we present the results of experimental investigations of the X-ray absorption spectra of MCPs and describe for the first time a new approach that allows the X-ray absorption data to be used for monitoring a change in the critical reflection angle of MCPs upon various technological treatments.

The X-ray absorption spectra of "white guide" (WG) and "black guide" (BG) MCPs were measured at a 0.1-eV energy resolution on a Mark IV Grasshopper spectrometer operating at the Canadian Synchrotron Center of the University of Wisconsin (Madison, USA). The results were reproduced in three independent series of measurements, whereby the spectra were measured on different samples of white and black MCPs.

According to the classical scheme of X-ray absorption measurements, a sample is exposed to a primary X-ray beam of known intensity in a given energy range, and the spectral distribution of the intensity of radiation transmitted through the sample is measured. Thus, the absorption spectrum represents the energy (or wavelength) dependence of the ratio of intensities of the transmitted and primary (incident) radiation fluxes. Since samples of the required thickness are not always available, some other techniques have been developed that allow spectral dependences analogous to the classical transmission absorption spectra to be obtained. In particular, the fluorescence yield (FY) and total electron yield (TEY) spectra are obtained by exciting a sample with a monochromatic radiation scanned over energies in the vicinity of the corresponding absorption edges (e.g., B *K* or Si *L*). In the case of FY spectroscopy, the response signal is the integral (total) intensity of X-ray fluorescence. In the case of TEY spectroscopy, the response (upon monochromatic excitation) is the total yield of photoelectrons (including the Auger electrons) escaping from the samples surface under the action of an applied Coulomb field. Obviously, the TEY measurements are more sensitive with respect to the composition and structure of a thin (within 500-Å-thick) near-surface layer of the sample, whereas the FY spectra provide information about the electron structure from deeper layers.

Figures 1 and 2 present the review X-ray absorption spectra of the WG and BG samples, respectively. The WG type sample is a matrix plate with holes, which serve as blanks for the electron multiplier channels. The matrix framework is composed of a lead silicate glass, while the holes are initially (prior to chemical etching) filled with a borosilicate glass. Note that the presence of a signal due to the boron absorption *K*-edge (194.4 eV)

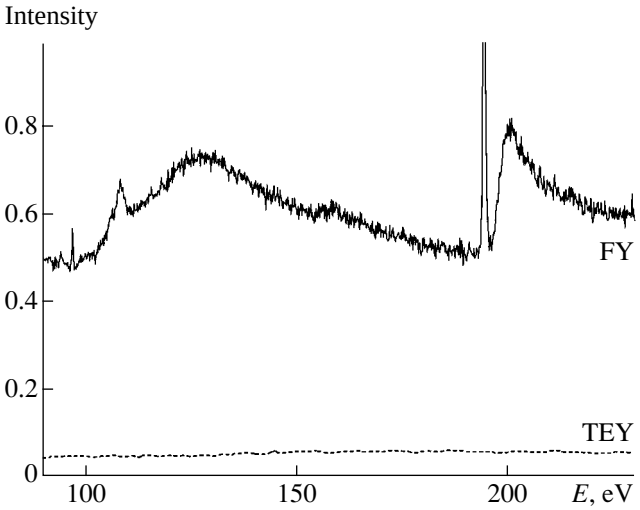

Fig. 1. Review X-ray absorption spectrum of a "white" (WG) microchannel plate.

1063-7850/05/3104-0277$26.00 © 2005 Pleiades Publishing, Inc.

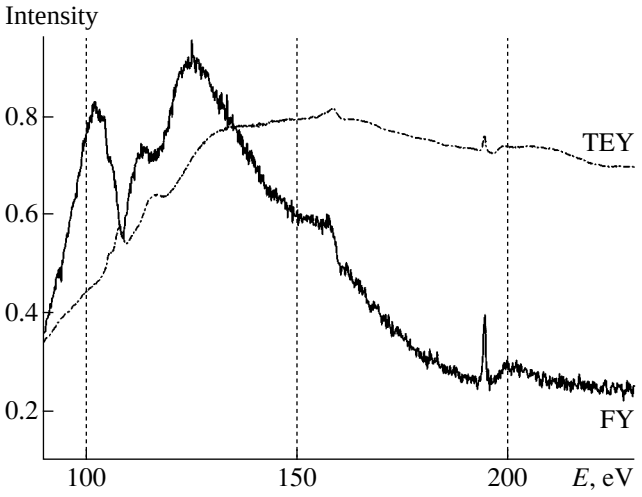

Fig. 2. Review X-ray absorption spectrum of a "black" (BG) microchannel plate.

is evidence that borosilicate glass traces are present on the lead silicate glass surface. The BG type samples were prepared from the WG ones by means of thermal reduction in hydrogen. This procedure modifies the physicochemical properties of the initial glass. An analysis of the sample surface structure indicated [4–6] a change in the state of silicon oxide SiO_x, where $1 < x < 2$. In addition, the dielectric permittivity of the BG type samples was significantly lower than that before the thermal treatment in hydrogen. Experimental data on the main components of the X-ray absorption near edge structure of the MCPs studied are presented in the table.

A comparison of the FY structures in the spectra presented in Figs. 1 and 2 shows that the curve for the BG sample in the interval of energies up to about 120 eV (see Fig. 2) appears as the inverse of the analogous curve for the WG sample. In other words, the structure of the FY spectrum of the BG plate in the soft X-ray range resembles that of the classical absorption spectra obtained in the transmission mode. At the same time, no such difference is observed in the TEY spectra. Let us consider in more detail the mechanism of formation of the fine structure of Si $L_{II,III}$ absorption spectra in the samples studied.

Experimental conditions for both FY and TEY measurements were as follows. A monochromatic X-ray beam was incident at the same angle (nearly perpendicular) relative to the sample surface. As is known, the maximum intensity of fluorescence is observed at a right angle to the incident exciting radiation flux. Both WG and BG samples contain through holes (channels) accounting for up to 80% of the total surface area. Evidently, the rays entering these channels fall on their inner walls at small (sliding) angles. In comparison to the case of a flat sample, the measured response intensity is attenuated as a result of the fluorescence signal absorption inside the sample. The TEY spectrum of the BG sample is characterized by a significantly higher intensity as compared to that of the WG plate and displays clear absorption edges of silicon, lead, and boron. Apparently, the photoelectrons are capable of escaping (under the action of the applied electric field) even from inside the channels.

Experimental values of the main X-ray absorption near edge structure components of MCPs

Electron levels	Pb O_{III} ($5p_{3/2}$)	Si L_{III} ($2p_{3/2}$)	Pb O_{II} ($5p_{1/2}$)	Pb N_{VII} ($4f_{7/2}$)	Si L_I ($2s_{1/2}$)	B K ($1s_{1/2}$)
Energy, eV	97.1	108.5 (WG) 109.1 (BG)	115	144.7	157.2	194.4

The condition of sliding incidence is satisfied when the angle θ between the incident beam and the surface (glancing angle) is smaller than a certain critical value θ_c characteristic of a given substance, corresponding to total external reflection. It should be recalled that the optical properties of substances in the X-ray range are conveniently described in terms of the complex permittivity $\varepsilon = 1 - \delta + i\gamma$, where $\delta, \gamma \ll 1$. This quantity also determines the value of the critical angle to be $\theta_c = \sqrt{\delta}$, which increases with the radiation wavelength. In the wavelength range studied, the critical angle falls within 7°–10° [7].

Evidently, the white and black plates do not differ in their compositions. With neglect of the scattering, the incident radiation is either reflected or penetrates the substance and then is absorbed by atomic electron shells. In the case of BG, the absence of fluorescence near the Si L absorption edge is indicative of a sharp decrease in the penetration depth for the X-rays incident on the channel walls. This behavior corresponds to total external reflection, whereby the radiation propagates along the channel virtually without attenuation. This regime was considered in detail in [6, 9].

The value of the reflection coefficient is determined by the quantity $\exp(-\gamma/\delta^{3/2})$ and may exhibit significant growth. Note that the most substantial distinction between white and black MCPs is the difference in their dielectric properties: the conductivity of BG samples is higher by several orders of magnitude than that of the WG plates. In other words, the radiation escapes from black MCPs upon multiple reflections in a channel and exhibits absorption near the Si L edge. This is confirmed by the fact that the Si L absorption edge in the FY spectrum of the BG sample has the inverse shape and is shifted by 0.6 V toward higher energies as compared to the spectrum of the WG sample. In addition, the main resonance maximum in the spectrum of the BG plate is somewhat wider than that for the WG plate. This is explained by the fact that the glass surface upon thermal treatment contains silicon oxidized to various states SiO_x, where $1 < x < 2$. The spectrum observed

upon multiple reflections and partial absorption exhibits a superposition of several Si *L* absorption spectra of such oxide components.

In a short-wavelength range, the coefficient of X-ray reflection may significantly decrease for two reasons: first, as a result of a decrease in the critical total external reflection angle; second, due to a sharp drop in reflection caused by a jump in the absorption coefficient. This explains the absence of the inverse structure in the spectra of black MCPs, for example, in the region of the B *K* absorption edge (194 eV).

In order to completely elucidate the nature of the inverse absorption spectra of black MCPs, it is necessary to perform experiments for various radiation incidence angles. Then, using X-ray absorption measurements in a broad spectral range, it is possible to analyze the influence of technological factors on the critical reflection angle of MCPs.

In conclusion, it should be noted that the thermal reduction in hydrogen increases the limiting angle of total external reflection, thus increasing the efficiency of X-ray waveguides made of a silica glass. This kind of modification is especially attractive for the fabrication of MCPs to be used as X-ray filters and reflectors operating in a long-wavelength range.

REFERENCES

1. N. Yamaguchi, S. Aoki, and S. Miyoshi, Rev. Sci. Instrum. **58**, 43 (1987).
2. H. N. Chapman, A. Rode, K. A. Nugent, and S. W. Wilkins, Appl. Opt. **32**, 6333 (1993).
3. A. P. Martin, A. N. Brunton, G. W. Fraser, and A. F. Abbey, Nucl. Instrum. Methods Phys. Res. A **460**, 316 (2001).
4. A. T. Kozakov, A. V. Nikol'skii, M. I. Mazuritskii, *et al.*, Pis'ma Zh. Tekh. Fiz. **17** (12), 9 (1991) [Sov. Tech. Phys. Lett. **17**, 426 (1991)].
5. A. T. Kozakov, A. V. Nikol'skii, and M. I. Mazuritskii, Fiz. Khim. Stekla, No. 6, 225 (1991).
6. A. V. Soldatov, T. S. Ivanchenko, and M. I. Mazuritskii, Fiz. Tverd. Tela (St. Petersburg) **36**, 836 (1994) [Phys. Solid State **36**, 459 (1994)].
7. A. V. Vinogradov and I. V. Kozhevnikov, Tr. Fiz. Inst. Akad. Nauk SSSR **196**, 18 (1989).
8. I. V. Kozhevnikov, Tr. Fiz. Inst. Akad. Nauk SSSR **196**, 143 (1989).
9. S. B. Dabagov, A. Marcelli, V. A. Murashoval, *et al.*, Report No. LNF-99/033 (P) (Laboratori Nazionali di Frascati, 1999).
10. V. A. Arkad'ev and M. A. Kumakhov, Poverkhnost **10**, 25 (1986).

Translated by P. Pozdeev

Technical Physics Letters, Vol. 31, No. 4, 2005, pp. 280–283. Translated from Pis'ma v Zhurnal Tekhnicheskoĭ Fiziki, Vol. 31, No. 7, 2005, pp. 25–31.

Plane Defect-Field Wave Propagation in a Viscoelastic Medium

N. V. Chertova and M. A. Chertov

Institute of Strength Physics and Materials Science, Siberian Division, Russian Academy of Sciences, Tomsk, 634055 Russia

Received October 18, 2004

Abstract—The wave solutions of the system of equations describing the defect field in a viscoelastic medium are studied within the framework of the defect field theory. The refraction and absorption coefficients and the velocities of propagation of the elastic continuum and the defect continuum waves are determined. Features of the correlation between various waves are analyzed. © *2005 Pleiades Publishing, Inc.*

Previously, the laws of propagation of plane defect waves were studied [1–3] using a system of equations of the defect field theory,

$$B\frac{\partial}{\partial x_i}I_{ij} = -P_j, \quad e_{ikl}\frac{\partial}{\partial x_k}I_{lj} = \frac{\partial}{\partial t}\alpha_{ij},$$
$$\frac{\partial}{\partial x_k}\alpha_{ki} = 0, \quad Se_{ikl}\frac{\partial}{\partial x_k}\alpha_{lj} = -B\frac{\partial}{\partial t}I_{ij} - \sigma_{ij}, \tag{1}$$

in a homogeneous viscoplastic medium described by the relations

$$\sigma_{ij} = \theta_{ijkl}I_{kl} \tag{2}$$

and the corresponding boundary conditions. In Eqs. (1) and (2), α_{ij} is the dislocation density tensor, I_{ij} is the dislocation flux density tensor, σ_{ij} is the effective stress tensor, P_j is the effective momentum, θ_{ijkl} is the tensor of viscosity coefficients, and B and S are constant quantities.

In this paper, an analogous investigation is performed for the case of a viscoelastic medium [4] described by the relations

$$\sigma_{ij} = \sigma_{ij}^{\mathrm{el}} + \sigma_{ij}^{\mathrm{v}}, \tag{3}$$

where $\sigma_{ij}^{\mathrm{el}}$ and σ_{ij}^{v} are the elastic and viscous stresses, respectively, which can be expressed using well-known relations via components of the displacement vector U_i, the tensor of elastic moduli C_{ijkl}, and the tensor of viscosity coefficients η_{ijkl} [5]:

$$\sigma_{ij}^{\mathrm{el}} = C_{ijkl}\partial_k U_l, \quad \sigma_{ij}^{\mathrm{v}} - \eta_{ijkl}\partial_k V_l. \tag{4}$$

The momentum vector of the medium can be expressed as

$$P_i = \rho V_i = \rho\frac{\partial}{\partial t}U_i, \tag{5}$$

where ρ is the density. Equations (1) also obey the compatibility condition

$$\frac{\partial}{\partial t}P_i = \frac{\partial}{\partial x_k}\sigma_{ki}, \tag{6}$$

which is essentially the equation of dynamic equilibrium.

Let us consider solutions to Eqs. (1), (3)–(5) in the wave form,

$$\{\alpha_{ij}(r,t), I_{ij}(r,t), U_i(r,t)\} = (\alpha_{ij}(x), I_{ij}(x), U_i(x))\exp(-i\omega t), \tag{7}$$

assuming that the unknown quantities depend on a single coordinate x. For the complex components of $\alpha_{ij}(x)$, $I_{ij}(x)$, and $U_i(x)$, the system of equations (1), (3)–(5) can be rewritten as

$$B\partial_x I_{xj}(x) = i\omega\rho U_j(x), \tag{8.1}$$

$$i\omega\alpha_{xj}(x) = 0, \quad i\omega\alpha_{yi}(x) = \partial_x I_{zj}(x), \quad i\omega\alpha_{zj}(x) = -\partial_x I_{yj}(x), \tag{8.2}$$

$$\partial_x\alpha_{xj}(x) = 0, \tag{8.3}$$

$$i\omega BI_{xj}(x) - \sigma_{xj}(x) = 0,$$
$$i\omega BI_{yj}(x) - \sigma_{yj}(x) = -S\partial_x\alpha_{zj}(x), \tag{8.4}$$
$$i\omega BI_{zj}(x) - \sigma(x) = S\partial_x\alpha_{yj}(x).$$

For a homogeneous isotropic body, the tensors of elastic moduli and viscosity coefficients have the following form [5]:

$$C_{ijkl} = \lambda\delta_{ij}\delta_{kl} + \mu(\delta_{ik}\delta_{jl} + \delta_{il} + \delta_{jk}), \tag{9}$$

$$\eta_{ijkl} = \xi\delta_{ij}\delta_{kl} + \gamma(\delta_{ik}\delta_{jl} + \delta_{il} + \delta_{jk}), \tag{10}$$

where λ and μ are the Lamé coefficients; ξ and γ are the

volume and shear viscosity, respectively; and δ_{ij} is the Kronecker delta. In this case, the stress tensor components according to relations (4) and (5) can be written as

$$\begin{matrix}(\lambda+2\mu)\partial_x U_x(x)+(\xi+2\gamma)\partial_x\partial_t U_x(x), & \mu\partial_x U_y(x)+\gamma\partial_x\partial_t U_y(x), & \mu\partial_x U_z(x)+\gamma\partial_x\partial_t U_z(x),\\ \mu\partial_x U_y(x)+\gamma\partial_x\partial_t U_y(x), & \lambda\partial_x U_x(x)+\xi\partial_x\partial_t U_x(x), & 0,\\ \mu\partial_x U_z(x)+\gamma\partial_x\partial_t U_z(x), & 0, & \lambda\partial_x U_x(x)+\xi\partial_x\partial_t U_x(x).\end{matrix} \quad (11)$$

Using the first relation in (8.4), expressions for the stress tensor components (11), and relation (8.1) (or Eqs. (3)–(6) and (11)), we obtain the following equations for determining the displacement vector components $U_i(x)$:

$$\partial_x^2 U_x(x)+(\omega/C_1)^2/\left(1-\frac{i\omega(\xi+2\gamma)}{\lambda+2\mu}\right)U_x(x)=0,$$

$$\partial_x^2 U_y(x)+(\omega/C_2)^2/(1-i\omega\gamma/\mu)U_y(x)=0, \quad (12)$$

$$\partial_x^2 U_z(x)+(\omega/C_2)^2/(1+i\omega\gamma/\mu)U_z(x)=0,$$

where $C_1=\sqrt{(\lambda+2\mu)/\rho}$ and $C_2=\sqrt{\mu/\rho}$ are the longitudinal and transverse elastic wave velocities, respectively. The solutions to Eqs. (12) are well known and can be written as

$$\begin{aligned}U_x(x)&=a_1\exp(ik_1x)+a_2\exp(-ik_1x),\\ U_y(x)&=b_1\exp(ik_2x)+b_2\exp(-ik_2x),\\ U_z(x)&=c_1\exp(ik_2x)+c_2\exp(-ik_2x),\end{aligned} \quad (13)$$

where

$$\begin{aligned}k_1^2&=(\omega/C_1)^2/\left(1-\frac{i\omega(\xi+2\gamma)}{\lambda+2\mu}\right),\\ k_2^2&=(\omega/C_2)^2/(1-i\omega\gamma/\mu);\end{aligned} \quad (14)$$

a_1, a_2, b_1, b_2, c_1, and c_2 are unknown constants determined from the boundary conditions. Using the refraction and absorption coefficients (n_1, χ_1) and (n_2, χ_2) [6], expressions (14) can be rewritten as

$$k_1=\omega(n_1+i\chi_1)/C_1, \quad k_2=\omega(n_2+i\chi_2)/C_2. \quad (15)$$

The above refraction and absorption coefficients can be also expressed via the so-called loss tangents $\tan\delta_1=\omega(\xi+2\gamma)/(\lambda+2\mu)$ and $\tan\delta_2=\omega\gamma/\mu$ as

$$\begin{aligned}n_1&=[((\tan^2\delta_1+1)^{1/2}+1)/2(\tan^2\delta_1+1)]^{1/2},\\ \chi_1&=[((\tan^2\delta_1+1)^{1/2}-1)/2(\tan^2\delta_1+1)]^{1/2},\end{aligned} \quad (16)$$

and the analogous relations for (n_2, χ_2). The refractive indices (n_1, n_2) determine the phase velocity of the waves, while the absorption coefficients (χ_1, χ_2) characterize the rate of decay of the wave amplitude in the propagation direction [4, 6].

Once the $U_i(x)$ values are known, the dislocation flux density tensor components $I_{xj}(x)$ can be determined from the first relation in (8.4) as

$$\begin{aligned}I_{xx}(x)&=(C_1\rho/B\sqrt{n_1^2+\chi_1^2})\\ &\times[a_1\exp(ik_1a)-a_2\exp(-ik_1x)]\exp(-i\chi_1/n_1),\\ I_{xy}(x)&=(C_2\rho/B\sqrt{n_2^2+\chi_2^2})\\ &\times[b_1\exp(ik_2a)-b_2\exp(-ik_2x)]\exp(-i\chi_2/n_2),\\ I_{xz}(x)&=(C_2\rho/B\sqrt{n_2^2+\chi_2^2})\\ &\times[c_1\exp(ik_2x)-c_2\exp(-ik_2x)]\exp(-i\chi_2/n_2).\end{aligned} \quad (17)$$

Then, the unknown $I_{yj}(x)$ and $I_{zj}(x)$ can be determined by jointly using the last relations in (8.2) and (8.4):

$$\begin{aligned}-\omega^2BI_{yj}(x)-i\omega\sigma_{yj}(x)&=S\partial_x^2I_{yj}(x),\\ -\omega^2BI_{zj}(x)-i\omega\sigma_{zj}(x)&=S\partial_x^2I_{zj}(x).\end{aligned}$$

Taking into account relations (11), these expressions can be rewritten as

$$\begin{aligned}&\partial_x^2I_{yx}(x)+k_3^2I_{yx}(x)\\ &=-\frac{i\omega}{S}(\mu-i\omega\gamma)\partial_xU_y(x)=-\frac{i\omega^3\rho}{Sk_2^2}\partial_xU_y(x),\\ &\partial_x^2I_{yy}(x)+k_3^2I_{yy}(x)\\ &=-\frac{i\omega}{S}(\lambda-i\omega\xi)\partial_xU_x(x)=-\frac{i\omega^3\rho}{Sk_4^2}\partial_xU_x(x),\\ &\partial_x^2I_{yz}(x)+k_3^2I_{yz}(x)=0,\\ &\partial_x^2I_{zx}(x)+k_3^2I_{zx}(x)\end{aligned} \quad (18)$$

$$= -\frac{i\omega}{S}(\mu - i\omega\gamma)\partial_x U_z(x) = -\frac{i\omega^3\rho}{Sk_2^2}\partial_x U_z(x),$$

$$\partial_x^2 I_{zy}(x) + k_3^2 I_{zy}(x) = 0,$$

$$\partial_x^2 I_{zz}(x) + k_3^2 I_{zz}(x)$$

$$= -\frac{i\omega}{S}(\lambda - i\omega\xi)\partial_x U_x(x) = -\frac{i\omega^3\rho}{Sk_4^2}\partial_x U_x(x),$$

where

$$k_3^2 = (\omega/C_3)^2,\ C_3 = \sqrt{S/B},$$

$$k_4^2 = (\omega/C_4)^2/(1 - i\omega\xi/\lambda) = [\omega(n_4 + i\chi_4)/C_4]^2,$$

$$C_4 = \sqrt{\lambda/\rho},\ \tan\delta_4 = \omega\xi/\lambda.$$

The quantities n_4 and χ_4 are determined using the expressions analogous to formulas (16). The known solutions of two equations (18) analogous to Eqs. (12) are as follows:

$$\begin{aligned} I_{yz}(x) &= d_1\exp(ik_3x) + d_2\exp(-ik_3x),\\ I_{zy}(x) &= f_1\exp(ik_3x) + f_2\exp(-ik_3x), \end{aligned} \tag{19}$$

where d_1, d_2, f_1, and f_2 are unknown constant coefficients. The solutions to other equations (18) will contain two terms, one representing a solution to the corresponding homogeneous equation and the other depending on the function in the right-hand part of each equation:

$$\begin{aligned} I_{yx}(x) &= g_1\exp(ik_3x) + g_2\exp(-ik_3x)\\ &+ \frac{\omega^3\rho}{Sk_2(k_3^2 - k_2^2)}(b_1\exp(ik_2x) - b_2\exp(-ik_2x)),\\ I_{yy}(x) &= h_1\exp(ik_3x) + h_2\exp(-ik_3x)\\ &+ \frac{\omega^3\rho k_1}{Sk_4^2(k_3^2 - k_1^2)}(a_1\exp(ik_1x) - a_2\exp(-ik_1x)),\\ I_{zx}(x) &= q_1\exp(ik_3x) + q_2\exp(-ik_3x)\\ &+ \frac{\omega^3\rho}{Sk_2(k_3^2 - k_2^2)}(c_1\exp(ik_2x) - c_2\exp(-ik_2x)),\\ I_{zz}(x) &= p_1\exp(ik_3x) + p_2\exp(-ik_3x)\\ &+ \frac{\omega^3\rho k_1}{Sk_4^2(k_3^2 - k_1^2)}(a_1\exp(ik_1x) - a_2\exp(-ik_1x)), \end{aligned} \tag{20}$$

where g_1, g_2, h_1, h_2, q_1, q_2, etc., are constant coefficients.

The dislocation density tensor components $\alpha_{yj}(x)$, $\alpha_{zj}(x)$ can be determined from the last relations in (8.2) as

$$\begin{aligned} \alpha_{yx}(x) &= [q_1\exp(ik_3x) - q_2\exp(-ik_3x)]/C_3\\ &+ \frac{\omega^2\rho}{S(k_3^2 - k_2^2)}[c_1\exp(ik_2x) + c_2\exp(-ik_2x)],\\ \alpha_{yy}(x) &= [f_1\exp(ik_3x) - f_2\exp(-ik_3x)]/C_3,\\ \alpha_{yz}(x) &= [p_1\exp(ik_3x) - p_2\exp(-ik_3x)]/C_3\\ &+ \frac{\omega^2\rho k_1^2}{Sk_4^2(k_3^2 - k_1^2)}[a_1\exp(ik_1x) + a_2\exp(-ik_1x)],\\ \alpha_{zx}(x) &= [g_2\exp(-ik_3x) - g_1\exp(ik_3x)]/C_3\\ &- \frac{\omega^2\rho}{S(k_3^2 - k_2^2)}[b_1\exp(ik_2x) + b_2\exp(-ik_2x)],\\ \alpha_{zy}(x) &= [h_2\exp(-ik_3x) - h_1\exp(-ik_3x)]/C_3\\ &- \frac{\omega^2\rho k_1^2}{Sk_4^2(k_3^2 - k_1^2)}[a_1\exp(ik_1x) + a_2\exp(-ik_1x)],\\ \alpha_{zz}(x) &= [d_2\exp(-ik_3x) - d_1\exp(ik_3x)]/C_3. \end{aligned} \tag{21}$$

According to the first relations in (8.2) and (8.3), we have

$$\alpha_{xj}(x) = 0. \tag{22}$$

Thus, a viscoelastic medium with defects (dislocations) features plane waves of the elastic displacements, the defect density tensor, and the defect flux density tensor. The waves of elastic displacements and the "longitudinal" components of the defect flux density tensor $I_{xj}(x, t)$ are interrelated. Here, the term "longitudinal" tensor component implies that the first index coincides with the wave propagation direction. The waves of U_i and $I_{xj}(x, t)$ propagate at equal velocities determined by the coefficients of refraction and absorption and by the sound wave velocity (15). The amplitudes of these waves are related via the coefficients

$$\theta_1 = C_1\rho/(B\sqrt{n_1^2 + \chi_1^2}),\quad \theta_2 = C_2\rho/(B\sqrt{n_2^2 + \chi_2^2}),$$

and there is a phase difference determined by the ratios χ_1/n_1 and χ_2/n_2.

For $\tan\delta_1 \ll 1$ and $\tan\delta_2 \ll 1$, we deal with the case of weakly decaying waves of U_i and $I_{xj}(x, t)$, such that

$$n_1 = 1,\quad \chi_1 = (\tan\delta_1)/2 = \omega(\xi + 2\gamma)/2(\lambda + 2\mu),$$

$$n_2 = 1,\quad \chi_2 = (\tan\delta_2)/2 = \omega\gamma/2\mu.$$

In this case, dispersion is absent and dissipation is frequency dependent. For $\tan\delta_1 \gg 1$ and $\tan\delta_2 \gg 1$, the

waves exhibit strong damping and

$$n_1 \approx \chi_1 = 1/\sqrt{2(\tan\delta_1)} = 1/\sqrt{2\omega(\xi + 2\gamma)/(\lambda + 2\mu)},$$

$$n_2 \approx \chi_2 = 1/\sqrt{2(\tan\delta_2)} = 1/\sqrt{2\omega\gamma/\mu},$$

so that both dispersion and dissipation are frequency dependent. In the case of strong damping, the wave process is practically absent, since the waves decay over a very short distance as compared to the corresponding wavelength (λ_1, λ_2):

$$d_1 = C_1/\omega\chi_1 = \lambda_1/2\pi\chi_1, \quad d_2 = C_2/\omega\chi_2 = \lambda_2/2\pi\chi_2.$$

The "longitudinal" waves of the dislocation density tensor components $\alpha_{xj}(x, t)$ do not exist, in agreement with the conclusions derived previously [2]. The waves of the "transverse" components $I_{yi}(x, t)$, $I_{zi}(x, t)$, $\alpha_{zi}(x, t)$, and $\alpha_{yi}(x, t)$ (with the first index perpendicular to the wave propagation direction) represent superposition of the waves of the dislocation ensemble propagating at a velocity of $C_3 = \sqrt{S/B}$ and the waves related to the field of elastic displacements (13). An exception is presented by the components $I_{yz}(x, t)$, $I_{zy}(x, t)$, $\alpha_{yy}(x, t)$, and $\alpha_{zz}(x, t)$, whose dynamics is independent of the elastic displacements.

Acknowledgments. This study was supported by the Russian Foundation for Basic Research, project no. 02-01-01188.

REFERENCES

1. N. V. Chertova and Yu. V. Grinyaev, Pis'ma Zh. Tekh. Fiz. **25** (18), 91 (1999) [Tech. Phys. Lett. **25**, 756 (1999)].
2. N. V. Chertova, Pis'ma Zh. Tekh. Fiz. **29** (2), 83 (2003) [Tech. Phys. Lett. **29**, 78 (2003)].
3. N. V. Chertova and Yu. V. Grinyaev, Prikl. Mekh. Tekh. Fiz. **45**, 115 (2004).
4. L. D. Landau and E. M. Lifshitz, *Course of Theoretical Physics*, Vol. 7: *Theory of Elasticity* (Nauka, Moscow, 1987; Pergamon, New York, 1986).
5. L. I. Sedov, *Course in Continuum Mechanics* (Wolters-Noordhoff, Groningen, 1971; Nauka, Moscow, 1976), Vol. 1.
6. M. B. Vinogradova, O. V. Rudenko, and A. P. Sukhorukov, *The Theory of Waves* (Nauka, Moscow, 1990) [in Russian].

Translated by P. Pozdeev

Technical Physics Letters, Vol. 31, No. 4, 2005, pp. 284–287. Translated from Pis'ma v Zhurnal Tekhnicheskoĭ Fiziki, Vol. 31, No. 7, 2005, pp. 32–39.

Special Features of Heavy Metal Ion Reduction from Liquid Electrolytes

V. I. Trigub and S. V. Plokhov

Nizhni Novgorod State Technical University, Nizhni Novgorod, Russia

Received June 21, 2004; in final form, November 1, 2004

Abstract—The ion exchange reduction of heavy metal ions from electrolytes has been studied by theoretical and experimental methods. It is established that high efficiency of the ion exchange is provided by metal ion diffusion through a thin subsurface layer of an ion exchanger with a thickness of $\tilde{\delta} = 1.6 \times 10^{-4}$ m under conditions of the optimum solution flow velocity U_0, such that the time of ion penetration through the layer of water molecules adsorbed on the surface of pores in this layer is on the order of 10^{-2} s. In this case, the effective diffusion coefficient of metal ions in the subsurface layer is 4.5×10^{-7} m^2/s, which is more than two orders of magnitude higher than the value in solution. © *2005 Pleiades Publishing, Inc.*

Elucidation of the mechanism responsible for the reduction of heavy metal ions from electrolytes is one of the very important problems in modern science. This knowledge is of importance both for the purification of solutions from undesired heavy metal ions and for the isolation of valuable substances present in ion form in various solutions. The process of metal ion reduction is carried out using ion exchangers. The mechanism of this process is still incompletely clear and is difficult to describe theoretically. Exact descriptions of many experimental relations established for ion exchange can be obtained based on an analysis of the equation of adsorption isotherm under the conditions of mixed diffusion kinetics. However, the solution of this problem requires the application of special mathematical methods. For this reason, ion exchange processes are usually described in terms of simple physical models.

The process of ion exchange in liquid media is determined to a considerable extent by hydrodynamic factors. In addition, it is known [1] that heterogeneous transformations in liquids (i.e., processes at the phase boundaries or on the surface) include three main stages: (i) transfer of reactants to an interface where the reaction takes place; (ii) heterogeneous interaction; and (iii) removal of the reacted species from the reaction site. We will consider the case when a heterogeneous reaction proceeds in the diffusion region, since most heterogeneous processes employed in various technologies obey diffusion-controlled kinetics.

One of the most interesting applications of the diffusion kinetics is the process of heavy metal ion reduction from waste waters (wash solutions) of electrochemical works. Using ion exchangers of standard grades with preset properties, it is possible to increase the efficiency of ion exchange by acting upon the stage of external diffusion. It should be taken into account that this stage is determined predominantly by hydrokinetic factors, in particular, by the concentration of metal ions in solution and by the velocity of their passage through the ion exchanger. In this context, it is of interest to study the influence of these hydrokinetic factors on the efficiency of the ion exchange isolation of heavy metal ions. This paper presents the results of such investigations.

As was mentioned above, the process of heavy metal ion reduction from electrochemical wash solutions is effected with the aid of ion exchangers. These are fine-grained substances with a particle (grain) size on the order of 10^{-3} m. When a solution is passed through an ion exchanger, the exchanger grains occur in this solution in a suspended state. The solution is purified because metal ions are retained by the ion exchanger grains. The efficiency of the purification process depends on the exchange capacity of the medium [2], which is defined as the mass of metal ions absorbed per unit mass (1 kg) of the swelled ion exchanger. From the standpoint of physics, the exchange capacity characterizes a specific dynamic sorption capacity. In addition to the exchange capacity, the efficiency of the purification process is sometimes characterized by the bypass capacity, which is the mass of metal atoms absorbed per unit mass (1 kg) of the exchanger before these ions appear at the exchanger output. Experimental investigations are usually aimed at determining the exchange capacity, which is the main performance characteristic of an ion exchanger [3]. Evidently, an important factor determining the regime of solution purification is the rate of solution flow through the exchanger layer or, in terms of the Galilean (nonrelativistic) relativity principle [4], the velocity of exchanger grains relative to the solution.

Ion exchangers are substances capable of exchanging ions with a solution. These substances are subdi-

1063-7850/05/3104-0284$26.00

vided into highly disperse heterogeneous adsorbents and high-molecular-mass ion exchangers. Polymeric organic ion exchangers are frequently referred to as ion exchange resins [5]. The ion exchangers are also divided into anion exchangers and cation exchangers. The main laws of ion exchange are independent of the ion exchanger grain size and are retained both upon smearing of the phase boundaries and on the passage to gels, where phase boundaries in the strict physical sense are absent.

In this study, we have used an anion exchanger of the AV-17-8 grade in the OH^- form for the isolation of Cr(IV) ions from acid solutions; a cation exchanger of the KU-1 grade in the H^+ form for the isolation of Cu(II), Zn(II), and Cr(III) ions; and a cation exchanger of the KU-1 grade in the Na^+ form for the isolation of Ni(II) ions. The ion exchanger particles in all cases can be modeled as spherical grains. Therefore, the problem of solution purification can be reduced to determining the velocity distribution for a spherical particle falling down in a liquid medium. As is known, Stokes has successfully solved this problem [5] taking into account that (i) the velocity of a liquid medium streamlining a spherical particle decreases with the distance from the particle surface and (ii) the hydrodynamic layer is absent at the particle surface. However, a boundary diffusion layer is still formed near the surface [1]. For this reason, many physical problems can be correctly solved only by making allowance for such a layer, with the corresponding modification of the Stokes equation. The problem considered in this paper is also of this kind. As is known, the Stokes equation is valid for the Reynolds numbers $\mathrm{Re} \approx 0.5$ [1]. If the Prandtl number is about $\mathrm{Pr} = 10^3$, the Peclet number is $\mathrm{Pe} = \mathrm{RePr} \gg 1$ and, hence, the solution concentration will change within a thin boundary layer despite the fact that the liquid flow velocity varies in a smooth manner.

In the flow of a liquid medium, each grain of the ion exchanger moves under the action of the liquid pressure and the Stokes viscous force, which determine the acceleration of the grain. As was noted above, the ion exchanger grain can be considered as a ball of radius r. For such a ball with a density ρ_1 and a diameter $a = 2r$ uniformly falling down at a velocity of U in a liquid of density ρ_2, a modified Stokes equation taking into account the boundary layer is as follows:

$$\rho_1 g a = \rho_2 g \delta_0 + \frac{9}{2}\frac{U\delta_0\mu}{r^2}. \quad (1)$$

Here, $\rho_1 g a$ is the pressure produced by the moving ball upon the liquid, $\rho_2 g \delta_0$ is the pressure produced by the moving ball upon the liquid, $(9/2)U\delta_0\mu/r^2$ are the energy losses for friction, δ_0 is the boundary layer thickness, g is the acceleration of gravity, and μ is the dynamic viscosity of the liquid.

As is known, the diffusion layer thickness δ is related to δ_0 as

$$\delta = \left(\frac{D}{\nu}\right)^{1/3}\delta_0 = \frac{\delta_0}{\mathrm{Pr}^{1/3}}, \quad (2)$$

where D is the diffusion coefficient and ν is the kinematic viscosity. In addition, the ion exchanger density in the state of partial saturation is close to the solution density:

$$\rho_1 \approx \rho_2.$$

Then, taking into account that $\delta \approx 0.1\delta_0$ and using Eq. (1), we obtain the following formula for evaluating the ion exchanger grain size:

$$r \approx \frac{\delta}{0.2 - XU\delta}, \quad (3)$$

where $X = 6\pi\mu/mg$ and m is the mass of the ion exchanger grain.

The degree of saturation of the ion exchanger grain in solution can be evaluated using a model of the ball with a shell [6], which yields

$$F = 1 - \frac{6}{\pi^2}\exp\left(-\frac{D_g\tau\pi^2}{r^2}\right), \quad (4)$$

where D_g is the effective coefficient of metal ion diffusion in the ion exchanger grain and τ is the time of the ion exchanger saturation. By definition, the degree of saturation F is the ratio of the current exchange capacity Q to the limiting value Q_∞ (for $\tau \longrightarrow \infty$). Substituting expression (3) into formula (4), we obtain a relation between the exchange capacity and the solution flow velocity:

$$Q = Q_\infty - Q_\infty\frac{6}{\pi^2}\exp\left[-\frac{D_g\tau\pi^2(0.2 - XU\delta)^2}{\delta^2}\right]. \quad (5)$$

An analysis of this expression shows that it exhibits an extremum at $U_0 = 0.2/X\delta$.

An analogous expression describes the relation between the current exchange capacity Q and the metal ion concentration C_m in solution. This relation follows from an equation for the maximum diffusion flux j of metal ions toward the grain surface:

$$j = -D_n\frac{C_\mathrm{m}}{\delta},$$

where D_n is the diffusion coefficient for metal ions in solution.

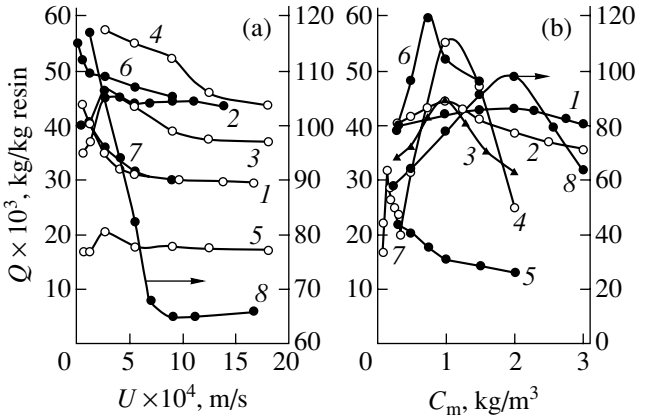

Fig. 1. Plots of the exchange capacity Q: (a) versus the solution flow velocity U for the metal ion concentrations C_m = 1.0 (*1–6*, *8*) and 0.15 kg/m^3 (*7*); (b) versus the initial concentration C_m of metal ions in solution for the flow velocity $U \times 10^4$ = 2.0 (*1*, *2*, *4*, *7*, *8*), 1.0 (*3*), and 0.5 m/s (*5*, *6*). The experimental data refer to the reduction of copper from (*1*) sulfuric and (*2*) silicon fluoride solutions; zinc from (*3*) sulfuric, (*4*) ammonium chloride, and (*5*) zincate solution; nickel (*6*); chromium(III) (*7*); and chromium(VI) (*8*).

In order to verify the results of these calculations, we have performed a series of experiments. The exchange capacity was determined by graphical integration of the curves of metal ion concentration at the exchanger output versus the volume of passed solution. These curves were obtained for various initial concentrations of metal ions in the liquid phase and for various velocities of the liquid flow. The experiments were performed with the ion exchanger in glass columns with an internal diameter of 1.6×10^{-2} m and a diameter to ion exchanger height ratio of 1 : 9. The output solutions were analyzed for content of metal ions (copper, zinc, nickel, and chromium) by methods of atomic absorption spectroscopy, spectrophotocolorimetry, and photocolorimetry. The measurements were performed using standard procedures on the Saturn S-115 and SF-26 spectrophotometers and a KFK-3 photocolorimeter [7, 8].

The results of our experiments showed that, as the velocity U of solution passing through the ion exchanger was increased, the exchange capacity Q in all cases exhibited a general tendency to decrease (Fig. 1a). This is probably explained by a decrease in the duration of contact between phases, that is, in the time for which the elementary volume of liquid passes through the ion exchanger layer. However, in some cases (Fig 1a, curves *2*, *3*, and *5*), the plots of Q versus U exhibited maxima. The appearance of these features can be related to the fact that the ion exchange efficiency is determined by diffusion in a thin subsurface layer rather than above the grain. Indeed, relation (5) yields

$$(\partial^2 Q/\partial z^2) = 12 Q_\infty \frac{D_g \tau}{\delta^2},$$

where $z = 0.2 - XU\delta$ and the derivative is taken at the point $z = 0$. If the diffusion process over the ion exchanger surface were predominant, then $\delta^2 > 0$ and the function $Q = f(U)$ would exhibit a minimum at $U = U_0$, which disagrees with experiment (Fig. 1a). This function would exhibit a maximum only provided that $\delta^2 < 0$, which implies predominance of a diffusion process in the subsurface layer of the ion exchanger.

The thickness $\tilde{\delta}$ of a subsurface layer of the ion exchanger featuring the dominant diffusion process can be evaluated using the formula

$$\tilde{\delta} = \frac{0.4}{9} \frac{g r^3}{\nu U_0}. \quad (6)$$

Substituting the values of parameters $r \cong 10^{-3}$ m, $U_0 \cong 1/3600$ m/s, $g \cong 10$ m/s^2, and $\nu \cong 10^{-2}$ m^2/s (viscosity in the subsurface region of the ion exchanger grain), we obtain $\tilde{\delta} = 1.6 \times 10^{-4}$ m.

Now, let us estimate the diffusion coefficient of metal ions in the aforementioned subsurface layer. Using the above estimate of the subsurface diffusion layer thickness, we obtain

$$D_0 \cong U_0 \tilde{\delta} \cong 4.5 \times 10^{-7} \text{ m}^2/\text{s}.$$

A comparison of this D_0 value to the diffusion coefficient of metal ions in solution, $D_n = 10^{-9}$ m^2/s [9] shows that $D_0 \gg D_n$. This inequality explains the appearance of maxima on the curves of $Q = f(U)$. By the same token, we can explain the origin of maxima on the curves of $Q = f(C_m)$ presented in Fig. 1b.

The motion of metal ions through pores of the thin subsurface layer of the ion exchanger grain is determined by the structure of pores and by the adsorption of water molecules on the pore walls. The degree of filling of the pore surface by water molecules is described by the adsorption isotherm. The presence of adsorbed water molecules on the pore walls significantly influences the process of metal ion diffusion in these pores: it is obvious that the diffusion of ions in empty pores and in those covered by adsorbed water molecules is described by different diffusion coefficients. We believe that high permeability of a thin subsurface layer in the cation exchanger grain is determined by the variety and the complicated structure of pores. Indeed, the pores may differ both in diameter and in configuration; in some pores, the diameter varies along the length and some regions may behave as ion channels [10]. As is known, the characteristic ion transport time in such channels may be as short as 10^{-8} s. In our case, the total time of ion penetration through the thin subsurface layer is on the order of 10^{-2} s. This is possible provided that D_0 is an effective diffusion coefficient of metal ions in the subsurface layer.

REFERENCES

1. V. G. Levich, *Physicochemical Hydrodynamics* (Fizmatgiz, Moscow, 1959; Prentice-Hall, Englewood Cliffs, 1962).
2. S. V. Plokhov and M. G. Mikhalenko, Izv. Vyssh. Uchebn. Zaved., Khim. Khim. Tekhnol. **45**, 155 (2002).
3. S. V. Plokhov and N. A. Barinova, Ékol. Prom-st Ross., No. 9, 9 (2001).
4. L. D. Landau and E. M. Lifshitz, *Course of Theoretical Physics*, Vol. 1: *Mechanics* (Nauka, Moscow, 1982; Pergamon, New York, 1988).
5. N. E. Kochin, I. A. Kibel', N. V. Roze, and J. R. M. Radok, *Theoretical Hydromechanics* (GITTL, Moscow, 1955; Interscience, New York, 1964), Vol. 2.
6. Yu. A. Kokotov and V. A. Pasechnik, *Equilibrium and Kinetics of Ion Exchange* (Khimiya, Leningrad, 1970) [in Russian].
7. *GOST* (State Standard) *22001-87: Reagents and High-Purity Substances. Method of Atomic-Absorption Spectroscopy. Determination of the Impurities of Chemical Elements* (Standartizdat, Moscow, 1987).
8. Yu. Yu. Lur'e and A. I. Rybnikova, *Chemical Analysis of Industrial Waste Waters* (Khimiya, Moscow, 1974) [in Russian].
9. B. P. Nikol'skiĭ, O. N. Grigorov, M. E. Pozin, B. A. Poraĭ-Koshits, V. A. Rabinovich, F. Yu. Rachinskiĭ, P. G. Romankov, and D. A. Fridrikhberg, *Handbook of Chemistry* (Khimiya, Moscow, 1964), Vol. 3 [in Russian].
10. V. Ya. Antonchenko, A. S. Davydov, and V. V. Il'in, *Fundamentals of Physics of Water* (Naukova Dumka, Kiev, 1991) [in Russian].

Translated by P. Pozdeev

Technical Physics Letters, Vol. 31, No. 4, 2005, pp. 288–289. Translated from Pis'ma v Zhurnal Tekhnicheskoĭ Fiziki, Vol. 31, No. 7, 2005, pp. 40–44.

The Effect of γ Radiation on the Temperature Dependence of the Surface Generation Velocity at a Si–SiO_2 Interface

P. B. Parchinskiĭ*, L. G. Ligaĭ, Kh. Zh. Mansurov, and Sh. Kh. Iulchiev

National University of Uzbekistan, Tashkent, Uzbekistan

** e-mail: pavelphys@mail.ru*

Received November 5, 2004

Abstract—We have studied the effect of γ radiation on the generation characteristics of a silicon–silicon dioxide (Si–SiO_2) interface formed upon thermal oxidation of the surface of silicon. The irradiation leads to the appearance of a temperature dependence of the surface generation velocity. This effect is related to the formation of radiation-induced traps capable of exchanging trapped carriers with the bulk of a semiconductor by means of tunneling emission. © *2005 Pleiades Publishing, Inc.*

Thermal oxidation of silicon is among the main technological processes involved in semiconductor device manufacturing. This process leads to the formation of a silicon–silicon dioxide (Si–SiO_2) interface that has a significant and, in many cases, decisive influence on the parameters of semiconductor devices and heterostructures. One of the principal characteristics determining the quality of this interface is the velocity of surface generation of charge carriers (S_g) [1, 2]. The S_g value is usually determined using the method of isothermal relaxation of capacitance in the structures of the metal–insulator–semiconductor (MIS) type [2, 3]. According to the concepts underlying this method, S_g is independent of the temperature [1, 3]. However, our recent analysis [4] showed that the presence of trapping centers capable of exchanging carriers with the bulk of semiconductor by means of tunneling and/or tunneling-assisted field emission may lead to the appearance of temperature dependence of the surface generation velocity. The trapping centers can appear in the SiO_2 layer both in the course of its formation and under the action of external factors, in particular, under irradiation. In this context, we have studied the effect of γ radiation on the temperature dependence of S_g at the Si–SiO_2 interface formed upon thermal oxidation of the surface of silicon.

The samples containing a Si–SiO_2 interface were prepared by thermal oxidation of the surface of *n*-type ⟨100⟩-oriented single crystal silicon wafers with a resistivity of 0.3 Ω cm. The technology of silicon oxidation and subsequent preparation of the test MIS structures was analogous to that described in [5]. The sample structures were irradiated by γ quanta at a dose of 10^6 rad using a ^{60}Co source. This treatment was performed in the dark, without applying a bias voltage to the field electrode.

The process of relaxation of the nonequilibrium capacitance was studied using a 150-MHz probing signal. The sample structure, occurring in the state of inversion at a bias voltage of V_1, was converted to the state of deeper inversion by applying a voltage pulse of amplitude ΔV. In this regime, it was possible to neglect a contribution to the surface generation current related to the recharging of the surface states [6]. The necessary bias voltage V_1, determined using the method of high-frequency capacitance–voltage characteristics, was $V_1 = -16$ and -30 V for the samples before and after irradiation, respectively. This difference is related to the radiation-induced accumulation of a positive charge in the SiO_2 layer and at the Si–SiO_2 interface [7]. The ΔV value was −4 V for both irradiated and unirradiated samples.

The typical experimental temperature dependences of S_g measured in the interval from −40 to 20°C for one of the sample structures before and after the exposure to γ radiation are presented in the figure. As can be seen from these data, S_g measured before irradiation is practically constant (to within the experimental error) in the entire range of temperature variation. Exposure to γ quanta leads to an increase in the S_g value and renders this value dependent on the temperature. The appearance of the temperature dependence of S_g upon irradiation was observed in all samples despite a considerable scatter in S_g values both before and after exposure. It should be noted that the scatter in S_g even for the MIS structures prepared in the same technological cycle is typical of the Si–SiO_2 interface and, according to [8], is related to fluctuations of the surface potential in the interface plane.

Let us consider in more detail a mechanism responsible for the appearance of the temperature dependence of S_g. According to the model developed in [4], the sur-

1063-7850/05/3104-0288$26.00 © 2005 Pleiades Publishing, Inc.

face generation velocity determined by the method of isothermal relaxation of the MIS capacitance can be expressed as

$$S_g = (I_s + I_t)/(qn_iA), \quad (1)$$

where q is the electron charge, n_i is the intrinsic density of charge carriers in the semiconductor, A is the area, I_s is the current due to the surface generation, and I_t is the current due to the tunneling and/or tunneling-assisted activation recharging of the trapping centers in the insulator. The I_s value is determined by the concentration of the surface generation centers and obeys the same law as the intrinsic charge carrier density n_i [1, 3]. For this reason, the ratio $I_s/(qn_iA)$ on the right-hand side of relation (1) is independent of temperature. The I_t current component is determined by the concentration of trapping centers in the insulator layer adjacent to the interface. This value also does not depend (or weakly depends) on the temperature [1]. Therefore, the ratio $I_t/(qn_iA)$ on the right-hand side of relation (1) and, hence, the total S_g value, will increase with decreasing temperature. If the concentration of trapping centers in the SiO_2 layer is low, the I_t value is small as compared to I_s, and the S_g value is determined by the temperature-independent part of relation (1). Thus, the absence of the temperature dependence of S_g in unirradiated MIS structures is indicative of a high quality and homogeneity of the SiO_2 layer.

The irradiation with γ quanta leads to a significant increase in the concentration of trapping centers in the SiO_2 layer and the surface generation centers, which accounts for the increase in both I_s and I_t. In the case of a considerable increase in the concentration of trapping centers in the SiO_2 layer, the term $I_t/(qn_iA)$ significantly contributes to the S_g value. According to the above analysis, this leads to the appearance of the temperature dependence of the surface generation velocity.

Thus, the observed temperature dependence of the surface generation velocity S_g in irradiated MIS structures is caused by an increase in the concentration of trapping centers in the SiO_2 layer adjacent to the $Si–SiO_2$ interface. It should be noted that, since the temperature dependence of S_g is determined by the presence of defects in the insulator region adjacent to the interface, measurements of the temperature dependence of the surface generation velocity in MIS structures can be used for monitoring the quality of insulator layers formed on the silicon surface in the course of device fabrication.

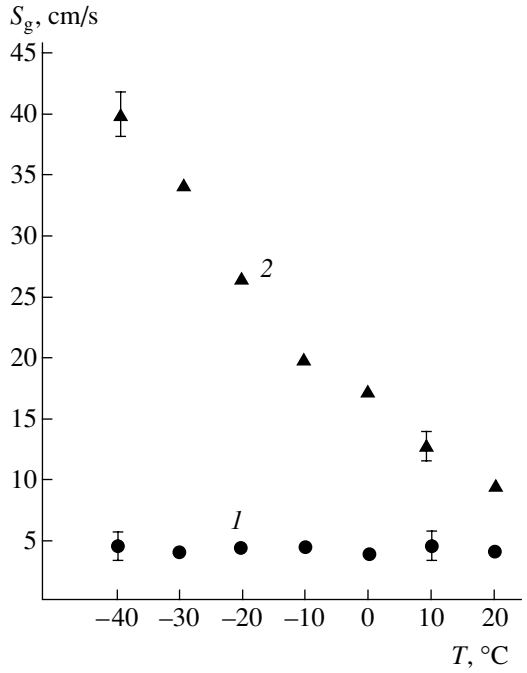

The temperature dependences of S_g at the $Si–SiO_2$ interface measured (*1*) before and (*2*) after the exposure to γ radiation.

REFERENCES

1. V. G. Litovchenko and A. P. Gorban', *Principles of the Physics of Metal–Insulator–Semiconductor Structures for Microelectronics* (Naukova Dumka, Kiev, 1978) [in Russian].
2. M. Zerbst, Z. Angew. Phys. **22**, 3039 (1966).
3. S. I. Kang and D. K. Schroder, Phys. Status Solidi A **89**, 13 (1985).
4. S. I. Vlasov, P. B. Parchinskiĭ, and L. G. Ligaĭ, Mikroélektronika **32**, 121 (2003).
5. P. B. Parchinskiĭ, S. I. Vlasov, R. A. Muminov, *et al.*, Pis'ma Zh. Tekh. Fiz. **26** (10), 40 (2000) [Tech. Phys. Lett. **26**, 420 (2000)].
6. L. S. Berman and A. A. Lebedev, *Deep Level Transient Spectroscopy in Semiconductors* (Nauka, Leningrad, 1981) [in Russian].
7. V. S. Pershenkov, V. D. Popov, and A. V. Shal'nov, *Surface Radiation Effects in Integrated Circuits* (Énergoatomizdat, Moscow, 1988) [in Russian].
8. E. I. Gol'dman and A. G. Zhdan, Fiz. Tekh. Poluprovodn. (St. Petersburg) **29**, 428 (1995) [Semiconductors **29**, 219 (1995)].

Translated by P. Pozdeev

Technical Physics Letters, Vol. 31, No. 4, 2005, pp. 290–292. From Pis'ma v Zhurnal Tekhnicheskoĭ Fiziki, Vol. 31, No. 7, 2005, pp. 45–50.

A Novel Temperature Sensor and Variable Optical Attenuator Based on a High-Birefringence Fiber Loop Mirror¶

Y. Yan[a,*], Q. Zhao[a], S. Chen[a,b], L. Liu[a], H. Zhang[a], G. Huang[a], S. Gao[a], and X. Dong[a]

[a] *Institute of Modern Optics, Nankai University, Tianjin 300071, China*

[b] *Mathematics and Physics Department, University of Petroleum, Beijing 102249, China*

** e-mail: yanyu@mail.nankai.edu.cn*

Revised manuscript received October 15, 2004

Abstract—A novel variable optical attenuator based on a high-birefringence fiber loop mirror is described. The fiber loop mirror is placed in a controlled-temperature chamber. As the temperature is increased, the transmission spectrum exhibits a shift, while virtually not changing its shape. The degree of attenuation at a wavelength of 1558 nm exceeds 30 dB, while the introduced losses are about 2.5 dB. The temperature-induced shift of the spectrum is strictly linear. The response of the temperature sensor based on this effect is linear with a correlation coefficient of 0.9997. The obtained experimental data are interpreted based on the results of numerical modeling. © *2005 Pleiades Publishing, Inc.*

Introduction. Variable optical attenuators (VOAs) are important elements in fiber-optic communication systems, which are usually employed for the absorption or reflection of background light. VOAs are also frequently used for controlling the optical power level in fiber-optic communication networks (both short and extended) with dense wavelength division multiplexing (DWDM), for monitoring the level of losses in such systems, and for solving some other tasks. In recent years, various types of VOAs have been suggested, including acoustooptic [1], thermo-optic [2], and microelectromechanical [3–5] devices, and silicon-on-insulator waveguide structures [6].

This paper reports on the design and working characteristics of a novel VOA based on a highly birefringent fiber loop mirror. We observed a shift of the transmission spectrum of this device in response to the fiber temperature variation and measured the attenuation characteristics at a preset wavelength, which showed good prospects for practical applications of the proposed device. The new VOA offers a number of advantages, including a broad attenuation band, independence of the polarization, low introduced losses, simple design, and good reproducibility. We have also established that the spectrum shifts strictly linearly with the temperature (with a linear correlation coefficient as high as 0.9997). When the temperature changes from 20 to 65°C, the transmission peak shifts by approximately 20 nm. The obtained experimental data agree well with results of numerical modeling.

Operation principle and experimental setup. Figure 1 shows a schematic diagram of the proposed VOA. The attenuator is based on a mirror comprising an optical fiber loop with a highly birefringent (HB) fiber insert. The principle of device operation can be briefly outlined as follows. The incident light is divided by a 3-dB fiber coupler into two waves propagating in the fiber loop in the opposite directions and having different polarization components. These waves pass the HB fiber section with different velocities, exhibit a change in polarization, and interfere upon leaving this section. Let L be the active fiber section length and B be the difference of the effective refractive indices of this section for the "fast" and "slow" waves. In accordance with the above considerations, the transmission coefficient of this device can be expressed as [7]

$$T = [1 - \cos\Delta\Phi(\lambda)]/2, \quad (1)$$

where $\Delta\Phi = 2\pi BL/\lambda$ is the resulting phase difference between the fast and slow wave components. Thus, the transmission spectrum is described by a cosine function with the argument involving the phase difference

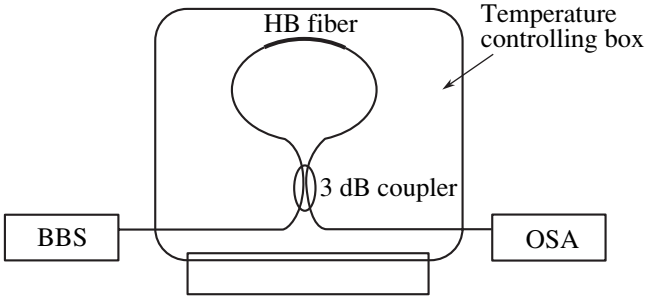

Fig. 1. Schematic diagram of the VOA (see the text for explanations).

¶ This article was submitted by the authors in English.

1063-7850/05/3104-0290$26.00 © 2005 Pleiades Publishing, Inc.

dependent on the wavelength, the HB fiber length L, and the birefringence B.

In our experiments, the beat length of the HB fiber was 3.1 mm at a wavelength of 1558 nm. In order to provide for the required accuracy, we have used an HB fiber section with L = 24.4 cm. The input signal was delivered from a broadband source (BBS) operating in a wavelength range from 1525 to 1565 nm. The output spectrum was measured with the aid of an ADVANTEST Q8383 optical spectrum analyzer (OSA). The fiber loop was placed into a controlled-temperature chamber, in which the temperature could be set accurately to within 0.1°C. According to formula (1), the phase shift $\Delta\Phi$ can be varied by controlling the temperature, which will produce a shift of the transmission spectrum and a change in the optical losses at 1.55 μm.

Experimental results. Figure 2 presents the transmission spectra of the proposed VOA measured at 26°C and upon increasing the temperature to 43°C. As can be seen, the increase in the temperature leads to a shift of the spectrum such that the maximum transmission at 1558 nm is –2.5 dB at 26°C and –37.5 dB at 43°C. Thus, a change in the optical losses at this wavelength amounts to 35 dB. At the same time, the period of modulation of the transmission spectrum changes rather insignificantly. The level of introduced losses is about 2.5 dB and is mostly due to the fiber connections. By improving the quality of joints, it is possible to reduce the level of introduced losses.

Figure 3 shows the attenuation characteristic of the proposed VOA in the region of 1.55 μm. As can be seen from these data, the VOA exhibits quite good attenuation properties. By controlling the temperature to within 0.1°C, it is possible to effectively modify the level of extinction at the given wavelength.

Since the transmission spectrum shifts in response to a change in the phase difference $\Delta\Phi$, it was of interest to establish a relation between the wavelength and the temperature. This experimental dependence is plotted in Fig. 4. As can be seen, the wavelength shift is a linear function of the temperature, and the linear correlation coefficient is 0.9997. It should be noted that the proposed VOA operates in a broad wavelength range of about 1.55 μm and shows good transmission properties. Moreover, owing to the high linear correlation coefficient, the VOA can be used as a temperature sensor. As the temperature changes from 25 to 60°C, the maximum of the transmission spectrum shifts by ~20 nm with a temperature sensitivity coefficient of 0.6255 nm/K. Thus, the sensor is highly linear and can operate in a quite broad temperature range. The results of multiply repeated analyses showed that the device is highly stable, which is evidence in favor of a high potential in various applications.

Numerical modeling. Figure 5 presents the results of numerical modeling of the experiment described above. According to the obtained experimental data, formula (1) involves two factors responsible for a shift of the trans-

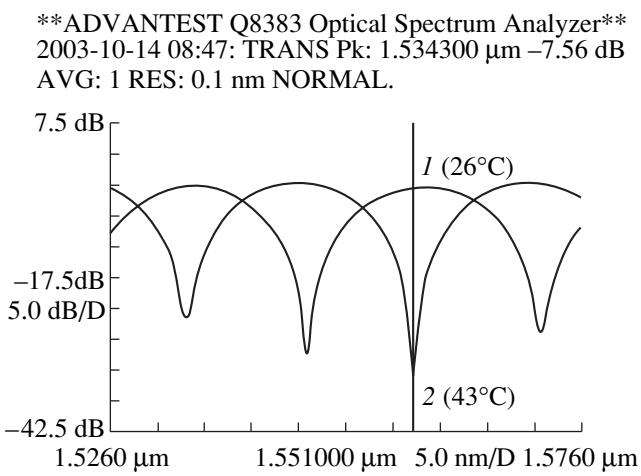

Fig. 2. The transmission spectra of the VOA measured at (*1*) 26°C and (*2*) 43°C.

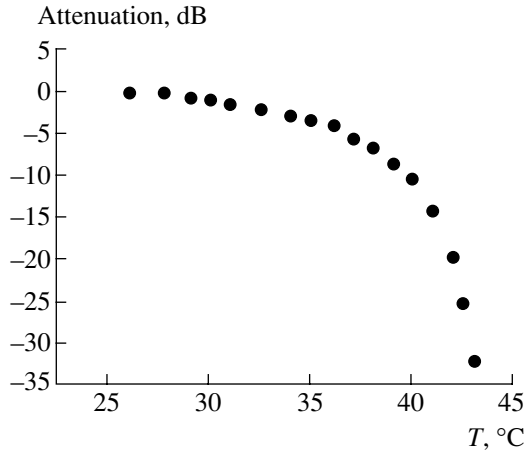

Fig. 3. The experimental attenuation characteristic of the VOA in the region of 1.55 μm.

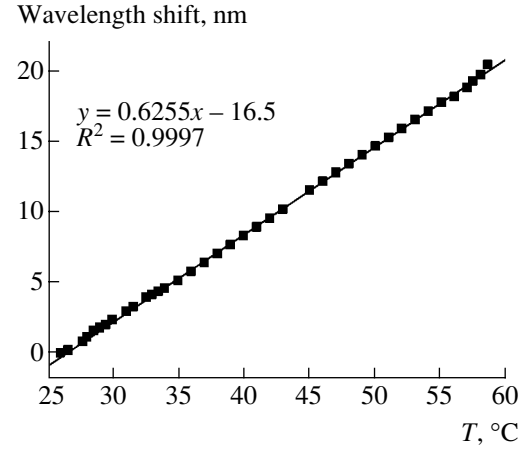

Fig. 4. An experimental plot of the wavelength shift versus temperature (points) and its linear approximation (solid line).

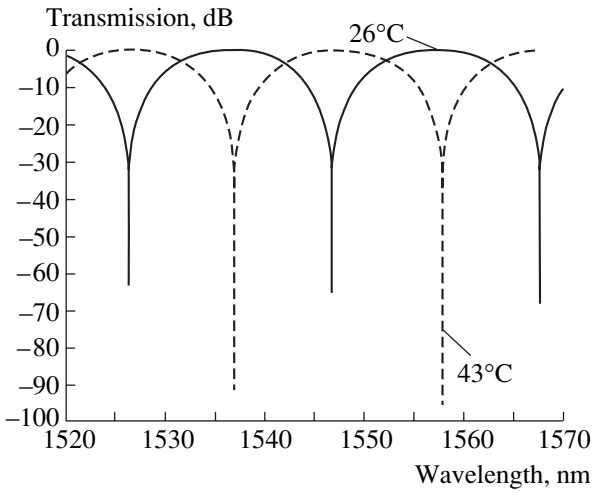

Fig. 5. Model transmission spectra calculated for the VOA with L = 24.2 cm at a temperature of 26 and 43°C.

mission spectrum in response to temperature variations. The first is the fiber length L, which increases with the temperature. The thermal expansion coefficient of the optical fiber is about 10^{-6} m/K. The second temperature-sensitive factor is the birefringence B, that is, the difference between the refractive indices for the fast and slow waves. This change is related to an elliptic deformation of the fiber upon heating. According to the experimental data, an increase in the temperature shifts the spectrum toward lower wavelengths despite the fact that the fiber length increases. Theoretically, in order to provide for the observed variation, the difference of the refractive indices must increase approximately by $\sim 10^{-6}$. In order to quantitatively explain the experimental results, it is necessary to perform theoretical analysis based on a more adequate model.

Conclusions. We described a novel VOA based on a highly birefringent fiber loop mirror. The proposed device has a number of advantages, including a broad attenuation band, independence of the polarization, low introduced losses, simple design, and good reproducibility. It was demonstrated that the VOA can be used as a base for the development of a temperature sensor with a highly linear scale. A model qualitatively explaining the experimental results has been presented.

Acknowledgments. This study was supported by the National Natural Science Foundation of China (project no. 69977006), the Special National Science Foundation of Tianjin (project no. 013800511), and the Doctoral Program Support Foundation of the Ministry of Education of China (project no. 20020055036).

REFERENCES

1. Q. Li, A. A. Au, C. H. Lin, *et al.*, IEEE Photonics Technol. Lett. **14**, 1563 (2002).
2. F. R. Akkari, K. H. Cazzini, and W. Blau, J. Non-Cryst. Solids **187**, 494 (1995).
3. X. M. Zhang, A. Q. Liu, C. Lu, *et al.*, Electron. Lett. **38**, 382 (2002).
4. X. H. Dai, X. L. Zhao, W. J. Li, *et al.*, Proc. SPIE **4601**, 97 (2001).
5. B. M. Anderson, S. Fairchild, N. Thorsten, *et al.*, in *Proceedings of the Optical Fiber Communication Conference (OFC-2000), Baltimore, 2000*, Vol. 10, p. 260.
6. A. Vonsovici, I. E. Day, A. A. House, *et al.*, Proc. SPIE **4293**, 1 (2001).
7. S. Yang, H. Meng, S. Yuan, *et al.*, Chin. J. Lasers **10**, 868 (2001).

Technical Physics Letters, Vol. 31, No. 4, 2005, pp. 293–294. Translated from Pis'ma v Zhurnal Tekhnicheskoĭ Fiziki, Vol. 31, No. 7, 2005, pp. 51–55.

Influence of the Carrier Gas Composition on Metalorganic Vapor Phase Epitaxy of Gallium Nitride

W. V. Lundin*, E. E. Zavarin, and D. S. Sizov

Ioffe Physicotechnical Institute, Russian Academy of Sciences, St. Petersburg, 194021 Russia

** e-mail: lundin.vpegroup@mail.ioffe.ru*

Received November 3, 2004

Abstract—The influence of hydrogen and nitrogen as carrier gases on the rates of gallium nitride (GaN) growth and etching in the process of metalorganic vapor phase epitaxy (MOVPE) have been studied. Based on these data, the possible roles of hydrogen and nitrogen in the events on the surface of an epitaxial GaN layer are considered. © *2005 Pleiades Publishing, Inc.*

Despite considerable progress in the technology of gallium nitride (GaN) structures obtained by means of metalorganic vapor phase epitaxy (MOVPE), the mechanism of GaN layer growth in the course of this process is still insufficiently studied. In particular, the influence of the carrier gas type on the MOVPE of GaN is unclear. The MOVPE of III–V semiconductor compounds (including GaN) is usually performed using hydrogen as a carrier gas, which is related to the easy and effective purification of this gas with the aid of palladium diffusion cells. However, GaN is chemically unstable in hydrogen and hydrogen–ammonia gas mixtures. Switching off the flow of trimethylgallium (TMG) in the reactor under the conditions typical of the MOVPE of GaN leads to etching of the GaN layer [1]. The nature of this instability and its possible influence on the process of epitaxial growth have not been studied so far. It was reported about using nitrogen [2, 3] and nitrogen–hydrogen mixtures [4, 5] as carrier gases in MOVPE of GaN. However, these communications were devoted primarily to the properties of obtained GaN structures rather than to the features of the epitaxial process.

This Letter reports the results of our systematic investigation of the rates of GaN growth and etching during MOVPE depending on the reactor temperature, the carrier gas composition, and the TMG flow rate.

The experiments were performed in a modified MOVPE system of the Epiquip VP-50 RP type using TMG and ammonia as the sources of components. The gas blending system made it possible to use a nitrogen–hydrogen mixture of arbitrary composition as the carrier gas. The rates of GaN growth and etching were determined using the method of laser reflectometry [1]. Epitaxial layers of GaN on sapphire grown in AIX2000 HT system were used as substrates.

Each experiment was started with the growth of a GaN layer on a quasi-GaN substrate under standard conditions established for the Epiquip VP-50 RP system [6]. Then, the reactor temperature and the carrier gas composition were changed (while the ammonia flow and the total flow remained unchanged) and the rates of GaN growth (with TMG flow on) and etching (with TMG flow off) under the modified conditions were determined. All experiments can be subdivided into three series.

In the first series of experiments, the carrier gas was nitrogen. In this case, the growth rate was directly proportional to the TMG flow rate and did not depend on the reactor temperature (Fig. 1). Switching off the TMG flow did not lead to the etching of GaN. In the second series, where the carrier gas was hydrogen, the growth rate was also directly proportional to the TMG flow rate. However, the extrapolation of this dependence to a zero TMG flow rate intersects the ordinate axis below zero, which corresponds to etching (see the inset to Fig. 1). Direct measurement of the etching rate with the TMG flow switched off (Fig. 1) gave a value coinciding

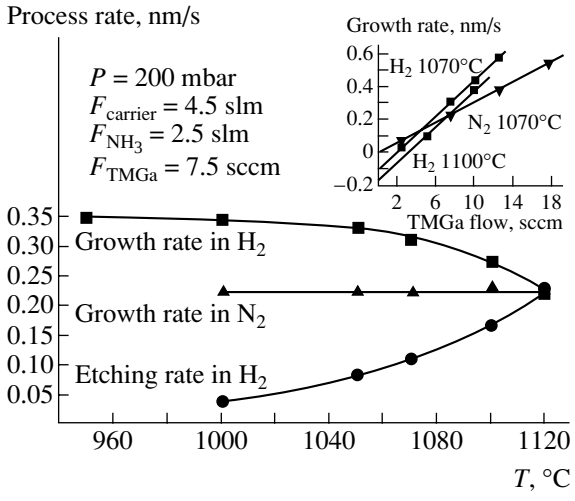

Fig. 1. Plots of the GaN growth and etching rates versus reactor temperature and TMG flow rate [slm = standard liter per minute; sccm = standard cubic centimeter per minute].

1063-7850/05/3104-0293$26.00 © 2005 Pleiades Publishing, Inc.

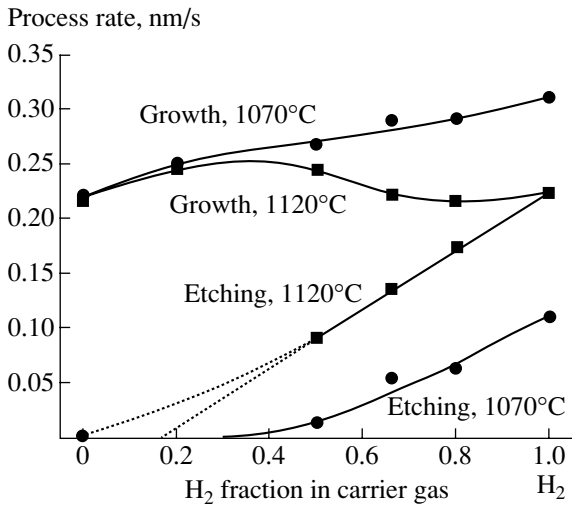

Fig. 2. Plots of the GaN growth and etching rates versus carrier gas composition (H_2/N_2 ratio) at 1070 and 1120°C.

with that determined by extrapolation of the growth rate as a function of the TMG flow rate. An increase in the reactor temperature led to a decrease in the growth rate and an increase in the etching rate.

In the third series, the experiments were performed using a nitrogen–hydrogen mixture as the carrier gas. The rates of GaN growth and etching were studied as dependent on the ratio of nitrogen and hydrogen in the mixture. Figure 2 shows the results of such experiments performed at two temperatures (1070 and 1120°C). On the whole, the observed behavior reflects a competition between the growth and etching processes: no etching takes place in the hydrogen-free atmosphere, but the growth rate in the presence of hydrogen is higher (probably due to greater diffusion coefficients of the components, the sources of group III elements) than in pure nitrogen.

At 1070°C, the GaN growth rate monotonically decreases with increasing nitrogen content in the mixture (in agreement with the results presented in Fig. 1), but the behavior deviates from linearity (previously, an analogous observation was reported in [5]). The etching rate rapidly decreases with increasing nitrogen content in the reactor, and practically no etching takes place at a 1 : 1 ratio of nitrogen and hydrogen in the mixture. At 1120°C, the plot of the etching rate versus carrier gas composition is more regular, but it still deviates from linearity and more rapidly decreases with increasing nitrogen content. The growth rate at this temperature depends on the carrier gas composition in a complex nonmonotonic manner.

On the whole, the obtained results led us to the following preliminary conclusions.

(i) The possibility of etching should be taken into account in developing vapor transport technology for GaN structures, especially in cases when the growth has to be interrupted during the technological cycle.

(ii) Coincidence of the etching rates determined by direct measurements and by extrapolation of the growth rate as a function of the TMG flow rate indicates that the presence of TMG in the reactor does not influence the etching process and, hence, does not change the state of the growth surface.

(iii) Strong suppression of the etching of GaN observed upon adding nitrogen to the reactor atmosphere suggests that nitrogen is not chemically inert with respect to this process. Direct measurement of the dependence of the etching rate on the partial pressure of hydrogen (at a fixed partial pressure of ammonia) showed that the role of nitrogen cannot be explained in terms of simple dilution of hydrogen. It is possible that nitrogen prevents the removal of etching products from the surface via diffusion, thus increasing the probability of redeposition. At the same time, it is known that GaN is a catalyst of ammonia decomposition [7]. Assuming that the mechanism of the catalytic action of GaN is analogous to that of the typical metal catalysts (iron, nickel, etc.) used in the synthesis and decomposition of ammonia [8], we may suggest that the following processes take place on the GaN surface. Hydrogen molecules dissociate to atoms (GaN is probably etched by atomic hydrogen), while nitrogen molecules bind to gallium atoms on the GaN surface and become less strong. As a result, the surface of GaN is passivated and the nitrogen molecules with weak bonds may add hydrogen atoms with the formation of ammonia, thus preventing these atoms from interaction with GaN.

Acknowledgments. The authors are grateful to A.V. Fomin and R.A. Talalaev for fruitful discussions and to Yu.P. Yakovlev and P.S. Kop'ev for their support of this study.

REFERENCES

1. A. V. Sakharov, W. V. Lundin, I. L. Krestnikov, *et al.*, in *Proceedings of the International Workshop on Semiconductor Nitrides (IWN 2000), Nagoya, 2000*, Ed. by H. Amano and A. Wakahara.
2. S. Yamaguchi, M. Kariya, M. Kosaki, *et al.*, J. Appl. Phys. **89**, 7820 (2001).
3. O. Schon, B. Schineller, M. Heuken, *et al.*, J. Cryst. Growth **189**–**190**, 335 (1998).
4. S. Nakamura, Jpn. J. Appl. Phys. **30**, L1705 (1991).
5. H. X. Wang, Y. Amijima, Y. Ishihama, *et al.*, J. Cryst. Growth **233**, 681 (2001).
6. W. V. Lundin, A. V. Sakharov, A. F. Tsatsul'nikov, *et al.*, Fiz. Tekh. Poluprovodn. (St. Petersburg) **38**, 705 (2004) [Semiconductors **38**, 678 (2004)].
7. S. S. Liu and D. A. Stevenson, J. Electrochem. Soc. **125**, 1161 (1978).
8. N. L. Glinka, *General Chemistry* (Khimiya, Leningrad, 1983) [in Russian].

Translated by P. Pozdeev

Technical Physics Letters, Vol. 31, No. 4, 2005, pp. 295–297. Translated from Pis'ma v Zhurnal Tekhnicheskoĭ Fiziki, Vol. 31, No. 7, 2005, pp. 56–62.

Modification of the Near-Surface Layer of *n*-Si by Hydrogen Ions in a High-Voltage Pulsed Beam Discharge

V. P. Demkin[a], S. V. Mel'nichuk[b], and B. S. Semukhin[b]

[a] *Tomsk State University, Tomsk, 634050 Russia*

[b] *Institute of Strength Physics and Materials Science, Siberian Division, Russian Academy of Sciences, Tomsk, 634055 Russia*

Received October 4, 2004

Abstract—The near-surface layer of *n*-Si single crystal wafers has been subjected to microdoping by hydrogen ions in the plasma of a pulsed beam discharge. The resistivity and the current density of the samples have been studied as functions of the hydrogen treatment time. The hydrogen-modified *n*-Si samples exhibit photo emf. The results are interpreted within the framework of a qualitative model. © *2005 Pleiades Publishing, Inc.*

Introduction. The method of hydrogen microdoping of semiconductor materials in a pulsed beam discharge was originally described in [1]. A characteristic feature of this discharge is that the plasma contains an electron beam formed in the interelectrode gap between a cathode and a grid anode. The pressure in the gas discharge and the amplitude of the pulsed voltage applied to the electrodes are selected so that the electron component of the plasma in the interelectrode gap occurs predominantly in the runaway regime [2, 3]. The experimental data obtained by means of the polarization diagnostics [4] and the results of numerical simulations of the plasma gaskinetics [5] showed that accelerated electrons leaving the gap through the grid anode possess energies on the order of the applied potential difference and, hence, are characterized by high penetrating and ionizing ability. Using a flexible scheme developed for controlling the electron beam parameters, it is possible to obtain a plasma with desired parameters at a considerable distance from the interelectrode gap, which is an important prerequisite for solving problems related to controlled microdoping of semiconductors with hydrogen ions.

The results of our previous investigations [1] showed the possibility of controlled modification of the surface of semiconductor materials (in particular, GaAs) by treatment with hydrogen ions. It was found that this treatment leads to a change in the material structure in a near-surface layer, which becomes more homogeneous. This Letter presents the results of investigations of the structure and properties of another semiconductor material, namely, *n*-type silicon modified by hydrogen ions in a high-voltage pulsed beam discharge.

Experimental methods. The initial materials were *n*-type single crystal silicon wafers used for the fabrication of solar cells. A series of samples with dimensions 10×10 mm were cut from the same wafer.

The samples were prepared using an experimental setup and procedure described previously [1]. The samples were placed on a table situated outside the interelectrode gap and spaced by 15 mm from the grid anode. The discharge tube was evacuated and then filled with a mixture of helium (7 Torr) and hydrogen (1 Torr). The cathode was spaced by 0.9 mm from the grid anode with a transparency of 80%. The discharge was initiated and powered by high-voltage pulses with an amplitude of $U = 2$ kV, a duration of 2 μs, and a repetition rate of 2.5 kHz. The plasma temperature was 310–320 K. The samples were exposed to the plasma for various periods of time (3, 6, 9, 12. 15, 18, and 24 min); each treatment was studied in a set of three samples.

The charge carrier density was measured on a commercial system for determining the density of major carriers in *n*/*n* semiconductor materials, the resistivity was studied using an IUS-2 setup, and the conductivity type was determined using a TP-201 type device.

Experimental results and discussion. Figure 1 shows plots of the resistivity ρ and the current *I* versus duration *t* of the hydrogen treatment for the *n*-Si samples studied. As the treatment time increases to $t =$ 6 min, the resistivity decreases (curve *1*), while the current is virtually zero to within the experimental error (curve *2*). This behavior can be related to rearrangement of the block structure of silicon. Indeed, the

Experimental data of the photo emf in *n*-Si before and after 20-min modification with hydrogen ions

Illumination	Photo emf *U*, mV	
	unmodified	modified
Off	2	1
On	7	3

1063-7850/05/3104-0295$26.00

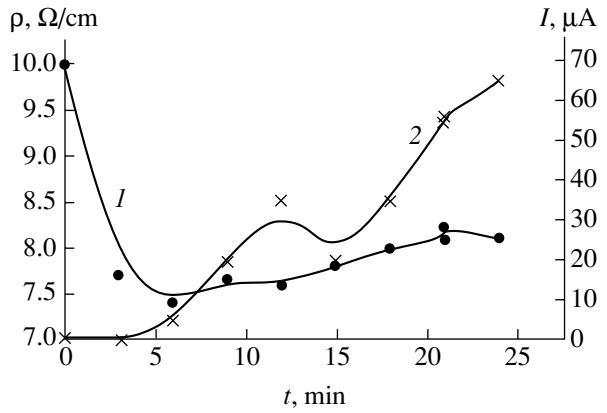

Fig. 1. Plots of (*1*) resistivity ρ and (*2*) current *I* versus duration *t* of the hydrogen treatment of single crystal *n*-Si samples.

results of X-ray diffraction measurements showed that the average block size decreased from 71 nm in the initial state to 43 nm for $t = 3$ min. In addition, the block size distribution function becomes more like a Gaussian curve, which is evidence of increasing order (and, accordingly, decreasing ρ) in the course of protonation.

Figure 2 shows images of the sample surface measured using an atomic force microscope (AFM) with a resolution of 6 nm before ($t = 0$) and after ($t = 3$ min) the treatment with hydrogen ions. As can be seen from these patterns, hydrogen implantation leads to a significant modification of the surface relief, which becomes more homogeneous in agreement with the results obtained previously [1].

The initial ($t \le 6$ min) decrease in the resistivity ρ relative to that of the untreated sample can be explained by the gradual saturation of a thin near-surface layer of *n*-Si with hydrogen ions and the development of a different conductivity type. This is consistent with a nearly zero current (which was below the sensitivity threshold of the TP-201 device employed). Antonova *et al.* reported [6] that hydrogen implantation into silicon lead to a change in the sample conductivity from *p* to *n* type during the first 0.5 h, while no such inversion was observed when the implantation time was increased to 3 h.

As the exposure of our samples in the plasma was increased above 6 min, both ρ and *I* exhibited growth, reaching 8.3 Ω/cm and 65 μA, respectively. This increase in the resistivity can be related to the formation of Si^{-}–H^{+} complexes and to a decrease in the fraction of Si^{-}–P^{+} complexes. Indeed, Mashin *et al.* [7] showed that linear structures of the Si–H or Si–H_2 types can form in real silicon crystals; moreover, large Si–H clusters can form when the concentration of such donor–acceptor centers is on the order of 10^{17} cm^{-3}.

Thus, we may suggest that the near-surface layer of *n*-Si upon hydrogen treatment consists of a large number of "pure" silicon atoms, a relatively small fraction of Si^{-}–P^{+} structures, and a very small amount of free hydrogen ions H^{+}. The gradient of the concentration of these components, which is most pronounced in the near-surface layer, leads to the appearance of an internal electric field. Note also that, according to [6], the ion range in the samples implanted to 10^{16} cm^{-2} reaches 0.5 μm. According to the results of our measurements, the modified layer thickness after a 15-min treatment is about 3–4 μm. Figure 3 presents an optical micrograph of the edge of a silicon sample treated with hydrogen ions for 15 min, where a dark band at the upper surface corresponds to the layer enriched with H^{+} ions.

The appearance of the internal electric field as a result of the polarization (predominantly in the form of Si^{-}–P^{+} type structures) leads to the formation of an electric double layer. The concentration of Si^{-}–P^{+} structures in the near-surface layer is much lower than that in deeper layers. This results in the development of photo emf upon illumination, since the charges are separated and the internal resistance is high. According to published data [8], the specific photo emf is proportional to the resistivity gradient. The increase in the photo emf is related to a decrease in the density of free charge carriers in the irradiated region of a semiconduc-

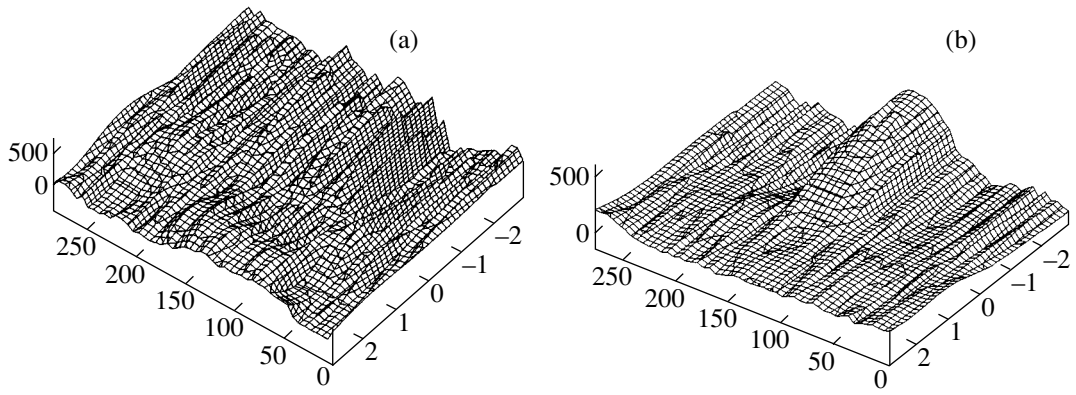

Fig. 2. AFM images of the *n*-Si single crystal sample surface (a) before and (b) after 3-min hydrogen treatment (scale: ×6 nm).

Fig. 3. An optical micrograph of the edge of a silicon sample treated with hydrogen ions for 15 min (magnification, ×500).

tor. We have performed measurements of the photo emf in the samples illuminated with radiation of an incandescent lamp before and after 20-min treatment with hydrogen ions. The results of these experiments are presented in the table. As can be seen, a change in the photo emf U for both the initial and hydrogen-treated surfaces are on the order of several millivolts, while the ratio of the values observed with and without illumination changes by a factor of about three. This result also confirms the above assumption concerning a decrease in the concentration of Si^{-}–P^{+} structures in the near-surface layer of hydrogen-treated samples.

Conclusions. (i) We have experimentally demonstrated a significant change in the structure and properties of the near-surface layer of *n*-Si as a result of treatment with hydrogen ions in a high-voltage pulsed beam discharge.

(ii) The observed behavior of the electric resistance and the appearance of photo emf are explained within the framework of a qualitative model based on the formation of Si^{-}–H^{+} complexes.

(iii) The method of hydrogen microdoping can be used for the creation of various structures for microelectronics and optoelectronics.

REFERENCES

1. V. V. Anisimov, V. P. Demkin, I. A. Kvint, *et al.*, Pis'ma Zh. Tekh. Fiz. **26** (7), 35 (2000) [Tech. Phys. Lett. **26**, 284 (2000)].
2. V. E. Golant, A. P. Zhilinskii, and S. A. Sakharov, *Fundamentals of Plasma Physics* (Atomizdat, Moscow, 1977; Wiley, New York, 1980).
3. P. A. Bokhan and G. V. Kolbychev, Zh. Tekh. Fiz. **51**, 2032 (1981) [Sov. Phys. Tech. Phys. **26**, 1057 (1981)].
4. V. P. Demkin, B. V. Korolev, and S. V. Mel'nichuk, Fiz. Plazmy **38** (1), 26 (1995) [Plasma Phys. Rep. **38** (1995)].
5. V. P. Demkin, B. V. Korolev, and S. V. Mel'nichuk, Fiz. Plazmy **21**, 81 (1995) [Plasma Phys. Rep. **21**, 76 (1995)].
6. I. V. Antonova, V. F. Stas', V. P. Popov, *et al.*, Fiz. Tekh. Poluprovodn. (St. Petersburg) **34**, 1095 (2000) [Semiconductors **34**, 1054 (2000)].
7. A. I. Mashin, A. F. Khokhlov, A. G. Razuvaev, *et al.*, Fiz. Tekh. Poluprovodn. (St. Petersburg) **33**, 1253 (1999) [Semiconductors **33**, 1139 (1999)].
8. Z. V. Basheleĭshvili and T. A. Pagava, Fiz. Tekh. Poluprovodn. (St. Petersburg) **33**, 924 (1999) [Semiconductors **33**, 845 (1999)].

Translated by P. Pozdeev

Technical Physics Letters, Vol. 31, No. 4, 2005, pp. 298–301. Translated from Pis'ma v Zhurnal Tekhnicheskoĭ Fiziki, Vol. 31, No. 7, 2005, pp. 63–69.

Resonance Drag of a Neutral Atomic Beam Caused by Near-Field Modes of a Fluctuational Electromagnetic Field at a Solid Surface

G. V. Dedkov

Kabardino-Balkarian State University, Nal'chik, Kabardino-Balkaria, Russia
e-mail: gv_dedkov@mail.ru
Received September 6, 2004

Abstract—Resonance drag losses have been studied by analytical and numerical methods for a neutral beam of 200–400-keV cesium atoms moving near a smooth solid surface bearing IR surface modes. The cases of pure ionic dielectrics, doped semiconductors, and the films of such substances on metal substrates are considered. For the films, the drag losses are approximately twice as large as those for the bulk substances. The theory predicts exponential growth of the drag losses with increasing temperature of the surface. © *2005 Pleiades Publishing, Inc.*

Evaluation of the drag losses for neutral atomic particles moving near a smooth solid surface is of principal importance in applications related to the development of nanotechnologies, in particular, to the creation of nanodimensional systems for the transport and focusing of charged and neutral particle beams [1, 2].

In recent years, a general theory [3–5] has been developed for a fluctuational-electromagnetic (contactless) interaction between moving neutral particles and the surface of a polarizable (solid) medium. In particular, this theory implies the possibility of a resonance interaction with the surface modes of the fluctuational-electromagnetic field for such particles moving in the region of nanometer distances from the surface. If the characteristic frequency of the surface mode (plasmon, phonon polariton, etc.) is ω_s and the particle (atom) excitation frequency is ω_{0n}, the resonance interaction condition is that

$$|\omega_s - \omega_{0n}| = \mathbf{kV}, \quad (1)$$

where $\mathbf{k}$ is the wavevector of the given surface mode and $\mathbf{V}$ is the particle velocity vector (which is assumed to be parallel to the surface). For a nonzero temperature of the solid surface ($T \neq 0$), the resonance interaction is additionally characterized by the conditions $\hbar\omega_s/k_BT \sim 1$ and/or $\hbar\omega_{0n}/k_BT \sim 1$; for $T \longrightarrow 0$, the interaction is exponentially small. It should be noted that no such temperature limitations were encountered in the earlier theory [6], because that model did not correctly take into account the possible thermal factors. Neutral atoms in a broad temperature range ($T < 10^3$ K) obey the condition $\hbar\omega_{0n}/k_BT \gg 1$. This is related to the fact that the frequencies of electron transitions from the ground states are large as compared to the Wien frequency $\omega_W = k_BT/\hbar$. On the other hand, the condition $\hbar\omega_s/k_BT \sim 1$ can be valid for many solid materials, (including semiconductors, dielectrics, and low-dimensional systems) possessing IR absorption. Taking into account these conditions and using the general results obtained in [3–5], we may infer that the resonance interaction of a moving atom with the surface electromagnetic modes always has a drag character. The case of $\hbar\omega_{0n}/k_BT \sim 1$ can be realized for a neutral nanodimensional particle, a cluster, or a strongly heated complex molecule. Note that, in the case of $\omega_{0n} < \omega_s$, the tangential forces are positive and, hence, accelerate the particle.

Since the practical observation of the effects under consideration in the relativistic case is hardly probable, let us restrict our analysis to a nonrelativistic case ($V/c \ll 1$, where c is the velocity of light) and consider the drag of a neutral atomic beam near the solid surface. In this case, condition (1) reduces to $k \gg |\omega_{0n} - \omega_s|/c$. For $\omega_{0n} \gg \omega_s$, this is equivalent to $k \gg \omega_{0n}/c$ and $k \gg \omega_s/c$. These conditions imply that we can use nonrelativistic equations obtained in [3, 4] and that the retardation effects can be completely ignored.

Below, we will consider the solid surfaces of several types characterized by low-frequency (IR) electromagnetic modes. These include (i) ionic dielectrics, (ii) doped semiconductors, and (iii) films of such a dielectric or semiconductor on a metal substrate. In the first two cases, the permittivities of bulk materials can be written in the standard form as

$$\varepsilon(\omega) = \varepsilon_\infty + \frac{\omega_T^2(\varepsilon_0 - \varepsilon_\infty)}{\omega_T^2 - \omega^2 - i\gamma\omega}, \quad (2a)$$

$$\varepsilon(\omega) = \varepsilon_\infty\left(1 - \frac{\omega_P^2}{\omega^2 + i\omega/\tau}\right), \quad (2b)$$

1063-7850/05/3104-0298$26.00

where ω_T is the transverse phonon frequency, ω_P is the plasma frequency, γ is the damping factor, τ is the charge carrier relaxation time, and ε_0 and ε_∞ are the static and high-frequency (optical) permittivities, respectively. In order to calculate the stopping power dE/dx for a neutral atom according to [3–5], it is necessary to obtain expressions for the imaginary part $\Delta''(\omega) = \mathrm{Im}\left\{\frac{\varepsilon(\omega)-1}{\varepsilon(\omega)+1}\right\}$ of the complex permittivity and for the atomic polarizability $\alpha''(\omega)$. Using relations (2a) and (2b), an expression for $\Delta''(\omega)$ in the presence of resonance absorption peaks can be written as

$$\Delta''(\omega) = \pi\omega_s f(\varepsilon_0, \varepsilon_\infty)\delta(\omega - \omega_s), \quad (3)$$

where the cases of (2a) and (2b) correspond to

$$f(\varepsilon_0, \varepsilon_\infty) = \frac{\varepsilon_0 - \varepsilon_\infty}{(\varepsilon_0 + 1)(\varepsilon_\infty + 1)}, \quad \omega_s = \omega_T\sqrt{\frac{\varepsilon_0 + 1}{\varepsilon_\infty + 1}},$$

$$f(\varepsilon_0, \varepsilon_\infty) = \frac{1}{(\varepsilon_\infty + 1)}, \quad \omega_s = \omega_T\sqrt{\frac{\varepsilon_\infty}{\varepsilon_\infty + 1}},$$

respectively. The resonance contribution to $\alpha''(\omega)$ can be expressed via the well-known quantum-mechanical formula

$$\alpha''(\omega) = \frac{\pi e^2 f_{0n}}{2m\omega_{0n}}\delta(\omega - \omega_{0n}), \quad (4)$$

where ω_{0n} is the frequency of the atomic transition from the ground state (0) to an excited state (n), f_{0n} is the oscillator strength, and e and m are the electron charge and mass, respectively.

Substituting expressions (3) and (4) into the general formula for the tangential fluctuational-electromagnetic force (see, e.g., [1, Eq. (60)], we obtain

$$\frac{dE}{dx} = -\frac{1}{32}\frac{e^2\hbar}{m}\frac{\omega_s}{\omega_{0n}}\frac{f_{0n}f(\varepsilon_0, \varepsilon_\infty)}{z_0^4\Delta\omega} \times\left[\exp\left(\frac{\hbar\omega_s}{k_B T}\right) - 1\right]^{-1} J(2\Delta\omega z_0/V), \quad (5)$$

$$J(x) = x^4(K_0(x) + K_2(x)), \quad (6)$$

where $K_{0,2}(x)$ is the Macdonald function, z_0 is the distance from the atom to the surface, and $\Delta\omega = |\omega_s - \omega_{0n}|$. Since the function $J(x)$ reaches a maximum at $x = 3.62$, where $J(3.62) = 7.86$, the particle velocity and the distance to the surface are related by a resonance condition $\Delta\omega z_0/V = 1.81$ (cf. condition (1)). If several atomic transitions have to be taken into consideration, formula (5) implies evident generalization via summation over the corresponding contributions.

It was shown [7] that the viscous drag (proportional to the velocity) can be much greater for a dielectric film of thickness d on a metal substrate than for a "pure" surface of the same bulk material. This is related to the appearance of two surface optical modes of the phonon polariton type at the film–substrate interface. Analogous (plasmon polariton) modes appear at the semiconductor–metal interfaces. Since these surface waves are characterized by a spatial dispersion, formula (3) has to be replaced (for $\omega_s = \omega_T$ or $\omega_s = \omega_P$) by

$$\Delta''(\omega) = \omega_s A(kd)\delta(\omega - \omega_s x(kd)), \quad (7)$$

where $A(kd)$ and $x(kd)$ are dimensionless quantities that also depend on the coefficients of permittivities of the corresponding materials. In the case of (2a), the expressions were obtained in [7]; for (2b), the expressions can be found in a similar way. For both modes, the function $x(kd)$ varies within small limits about unity, while the function $A(kd)$ exponentially decays with increasing wavenumber k.

The final expression for dE/dx is obtained by substituting relations (4) and (7) into the general formula for the tangential fluctuational-electromagnetic force [3, Eq. (60)]:

$$\frac{dE}{dx} = -\frac{1}{8\pi}\frac{e^2\hbar}{m}\frac{\omega_s}{\omega_{0n}}\frac{f_{0n}}{z_0^4\Delta\omega} = \tilde{J}(2z_0\Delta\omega/V, d\Delta\omega/V, \omega_s/\omega_W), \quad (8)$$

$$\tilde{J}(a, b, c) = a^4\int_1^{\kappa/b}\frac{t^2 A(bt)\exp(-at)}{(t^2-1)^{0.5}[\exp(cx(bt)) - 1]}dt, \quad (9)$$

where κ is a numerical factor on the order of unity ($\kappa > b$) corresponding the maximum possible wavenumber ($k_m = \kappa/d$) on the dispersion branch of surface excitations. This point corresponds to branching of the dispersion dependence, whereby it separates into the high- and low-frequency modes. The results of numerical calculations showed that the function $\tilde{J}(a, b, c)$, where $a = 2z_0\Delta\omega/V$, is characterized by a maximum at $a = 3$–4. The exact position of this maximum also depends on the variable $b = d\Delta\omega/V$ (the upper limit of b does not exceed κ). The function $\tilde{J}(a, b, c)$ also exhibits a maximum with respect to the variable b (this maximum is attained for $b/a \approx 1.5$–2) and exponentially decays with increasing variable c (see formula (9)). It can be shown that, in the limit of negligibly weak damping (whereby $\gamma \longrightarrow 0$ or $\tau \longrightarrow \infty$ in formulas (2a) and (2b), respectively), only the high-frequency surface mode is retained. In the case of finite damping, an increase in γ leads to a shift of the branching point of the dispersion

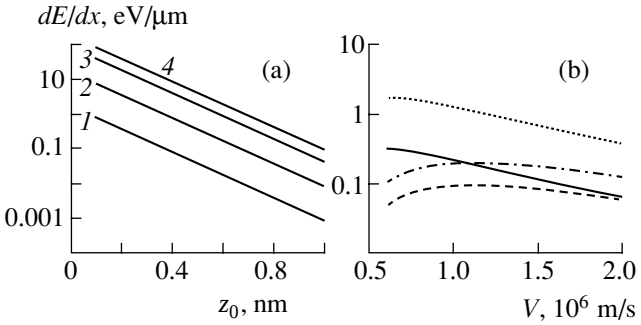

Fig. 1. Drag losses for cesium atoms moving over a MgO film on a metal substrate: (a) versus distance z from the surface at T = 177 (*1*), 300 (*2*), 600 (*3*), and 900 K (*4*) for $V = 0.6 \times 10^6$ m/s (d = 0.39 nm); (b) versus atomic velocity V for z_0 = 0.5 nm, T = 300 K (solid curve), z_0 = 0.5 nm, T = 600 K (dotted curve), z_0 = 1.0 nm, T = 600 K (dashed curve), and z_0 = 1.0 nm, T = 900 K (dash–dot curve) (d = 0.45 nm).

dependence toward smaller wavevectors, which results in some decrease in the values of κ and the integral (9).

As can be seen from expressions (5) and (8), the drag increases for atoms with low values of the transition frequency ω_{0n}. For this reason, it was expedient to obtain quantitative estimates for a beam of cesium atoms characterized by a doublet at 1.39 and 1.46 eV [8]. The results of calculations of the energy losses of cesium atoms moving at a distance of 0.5 nm from the surface of various typical materials bearing IR surface modes are presented in the table. The calculations were performed using formula (5) for the "bulk" materials and formula (8) for the films, with allowance for both branches of the dispersion dependence. The velocity V and the film thickness were optimized (at a preset distance z_0) so as to obtain the maximum possible drag losses. The case of "bulk" materials corresponds to $d = \infty$. The values of transition frequencies and oscillator strengths for Cs atoms were taken from the reference literature [8], while the parameters of dielectric functions (2a) and (2b) were taken from published data indicated as in the table. With the same optimum values of z_0/V and d/V, the data in the table can be readily recalculated for some other distance from the surface using the relation $dE/dx \sim z_0^{-4}$. It should be noted that the interval of atomic velocities indicated in the table corresponds to the energies of Cs atoms from 210 to 370 keV.

As can be seen from data in the table, the energy losses for the films are higher by a factor of about two than those for the same "pure" bulk materials. As noted above, this is related to the appearance of two surface optical modes with approximately equal contributions to the result. In addition, the drag dE/dx significantly increases with the surface temperature. To within an acceptable error (10–20%), the drag can be evaluated by using formula (5) and then doubling the result. However, it should be taken into account that the obtained estimate corresponds to the optimum film thickness ($d = 0.6$–$0.8z_0$). For other thicknesses, the drag will be less pronounced. The results of numerical calculations of dE/dx as a function of the distance from the surface and the velocity of particles moving along a MgO film (for which the expected drag losses are maximum in comparison to all other film materials studied) are presented in Figs. 1a and 1b, respectively.

Despite a rather small magnitude of the drag losses, their experimental observation is quite a real task. A beam of neutral cesium atoms with energies within 200–400 keV can be obtained by means of neutralization of the corresponding ion beam. A more thorough consideration of the experimental conditions, involving

Results of calculations of the resonance drag losses dE/dx for cesium atoms moving at the surfaces of various (a) bulk solids and (b) films

Material		ε_0	ε_∞	ω_T, ω_P, eV	V, 10^6 m/s	d, nm	T, K 177	dE/dx, eV/μm		
								300	600	900
SiC	*a*	9.8	6.7	0.098	0.64	∞	6×10^{-4}	0.013	0.14	0.34
	b				0.66	0.3	0.001	0.026	0.27	0.66
MgO	*a*	9.8	2.95	0.049	0.56	∞	0.017	0.16	0.77	1.87
	b				0.59	0.39	0.033	0.307	1.78	3.68
GaAs	*a*		9.8	0.033	0.73	∞	0.09	0.27	0.77	1.3
	b				0.73	0.32	0.18	0.52	1.47	2.51
Doped Si	*a*		11.7	0.098	0.62	∞	0.005	0.063	0.42	0.9
	b				0.62	0.38	0.008	0.11	0.77	1.68

Note: All dE/dx values were calculated for z_0 = 0.5 nm, and the values of the permittivity components were taken from published data for SiC [9], MgO [10], GaAs [11], doped silicon [12]; γ for SiC ($\gamma/\omega_T = 0.006$) corresponds to [9]; in all other cases, $\gamma/\omega_T = 0.01$.

an analysis of the atomic trajectories near the solid surface, was presented in [6].

REFERENCES

1. G. V. Dedkov, Nucl. Instrum. Methods Phys. Res. B **143**, 584 (1998).
2. G. V. Dedkov, Surf. Coat. Technol. **158–159**, 75 (2002).
3. G. V. Dedkov and A. A. Kyasov, Fiz. Tverd. Tela (St. Petersburg) **44**, 1729 (2002) [Phys. Solid State **44**, 1809 (2002)].
4. G. V. Dedkov and A. A. Kyasov, Phys. Low-Dimens. Semicond. Struct. **1–2**, 1 (2003).
5. G. V. Dedkov and A. A. Kyasov, Fiz. Tverd. Tela (St. Petersburg) **45**, 1729 (2003) [Phys. Solid State **45**, 1815 (2003)].
6. G. V. Dedkov and A. A. Kyasov, Nucl. Instrum. Methods Phys. Res. B **183**, 241 (2001).
7. G. V. Dedkov and A. A. Kyasov, Pis'ma Zh. Tekh. Fiz. **30** (13), 65 (2004) [Tech. Phys. Lett. **30**, 560 (2004)].
8. A. A. Radtsig and B. M. Smirnov, *Reference Data on Atoms, Molecules, and Ions* (Atomizdat, Moscow, 1980; Springer-Verlag, Berlin, 1985).
9. *Handbook of Optical Constants of Solids*, Ed. by E. D. Palik (Academic, New York, 1985).
10. P. M. Echenique and A. Howie, Ultramicroscopy **16**, 269 (1985).
11. J. S. Nkoma, Phys. Status Solidi B **139**, 117 (1987).
12. M. Auslender and M. S. Hava, Infrared Phys. Technol. **36**, 1077 (1995).

Translated by P. Pozdeev

Technical Physics Letters, Vol. 31, No. 4, 2005, pp. 302–305. Translated from Pis'ma v Zhurnal Tekhnicheskoĭ Fiziki, Vol. 31, No. 7, 2005, pp. 70–77.

Noise-Induced Coherence in an Excitable System with Frequency-Dependent Feedback

D. V. Setsinsky and D. É. Postnov

Saratov State University, Saratov, Russia

Received October 12, 2004

Abstract—The influence of the properties of an excitable system on the characteristics of the coherence resonance effect have been studied by experimental and numerical methods. The transition from monostable to bistable regime is accompanied by the appearance of a false maximum in the regularity parameter of the power spectrum plotted as a function of the noise intensity. An increase in the dimensionality of the system activates a mechanism whereby the noise reveals oscillatory dynamics, also resulting in the appearance of an additional maximum in the regularity parameter. *© 2005 Pleiades Publishing, Inc.*

Introduction. In recent years, it has become clear that the phenomenon of noise-induced coherence in excitable systems (the coherence resonance effect) has a general character and is frequently encountered in adjacent fields of science. In particular, manifestations of this effect in neuron dynamics provide for a new outlook on the problem of the functioning of an ensemble of neurons in the presence of noise. In the initial stage of research, the most general laws of this phenomenon were studied via theoretical analysis of the simplest models of excitable systems [1–3], including their piecewise linear approximations [4]. By now, the main mechanisms of the coherence resonance effect have been established and the laws of behavior of such excitable systems in ensembles have been studied [5–7]. However, a number of questions related to the dependence of this effect on the properties of an excitable system are still insufficiently clear.

As is known, an excitable system is characterized by the presence of a pseudo-orbit representing an almost closed trajectory [8]. A comparative analysis of several models belonging to the class of excitable systems shows that the number of segments of such a pseudo-orbit may exceed one if the system under consideration has several sequentially attained stable states (i.e., exhibits multistability). Some results indicate that noise-induced coherence also takes place in such cases, but the characteristics of this effect (in particular, the shape of the Fourier spectrum of the power of noise-induced oscillations) are significantly different from those in a monostable case [4].

Now, it is also clear that the dimensionality of the pseudo-orbit embedding space is another important factor. In particular, it was demonstrated [4] that the noise-induced coherence arises upon the passage from one- to two-dimensional model of an overdamped bistable oscillator. In another limiting case [9], it was shown that coherence resonance is possible in a bistable system with delayed feedback, which corresponds to an infinite dimensionality of the pseudo-orbit embedding space.

This Letter presents the results of radiophysical and numerical experiments providing information on the influence of the aforementioned factors on the characteristics of the coherence resonance effect.

Description of the model. We have studied a radiophysical model comprising an inertial nonlinear unit having an N-shaped characteristic, with feedback in the form of a low-pass *RC* filter (Fig. 1a). By selecting a working point on the N-shaped characteristic, it is possible to realize both monostable and bistable regimes (with one or two pseudo-orbit segments, respectively). By varying the number of *RC* units in the feedback chain, it was possible to change the filter order, which corresponded to a change in the dimensionality of the pseudo-orbit embedding space. In the case of a single-unit filter and a monostable regime of the nonlinear element, the equations describing the model system can be reduced to those of a model of the FitzHugh–Nagumo type [10]. For a system with an *N*-unit filter, a mathematical model of the device (Fig. 1a) is described by the following set of equations:

$$\begin{aligned} \dot{x} &= ax - bx^3 - \varepsilon y_N + D\xi(t), \quad \tau\dot{y}_1 = (k(x+c) - c - y_1), \\ &\qquad\qquad \tau\dot{y}_2 = (y_1 - y_2), \\ c &= \sqrt{(a-\varepsilon)/b}, \qquad\qquad \ldots \\ &\qquad\qquad \tau\dot{y}_N = (y_{N-1} - y_N), \end{aligned} \tag{1}$$

where the equation for x refers to the bistable system proper with a potential determined by the parameters a and b (we have studied the case of $a = 2$ and $b = 4$); the equations for y_i ($i = 1, \ldots, N$) describe the feedback

1063-7850/05/3104-0302$26.00 © 2005 Pleiades Publishing, Inc.

chain involving an N-unit low-pass filter (each unit having the time constant $\tau = RC$); ε is the feedback coefficient; D is the intensity of the white noise $\xi(t)$ with a zero mean ($\langle\xi(t)\rangle = 0$). The second equation of the system is written so that, by changing the control parameter k, it is possible to select the case with one or two stable equilibrium states. In the radiophysical model depicted in Fig. 1a, this selection was effected by setting the necessary bias voltage U_{bal} (controlled by potentiometer R_{15}) and the feedback gain (controlled by potentiometer R_{14}).

In order to qualitatively assess the degree of regularity and the regime of the noise-induced oscillations, we have calculated the degree of inhomogeneity of the spectrum of the signal power spectrum [11, 12]. This method has proved to work well with the spectra of any shape, including those with several maxima, and was successfully used in the investigations of stochastic dynamics in the ensembles of excitable systems [6, 7]. At the same time, the absolute value of the degree of regularity β depends on the parameters of the scheme of numerical calculations of the Fourier spectrum (e.g., on the number of readings). For this reason, these parameters remained unchanged and were the same during the processing of data from both numerical and radiophysical experiments. The obtained β values fall within the interval between 0 (white noise) and 1 (harmonic oscillations).

Results and discussion. The results of our investigation of the noise-induced dynamics of the model system in monostable and bistable regimes showed that, in both cases, low values of the regularity parameter β correspond to small and high noise intensities D. Intermediate D values correspond to the generation of a relatively regular sequence of pulses of approximately equal duration and, accordingly, to large β values reflecting the presence of the coherence resonance effect.

Figures 1b and 1c show the typical spectra of noise-induced oscillations in the bistable and monostable regimes, respectively. According to the results of both numerical and radiophysical experiments, the plot of β versus D for the monostable regime exhibits a clearly pronounced single maximum (Fig. 2a). The curve obtained for the bistable regime (Fig. 2b) has a more complicated shape, with an additional maximum in the region of a low noise intensity ($D \approx 0.05$) observed in both numerical (curve *1*) and radiophysical (curve *3*) experiments. The results of our investigation showed that the additional maximum is related to special features in the behavior of a system with two stable equilibrium states.

In the simplest case, an excitable system has a single stable equilibrium state, in which the system occurs in a nonexcited state and to which it returns upon generation of a pulse in response to external excitation. According to [2], the mechanism of the coherence resonance effect in this case is based on the balance of two characteristic times. One of these times is related to activation of the system from a stable equilibrium state and depends on the acting noise intensity (determining the time to attaining the threshold). The second characteristic time corresponds to the duration of motion over the pseudo-orbit and is determined by the intrinsic properties of the system rather than by the noise intensity. The system response is a random sequence of pulses with a fixed duration.

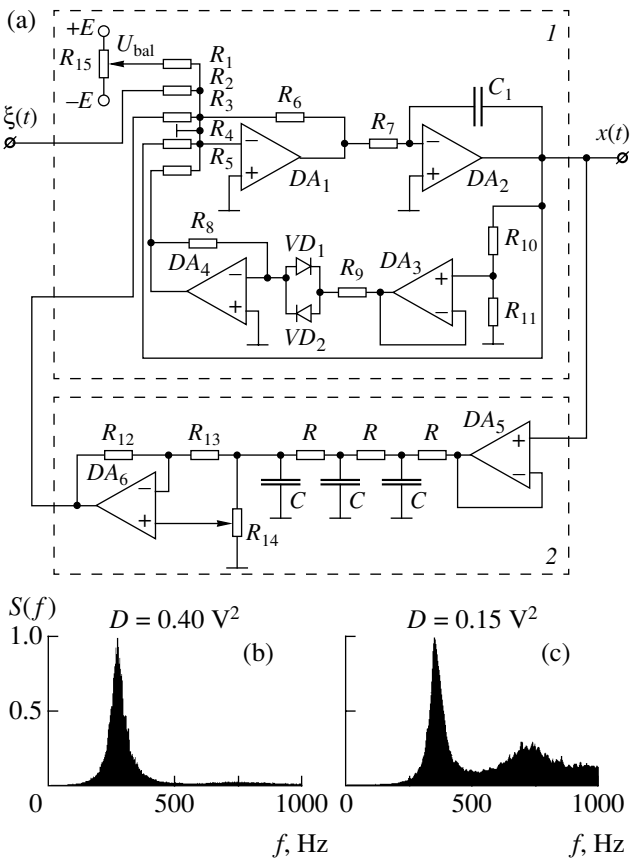

Fig. 1. (a) Schematic circuit diagram of the experimental setup ($R_1 = R_{12} = 100$ kΩ; $R_2 = R_3 = R_6 = R_9 = R_{10} = R_{13} = 10$ kΩ; $R_4 = 150$ kΩ; $R_5 = 2.2$ kΩ; $R_7 = 5.1$ kΩ; $R_8 = 57$ kΩ; $R_{11} = 0.68$ kΩ; $R_{14} = R_{15} = 20$ kΩ; $C_1 = 150$ pF; $R = 7.5$ kΩ; $C = 0.1$ μF; (b, c) typical normalized power spectra of noise-induced oscillations in the bistable and monostable regimes, respectively.

In the case of two equilibrium states, the system cannot immediately and directly return back to the state in which it occurred before activation. Instead, the system first jumps to another equilibrium state, and only from that state can it return back. Thus, the pseudo-orbit in this case consists of two segments, which are sequentially passed one after another. At low noise intensity, the system exhibits rare random jumps from one to another equilibrium state and spends time predominantly in one of these states. As a result, for any finite observation time, there is an interval of D values

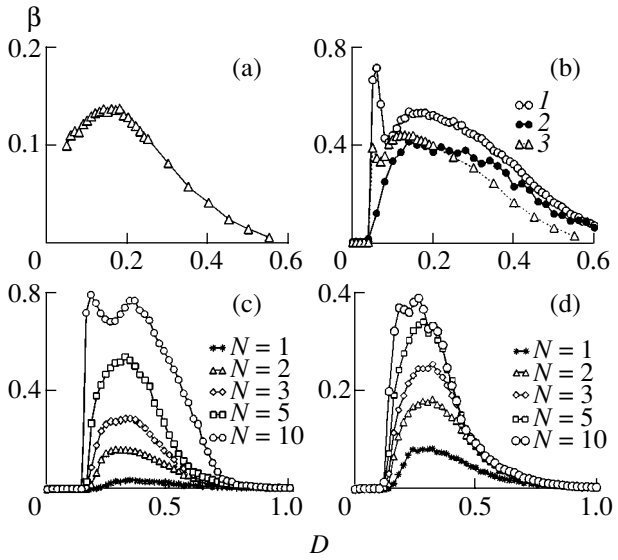

Fig. 2. Plots of the degree of regularity of the noise-induced oscillations in the (a, c) bistable and (b, d) monostable regimes, respectively: (a, b) $N = 1$. Curves *1* and *3* exhibit a false regularity maximum (see the text for explanation); (c, d) curves refer to various numbers of *RC* units in the feedback chain. The curve in (a) and curve *3* (b) were obtained in the radiophysical experiment; all other curves were obtained by numerical modeling using Eqs. (1).

in which the signal has a significant constant component. The Fourier spectrum of such a signals exhibits a pronounced peak at a zero frequency, which accounts for the appearance of an additional false maximum in the regularity parameter. Since the degree of manifestation of this effect depends on how the equilibrium states are "projected" onto the response signal of the system under consideration, this maximum can be eliminated by properly selecting the time series. For example, curve *2* in Fig. 2b was calculated using a time series representing the deviation of the state of system (1) on the phase plane (x, y_1) from a straight line defined by the zero isocline equation $\dot{y} = 0$. The passage to this frame of reference leads to the loss of all information about the particular equilibrium state in which the system occurs. As can be seen, the β versus D curve in this case exhibits only the main peak of regularity, while the false peak in the region of low noise is absent.

In the course of investigation of the stochastic dynamics of a system with increasing dimensionality, we have calculated the degree of regularity β of the response of system (1) with one ($k = 4$) and two ($k = 1$) equilibrium states for various numbers of equations (various numbers of *RC* units in the low-pass filter) describing the feedback chain. In the bistable regime, the degree of regularity was calculated for the magnitude of deviation from the zero isocline $\dot{y} = 0$.

The results of numerical modeling showed that, for a relatively small number of *RC* units ($N = 1$, 2, 3, and 5), the β versus D curve has a single maximum (Figs. 2c and 2d). However, an increase in the number of units to $N = 10$ and above leads to the appearance of an additional maximum in the regularity in the region of low D values. In this case, in contrast to the false regularity peak considered above, the additional maximum reflects real ordering of the noise-induced oscillations. As the number of equations (or the number of filter units) increases, the properties of the feedback chain approach, to a certain extent, the properties of a delay line with a fixed time $T = N\tau$. As is known from the theory of radio circuits, this gives rise to autooscillations with a frequency multiple of $1/T$, provided that the gain ε of the feedback chain is sufficiently high. If the ε value is insufficiently large, the system is underexcited but, nevertheless, the noise action reveals an autooscillatory dynamics [1, 14]. A maximum in the regularity of oscillations is observed when the average time of the noise activation of an excitable system coincides with the delay time ($D \approx 2$ in Figs. 2c and 2d). From this standpoint, our results are equivalent to a "finite-dimensionality" approximation [9], where noise-induced coherence was found for the first time in a delayed feedback bistable system.

Conclusions. The results of our numerical and radiophysical experiments showed that an excitable system may exhibit the coherence resonance effect in both monostable and bistable regimes, but the presence of two equilibrium states has to be taken into account in the calculation of the quantitative characteristics of regularity. An increase in the dimensionality of the system leads to the manifestation of another mechanism of noise-induced coherence. In this case, the plot of the degree of regularity exhibits two maxima corresponding to different noise intensities. The above results are of importance for the development of clearer notions about various aspects of the noise-induced coherence and more adequate interpretation of the behavior of stochastic excitable systems entering into ensembles.

Acknowledgments. This study was supported by the Russian Foundation for Basic Research (project no. 04-02-16769), the INTAS Foundation (grant no. 01-2061), and the US Civilian Research and Development Foundation (CRDF) for the Independent States of the Former Soviet Union (CRDF Award no. REC-006).

REFERENCES

1. A. Neiman, P. Saparin, and L. Stone, Phys. Rev. E **56**, 270 (1997).
2. A. Pikovsky and J. Kurths, Phys. Rev. Lett. **78**, 775 (1997).
3. D. E. Postnov, S. K. Han, T. G. Yim, and O. V. Sosnovtseva, Phys. Rev. E **59**, R3791 (1999).
4. B. Lindner and L. Schimansky-Geier, Phys. Rev. E **61**, 6103 (2000).

5. O. V. Sosnovtseva, A. I. Fomin, D. E. Postnov, and V. S. Anishchenko, Phys. Rev. E **64**, 026204 (2001).
6. D. E. Postnov, O. V. Sosnovtseva, S. K. Han, and W. S. Kim, Phys. Rev. E **66**, 016203 (2002).
7. D. E. Postnov, O. V. Sosnovtseva, and D. V. Setsinsky, Fluct. Noise Lett. **3**, L275 (2003).
8. E. M. Izhikevich, Int. J. Bifurcat. Chaos Appl. Sci. Eng. **10**, 1171 (2000).
9. L. S. Tsimring and A. Pikovsky, Phys. Rev. Lett. **87**, 250602 (2001).
10. R. A. Fitzhugh, Biophys. J. **1**, 445 (1961); A. C. Scott, Rev. Mod. Phys. **47**, 487 (1975).
11. S. K. Han, T. G. Yim, D. E. Postnov, and O. V. Sosnovtseva, Phys. Rev. Lett. **83**, 1771 (1999).
12. D. E. Postnov, D. V. Setsinskiy, and O. V. Sosnovtseva, Pis'ma Zh. Tekh. Fiz. **27** (11), 49 (2001) [Tech. Phys. Lett. **27**, 463 (2001)].
13. I. S. Gonorovskiĭ, *Radio Circuits and Signals* (Nauka, Moscow, 1986) [in Russian].
14. S.-G. Lee, A. Neiman, and S. Kim, Phys. Rev. E **57**, 3292 (1998).

Translated by P. Pozdeev

Technical Physics Letters, Vol. 31, No. 4, 2005, pp. 306–308. Translated from Pis'ma v Zhurnal Tekhnicheskoĭ Fiziki, Vol. 31, No. 7, 2005, pp. 78–84.

Monitoring Water Content in the Course of Microwave Heating

A. V. Markov and Yu. P. Yulenets*

St. Petersburg State Technical University, St. Petersburg, 195251 Russia

** e-mail: julenez@yandex.ru*

Received July 7, 2004

Abstract—A method of monitoring the water content of homogeneous (single-layer) and composite (two-layer) materials in the course of microwave heating is described. According to this, microwave heating is performed for a short period of time, after which the temperature is measured in each layer and the water content is calculated using relations established with allowance for the attenuation of the incident electromagnetic wave power. © *2005 Pleiades Publishing, Inc.*

Microwave thermal treatment is the most effective means of fighting harmful flora and fauna (fungi, insects, termites, etc.) occurring in some structural materials, since it is possible to heat both the surface and deeper layers of the structure. In practice, this treatment is performed using microwave beam sources of the open cavity type [1, 2]. In order to select an optimum thermal treatment regime, it is necessary to know, among other parameters, the initial water content in the target material. Methods for determining the water content in homogeneous materials are well known [3–5]. At the same time, no methods are available for monitoring the water content in inhomogeneous (in particular, double-layer) materials, especially in cases of practically unlimited volume (walls, floors, etc.). However, knowledge of the laws of microwave heating provides a relatively simple approach to indirect monitoring of the water content in processed materials.

Consider a microwave radiator of the horn type emitting a plane electromagnetic wave from the known effective area. With neglect of the drying action, equations describing the temperature field in a two-layer material irradiated by such a flat electromagnetic wave normally incident onto the half-space $x > 0$ are as follows:

$$\frac{\partial T_1}{\partial \tau} = a_{T1}\frac{\partial^2 T_1}{\partial x^2} + \frac{p_1(x, W_1)}{c_1\rho_1}, \quad (1)$$

$$\frac{\partial T_2}{\partial \tau} = a_{T2}\frac{\partial^2 T_2}{\partial x^2} + \frac{p_2(x, W_1, W_2)}{c_2\rho_2}. \quad (2)$$

Here, T_1 and T_2 are the local temperatures of the first (outer) and second (inner) layers, respectively; x is the coordinate; a_{T1} and a_{T2} are the thermal diffusivities of the corresponding layers; c_1, ρ_1 and c_2, ρ_2 are the heat capacities and densities of the layers; p_1 and p_2 are the specific microwave radiation powers deposited in each layer; W_1 and W_2 are the water contents in the layers; and τ is the current time.

The boundary conditions for the problem described by Eqs. (1) and (2) can be written as

$$T_1 = T_2 = T_0 \quad \text{at} \quad \tau = 0, \quad (3)$$

$$\lambda_1\frac{\partial T_1}{\partial x}\bigg|_{x=\sigma_1} = \lambda_2\frac{\partial T_2}{\partial x}\bigg|_{x=\sigma_1}, \quad (4)$$

$$T_1|_{x=\sigma_1} = T_2|_{x=\sigma_1}, \quad (5)$$

$$\lambda_1\frac{\partial T_1}{\partial x}\bigg|_{x=0} = k_0(T_1|_{x=0} - T_{sur}), \quad (6)$$

where σ_1 is the thickness of the first (outer) layer, λ_1 and λ_2 are the thermal conductivity coefficients, k_0 is the heat exchange coefficient, and T_{sur} is the temperature of surrounding medium.

The powers deposited in each layer are described by the equations [6–8]

$$p_1(x, W_1) = 2\alpha_1(W_1)p_{01}[1 - \gamma_1(W_1)]\exp[-2\alpha_1(W_1)x], \quad 0 \le x \le \sigma_1, \quad (7)$$

$$p_2(x, W_1, W_2) = 2\alpha_2(W_2)p_{02}\exp[-2\alpha_2(W_2)(x - \sigma_1)], \quad x > \sigma_1, \quad (8)$$

where α_1 and α_2 are the coefficients of electromagnetic wave damping in the corresponding layers, γ_1 is the coefficient of wave reflection from the first layer, and p_{01} and p_{02} are the microwave radiation power densities incident on the corresponding layers. The power inci-

dent on the second (inner) layer can be calculated using the formula

$$p_{02} = p_{01}[1-\gamma_1(W_1)]\exp[-2\alpha_1(W_1)\sigma_1]. \quad (9)$$

In the case of high-rate microwave heating for a short period of time, we may ignore the heat transfer inside the target by means of thermal conductivity $\partial T/\partial\tau \gg a_T(\partial^2 T/\partial x^2)$. Then, the rates of heat evolution will depend only on the damping and reflection coefficients (which are functions of the water content), and system of equations (1)–(4) can be solved analytically, which yields

$$T_{K1}(W_1, x, \tau_{rad}) = T_0 + \frac{2\alpha_1(W_1)p_{01}[1-\gamma_1(W_1)]\tau_{rad}}{c_1\rho_1} \times \exp[-2\alpha_1(W_1)x], \quad (10)$$

$$T_{K2}(W_2, x, \tau_{rad}) = T_0 + \frac{2\alpha_2(W_2)p_{02}[1-\gamma_2(W_1)]\tau_{rad}}{c_2\rho_2} \times \exp[-2\alpha_2(W_2)(x-\sigma_1)]. \quad (11)$$

Using relations (10) and (11) and the known physical characteristics ($\alpha(W)$ and $\gamma(W)$ functions) of the materials in both layers, it is possible to determine the final (reached for the fixed time $\tau = \tau_{rad}$ of the microwave treatment) values of the temperatures T_{K1} and T_{K2}, which will depend on the water content in each layer. Thus, the proposed method of monitoring of the water content consists in microwave heating (irradiation) of a two-layer material for a short period of time τ_{rad}, after which the microwave source is switched off, the temperatures of layers (T_{K1}, T_{K2}) are measured, and the water contents in the layers are calculated using formulas (10) and (11). In order to exclude the error related to a nonuniform radiation pattern of the horn radiator, the T_{K1} and T_{K2} values should be measured at the points on the radiator symmetry axis. The results of application of the proposed method are illustrated by the data presented in Figs. 1 and 2.

As can be seen, the results of $W_1(T_{K1})$ and $W_2(T_{K2})$ determination at large depths are rather ambiguous. Indeed, an increase in the water content leads to a growth of the damping coefficient and a drop in the radiation power delivered to the bulk of material. Initially (at a low water content), the growth of the damping coefficient prevails and the material temperature increases throughout the layer. However, at a higher water content, the effect of attenuation of the microwave radiation power supplied to a given depth becomes more pronounced. Since a considerable part of the incident power is absorbed in the surface layers, the rate of heating of the deeper layer decreases (Fig. 1, curves *4* and *5*; Fig. 2, curve *5*). Taking into account the well-known difficulties encountered in the determination of the heat-exchange coefficient, it is generally recommended to perform the temperature measurements within the framework of the proposed method at small distances from the surface of each layer.

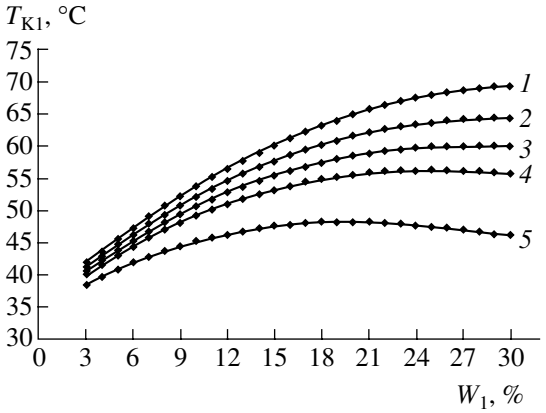

Fig. 1. The results of rapid determination of the water content W_1 using the results of measurements of the temperature T_{K1} reached in the first layer of a two-layer structure (gypsum plaster on brick wall) during microwave heating at $T_0 = 20°C$, $\tau_{rad} = 60$ s, $p_{01} = 70.4$ kW/m^2 (incident power density at the point on the material surface on the horn radiator axis). The curves refer to various depths $x = 0$ (*1*), 5 (*2*), 10 (*3*), 15 (*4*), and 30 mm (*5*); the water content is calculated per unit weight of absolutely dry material.

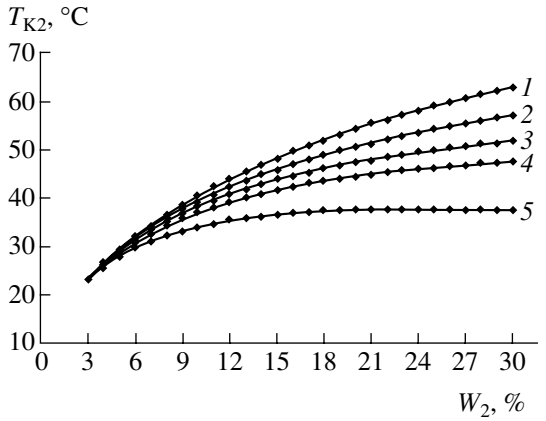

Fig. 2. The results of rapid determination of the water content W_2 using the results of measurements of the temperature T_{K2} reached in the second layer of a two-layer structure (gypsum plaster with $W = 10\%$ and a thickness of $\sigma_1 = 35$ mm on brick wall) during microwave heating at $T_0 = 20°C$, $\tau_{rad} = 60$ s, $p_{01} = 70.4$ kW/m^2 (incident power density at the point on the material surface on the horn radiator axis). The curves refer to various depths $x = 35$ (*1*), 40 (*2*), 45 (*3*), 50 (*4*), and 65 mm (*5*); the water content is calculated per unit weight of absolutely dry material.

In order to select the irradiation time (τ_{rad}), let us use the adiabatic approximation condition, whereby the heat transfer via thermal conductivity can be ignored. This

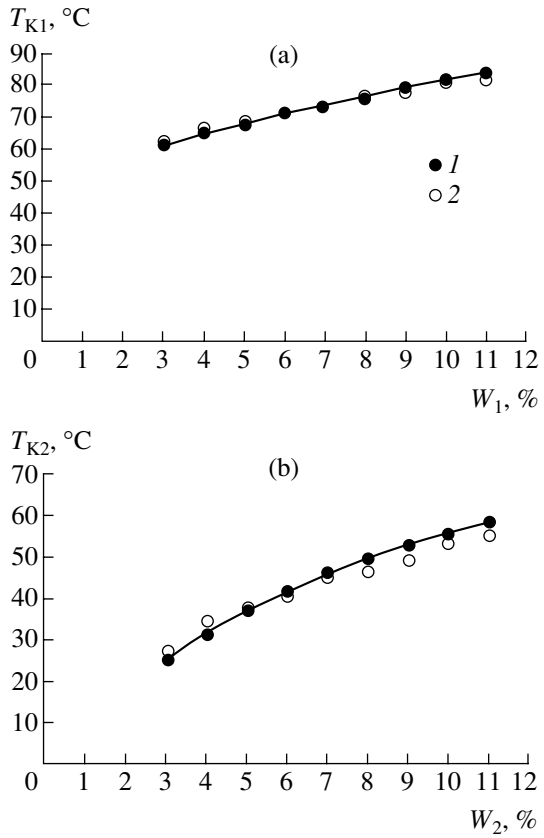

Fig. 3. The results of rapid determination of the water content using (*1*) the proposed method of microwave heating (p_{01} = 70.4 kW/m^2; τ_{rad} = 120 s) and (2) the direct measurements in a two-layer structure (gypsum plaster with W = 10% and a thickness of σ_1 = 35 mm on brick wall; T_0 = 20°C): (a) water content W_1 in the plaster at x = 10 mm; (b) water content W_2 in the brick wall at x = 45 mm.

approximation is applicable provided that $\partial T/\partial\tau \gg a_T(\partial^2 T/\partial x^2)$, or [6]

$$\tau_{rad} \ll \frac{1}{4\alpha^2 a_T}. \quad (12)$$

Note that this condition does not involve the incident power. The contribution of a term responsible for the thermal conductivity will not exceed 5% when

$$\tau_{rad} < \tau_{max} = \frac{0.05}{4\alpha^2 a_T}. \quad (13)$$

For example, the maximum irradiation time for a brick wall with a water content of W = 15% is τ_{max} = 124 s. The lower the water content, the higher the τ_{max} value. However, large irradiation times may introduce additional errors into the results of measurements because the temperature of the material surface may be close to 100°C. Indeed, for a standard microwave heating regime (p_{01} = 70.4 kW/m^2 for P = 0.75 kW at f = 2450 MHz), the surface temperature of a gypsum plaster with a water content of W = 15% reaches 100°C for τ_{rad} = 120 s. This example also shows that the irradiation time should not be selected large for materials with high initial water contents.

On the other hand, an excessively short irradiation time leads to weak heating, so that the difference in the temperatures of materials with different water contents will be rather insignificant. For example, in a two-layer system of gypsum plaster with W = 10% on a brick wall, irradiation at the same level of incident power (p_{01} = 70.4 kW/m^2) for τ_{rad} = 20 s leads to a temperature difference as small as 0.5 K at points in the second layer (brick wall) at a depth of 10 mm with the water content differing by 1%.

The results of our evaluations showed that, in practical implementation of the proposed method, the parameter τ_{rad} can be selected using a simple relation:

$$\tau_{rad} = 0.8\text{–}0.9\tau_{max}. \quad (14)$$

Figure 3 presents data on the water content in a two-layer structure determined by the method described above, in comparison to the results of direct measurements. The relative mean square error of the proposed method does not exceed 6.5%.

REFERENCES

1. *Microwave Power Engineering*, Ed. by E. C. Okress (Academic, New York, 1968; Mir, Moscow, 1971), Vol. 2.
2. Yu. S. Arkhangel'skiĭ, *Microwave Electrometry* (Saratov State Technical University, Saratov, 1998) [in Russian].
3. M. A. Berliner, *Humidity Measurements* (Énergiya, Moscow, 1973) [in Russian].
4. R. A. Berentsveig and V. V. Shevchenko, Inzh.-Fiz. Zh. **14**, 1079 (1968).
5. I. I. Devyatkin *et al.*, USSR Inventor's Certificate No. 324567 (1972) Byull. Izobret., No. 2 (1972).
6. L. E. Rikenglaz, Inzh.-Fiz. Zh. **27**, 1061 (1971).
7. A. H. Didenko and B. V. Zverev, *Microwave Power Engineering* (Nauka, Moscow, 2000) [in Russian].
8. A. V. Markov and A. V. Bubnov, in *Proceedings of the 16th International Conference on Mathematical Methods in Engineering and Technologies, St. Petersburg, 2003*, Vol. 10, pp. 83–84.

Translated by P. Pozdeev

Technical Physics Letters, Vol. 31, No. 4, 2005, pp. 309–311. Translated from Pis'ma v Zhurnal Tekhnicheskoĭ Fiziki, Vol. 31, No. 7, 2005, pp. 85–90.

Tribospectroscopic Study of a Steel–Steel Friction Couple

V. L. Popov and Ya. Starchevich

Berlin Technical University, Berlin, Germany

Received November 22, 2004

Abstract—The force of friction between a steel plate and a steel sample oscillating at a frequency of 60–70 kHz has been studied as a function of the oscillation amplitude. The static friction force rapidly decays when the oscillation amplitude increases from zero to 0.1 μm. Then, the force decreases only slightly as the amplitude grows further up to about 0.5 μm. The experimental data are interpreted within the framework of a theoretical model comprising two bodies moving in a random potential and coupled by a randomly oscillating bond. An analysis of this model shows that the oscillation amplitude at which the behavior of the friction force exhibits a qualitative change corresponds to a spatial scale producing a maximum contribution to the frictional force. From this, it is concluded that friction in the steel–steel couple originates on a scale of about 50 nm.

Introduction. In order to formulate adequate models of the friction and wear processes, it is necessary to know the characteristic scale of phenomena responsible for the formation of friction forces in a given system. Determining this scale is frequently a nontrivial problem, because (i) processes in the friction zone are inaccessible to direct experimental observation and (ii) the macroscopic force of friction is insensitive to the spatial scale on which the friction arises.[1] Therefore, reconstruction of the microscopic interaction potential from the macroscopic friction force is impossible. Despite extensive development of the physics of friction in the past two decades, the characteristic spatial scale producing the maximum contribution to the friction is still unknown for most materials of interest from the standpoint of practical tribology.

Previously, it was theoretically demonstrated [2–4] that the microscopic interaction potential responsible for the friction force formation can be reconstructed from the known behavior of the static friction force in a couple where one of the bodies performs high-frequency oscillations. The static friction force in the presence of such oscillations depends on the oscillation amplitude. At a given amplitude, the friction force provides information about the interaction potential component with a wavelength on the order of this amplitude. Thus, by measuring the static friction force as a function of the oscillation amplitude, we can obtain information about the entire spectrum of the interaction potential in a wavelength range corresponding to the interval of variation of the amplitude of oscillations of the body performing high-frequency oscillations. This idea underlies the method of tribospectroscopic investigation of the friction surfaces.

This paper reports the results of our experimental study of the force of friction in a steel–steel couple as a function of the oscillation amplitude. These results are compared to theoretical predictions so as to investigate the spatial scale responsible for the main contribution to the friction force in the couple studied.

Experimental setup and results. The main measuring element in our experimental system is a sample whose ends are in contact with the base plate (Fig. 1). Using piezoelements incorporated in the middle part of the sample, it was possible to change the sample length by applying an ac voltage with a frequency of 60–70 kHz. Since the exact frequency corresponded to the intrinsic resonance, the oscillation amplitude could reach about 1 μm. The frequency was automatically tuned in resonance with the aid of a special controller. The amplitude of sample oscillations $\Delta l/2$ on one of the ends was measured using a laser vibrometer employing the Doppler effect (data readout frequency, 1 MHz). The total amplitude (Δl) was assumed to be twice as large as the value measured at the end. The sample was moved along the base plate with the aid of a soft spring. In order to eliminate jumps upon reaching the critical

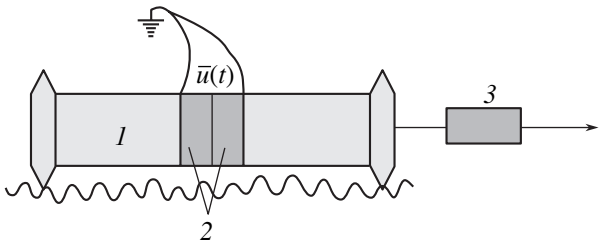

Fig. 1. Schematic diagram of the measuring sample on a base plate: (*1*) vibrator; (*2*) piezoelements; (*3*) force sensor.

[1] This statement can be illustrated using the Tomlinson model [1], in which the macroscopic force of friction in the limit of strong damping turns out to be independent of the period of the interaction potential responsible for the appearance of friction.

1063-7850/05/3104-0309$26.00 © 2005 Pleiades Publishing, Inc.

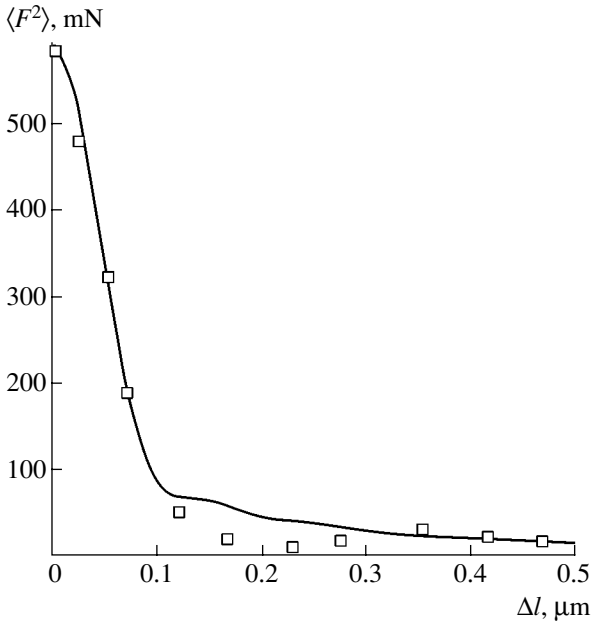

Fig. 2. A plot of the mean square of the friction force $\langle F^2 \rangle$ versus oscillation amplitude Δl. Symbols represent the experimental data; the solid curve shows the results of model theoretical calculations based on Eqs. (3) and (4) with $k_0 = 21\ \mu m^{-1}$.

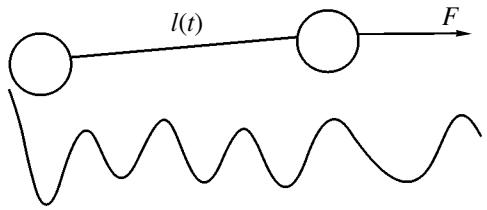

Fig. 3. A model system of two bodies coupled by an oscillating bond of variable length $l(t)$ moving under the action of force F in a random potential.

static friction force, the spring was provided with a damping element.

Each experiment consisted in moving the sample over a distance of about 10 cm while monitoring the spring tension as a function of time. The measured force varied with the time in a random manner. Using these data, the mean square friction force $\langle F^2 \rangle$ was calculated over the entire duration of each experiment in the same way as in the theoretical analysis (see below). The results were averaged over five experiments performed for the same oscillation amplitude. It should be noted that, for the random force, the mean square value amounts to 0.5 of the average static friction force determined as a limiting friction force at low sliding velocities. Thus, the experimentally measured value is directly related to the static friction force acting on the oscillating sample. The average sliding velocity (i.e., the velocity of motion of the sample) was selected to be sufficiently small (typically within 0.25–0.5 mm/s) so as to eliminate the influence on the friction force. This velocity was always much smaller than the velocity of oscillations (7–250 mm/s).

Figure 2 shows a typical experimental curve of the mean square friction force $\langle F^2 \rangle$ versus oscillation amplitude Δl. As can be seen, the static friction force rapidly decays when the oscillation amplitude increases from zero to 0.1 μm. Then, the $\langle F^2 \rangle$ value decreases only slightly as the amplitude grows further to about 0.5 μm.

Theory and its comparison to experiment. the experimental results are interpreted within the framework of a model described previously [2]. Let us briefly outline this model (Fig. 3). We consider two point masses coupled by a rapidly oscillating bond of length

$$l = l_0 + \Delta l \sin(\omega t) \quad (1)$$

and moving in the presence of a constant external force F in a random potential $U = U(x)$ defined by the spectral expansion

$$U(x) = \int_0^\infty c(k)\cos(kx + \varphi_k)dk, \quad (2)$$

where φ_k are the random phases that are assumed to be uncorrelated.

For the mean square "macroscopic" force (averaged over a time interval significantly greater than the sample oscillation period), this yields the expression [2]

$$\langle \overline{F(x)}^2 \rangle = 2\Phi \int_{k_1}^{k_2} c(k)^2 k^2 J_0^2\left(\frac{k\Delta l}{2}\right)dk, \quad (3)$$

where $c(k)^2$ is the spectral density of the interaction potential, $J_0(z)$ is the zero-order Bessel function, and Φ is a constant determining the average square of the force acting in the random potential on each body of the couple. In the simplest case, that of a potential with a single component corresponding to the wavevector k_0, the square of the friction force is proportional to $J_0^2\left(\frac{k_0\Delta l}{2}\right)$. In this case, the friction force vanishes at $\frac{k_0\Delta l}{2} \approx 2.4$ and then increases again.

Now, let us assume that the interaction potential has a continuous spectrum of wavevectors but that the system is characterized by a certain characteristic scale producing the main contribution to the friction force. This implies that the spectral density of the interaction potential has a maximum at a certain value of $k = k_0$. In a system with random interactions, the width of the spectral density function in the space of wavevectors is, generally speaking, on the same order of magnitude as

the characteristic wavevector k_0. One possible model of such spectral density distribution is

$$c(k^2) = \exp\left(-\frac{(k-k_0)^2}{2k_0^2}\right). \quad (4)$$

The mean square friction force calculated for this spectral density using formula (3) and normalized to the friction force at $\Delta l = 0$ is depicted by a solid curve in Fig. 2. The best fit of the experimental data to the theoretical curve is observed for $k_0 = 21\ \mu m^{-1}$. Therefore, the main contribution to the friction force is due to interactions on a spatial scale of $L \sim 1/k_0 \approx 0.05\ \mu m = 50$ nm.

Conclusions. We studied the dependence of the static friction force between a steel plate and a rapidly oscillating steel sample. According to theoretical predictions, the friction force significantly decreases when the oscillation amplitude is on the order of a wavelength corresponding to the spatial scale producing the maximum contribution to the microscopic interaction potential responsible for the friction force. Based on the experimental results, we may conclude that this characteristic scale for a steel–steel couple studied is on the order of 50 nm. The knowledge of this scale is a necessary prerequisite for the development of adequate models of friction and wear.

REFERENCES

1. G. A. Tomlinson, Philos. Mag. **7**, 905 (1929).
2. V. L. Popov and O. K. Dudko, Pis'ma Zh. Tekh. Fiz. **30** (4), 42 (2004) [Tech. Phys. Lett. **30**, 148 (2004)].
3. O. K. Dudko, V. L. Popov, and G. Putzar, Tribol. Schmierungstech. **5**, 23 (2004).
4. O. K. Dudko, V. L. Popov, and G. Putzar, Int. J. Tribol. (2004) (in press).

Translated by P. Pozdeev

Technical Physics Letters, Vol. 31, No. 4, 2005, pp. 312–313. Translated from Pis'ma v Zhurnal Tekhnicheskoĭ Fiziki, Vol. 31, No. 7, 2005, pp. 91–94.

A New Inverse-Pinch Plasma Opening Switch

V. G. Kornilov, S. Yu. Kornilov, D. A. Orlov, V. D. Selemir, D. A. Tolshmyakov, A. A. Khizhnyakov, and V. I. Chelpanov

Institute of Experimental Physics, Russian Federal Nuclear Center, Sarov, Russia

Received November 4, 2004

Abstract—An inverse-pinch plasma opening switch (POS) of a new type has been studied, which is capable of switching a 300–400 kA current at a rise time of ~1 μs and a current fall rate of 8×10^{12} A/s. The POS can operate at both negative and positive polarity of the central electrode. © *2005 Pleiades Publishing, Inc.*

Introduction. In widely used plasma opening switches (POSs), the interelectrode plasma shunt is typically created by injecting plasma from the outer to inner (central) electrode. Recently, Moshella *et al.* [1] suggested a device called the inverse-pinch POS, in which plasma is injected from the central electrode toward an outer one by means of a special source. In this way, it is possible to form an azimuthally uniform plasma layer that favors a better switching performance of the POS.

We have designed and studied a new inverse-pinch POS, in which plasma (also injected from the inner to outer electrode) is generated using a traditional plasma injector.

Setup description. In our setup, the current source comprised a driver, equipped with a capacitive energy storage and a transmission line, with the following characteristics: capacitance, 8 μF; charging voltage, up to 85 kV; inductance of the current circuit (including POS), 175 nH; initial current buildup rate, about 0.5 kA/ns.

Figure 1 shows a schematic diagram of the chamber containing a POS and a plasma channel. The experiments were performed in a cylindrical plasma chamber with an inner diameter of 240 mm and a central electrode diameter of 65 mm. A coaxial gas–plasma injector [2] is situated on the end flange of the chamber. The injector battery is switched on after admitting the plasma-forming gas (air or nitrogen) into the interelectrode space with the aid of a pulsed gas valve. The plasma jet is delivered via a metal tube (plasma guide) inside the central electrode of the POS, where a special forming system converts the plasma flow from axial to radial. The plasma flow enters the interelectrode space via slits or through a grid, forming an azimuthally uniform layer. The interelectrode gap of the POS is bounded by an anode insert comprising two rings and a cylindrical metal grid. The regime of the plasma injector and the delay time of the pulsed current generator were selected so as to insure that the critical current would be within 300–400 kA. The current pulse rise time was on a level of 1 μs. The currents were measured using a system of Rogowski loops.

Experimental results. The proposed POS switched current for both a positive and negative polarity of the central electrode. Figure 2 shows the typical oscillograms of currents in two cross sections between the current generator and the POS, measured for a negative polarity of the central electrode. As can be seen, the currents in these sections virtually coincide in the stage of conduction, during the jump in the plasma resistance, and in the subsequent stage. The plasma resistance in the conduction stage was ~25 mΩ (this value was determined using a function fit to an experimental oscillogram of the current). In the pulse presented in Fig. 2, the current transferred via plasma was 360 kA within 0.9 μs, the jump amplitude was 150 kA, and the current fall rate was 8×10^{12} A/s. As can be seen from Fig. 2, a high plasma resistance is retained for a long period of time. The character of erosion observed on the

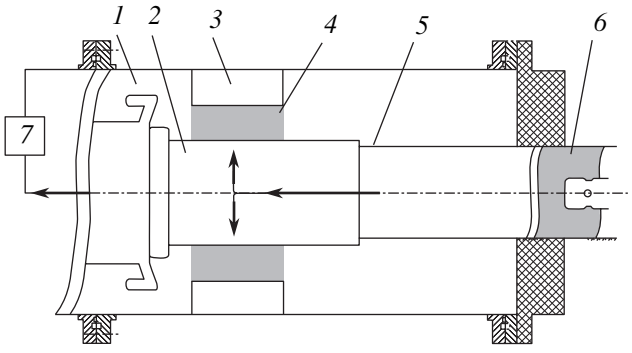

Fig. 1. Schematic diagram of the new inverse-pinch POS: (*1*) vacuum chamber; (*2*) central electrode; (*3*) outer electrode; (*4*) plasma layer; (*5*) plasma guide; (*6*) plasma injector; (*7*) driver.

1063-7850/05/3104-0312$26.00 © 2005 Pleiades Publishing, Inc.

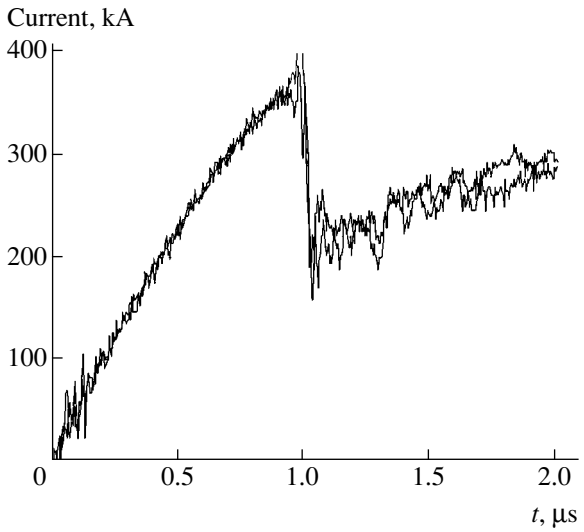

Fig. 2. Typical current oscillograms measured in two sections of the POS.

central electrode showed evidence of a high homogeneity of plasma in the POS region.

Conclusions. We implemented a new method for the formation of a plasma layer in a POS. An advantage of the proposed method is the possibility of using a single plasma injector placed outside the plasma chamber and ensuring high azimuthal homogeneity of a plasma layer in the POS. The current fall rate in the POS reached 8×10^{12} A/s at an initial buildup rate of 0.5×10^{12} A/s, which gives a ratio in excess of $K = 15$. High operation performance of the POS (high current fall rate, big jump amplitude, and high POS resistance retained for more than a microsecond) is reached without using external magnetic fields. The POS operated with currents in the 300–400 kA range for both positive and negative polarity of the central electrode.

REFERENCES

1. J. J. Moshella, R. C. Hazelton, C. Vidoli, and E. J. Yadlowsky, IEEE Trans. Plasma Sci. **28**, 2247 (2000).
2. V. V. Borovkov, E. P. Volkov, V. S. Zhdanov, *et al.*, in *Proceedings of the 13th IEEE International Pulsed Power Conference, Las Vegas, 2000*, p. 1458.

Translated by P. Pozdeev

Technical Physics Letters, Vol. 31, No. 4, 2005, pp. 314–315. Translated from Pis'ma v Zhurnal Tekhnicheskoĭ Fiziki, Vol. 31, No. 8, 2005, pp. 1–5.

Diffraction Calculation for an X-ray Refractive Kinoform Lens

L. I. Ognev

Institute of Nuclear Fusion, Russian Research Center Kurchatov Institute, Moscow, 123182 Russia

e-mail: ognev@nfi.kiae.ru

Received November 23, 2004

Abstract—The influence of thickness jump in a kinoform X-ray lens on transmitted beam formation in the near and far field has been studied for the first time using a numerical diffraction model. © *2005 Pleiades Publishing, Inc.*

The aperture of an X-ray beam transmitted through an X-ray refractive lens [1–3] is limited as a result of radiation absorption at the edge, where the lens thickness is relatively large [4]. In order to increase the effective aperture, it is possible to reduce the lens thickness in the peripheral region by an amount corresponding to the jump in the phase of the transmitted radiation by a multiple of 2π [5]. The most developed prototype of such a device is offered by a kinoform planar fern lens [5] comprising a set of numerous peripheral parts of a parabolic lens attached to the central part. This composite lens structure is multiply repeated so as to form a unified block. However, the presence of sharp jumps in the lens thickness at the boundaries between elements may give rise to diffraction effects. This paper reports on the results of the first investigation of such diffraction effects using a numerical method developed previously [6].

According to the proposed model, the system is described using step-by-step numerical integration of a parabolic quasi-optical equation for the complex amplitude $A(x, z)$ of the synchrotron radiation propagating along the z axis (coinciding with the optical axis of the lens):

$$2ik\partial A/\partial z = \Delta_\perp A + k^2[(\varepsilon - \varepsilon_0)/\varepsilon_0]A, \qquad (1)$$

where x is the transverse coordinate. The initial value of the wave amplitude at the entrance of the lens is determined by the distance from the radiation source and by the radiation source size:

$$A(x, z = 0) = A_0(x), \qquad (2)$$

where $k = \sqrt{\varepsilon_0}(\omega/c)$ is the wave vector and ε is the permittivity. It was assumed that the X-ray beam is narrow and has a Gaussian profile. The model can be generalized to the case of partly coherent radiation. In contrast to the paraxial approximation for a refractive lens with parabolic density profile [4], the numerical model used in this study allows refractive lenses with arbitrary profiles to be studied, including those with groove-like surfaces [2].

The results of numerical calculations of the transmitted radiation intensity on the axis of planar lens with a parabolic density profile are presented by curve *1* in Fig. 1. The calculations were performed for $1 - \varepsilon = 10^{-5}$, an imaginary part of the complex permittivity of 10^{-7}, and an X-ray beam energy of 12.4 keV. The position of the intensity maximum behind the lens was compared to the estimate obtained for the focal distance of a thin lens within the framework of geometrical optics. The focal length F of an elementary refractive lens as a function of the curvature radius R is given by the formula [4]

$$F = 2R/(1 - \varepsilon). \qquad (3)$$

For the above parameters, the focal length is $F = 6625$ mm, which is in good agreement with the results presented in Fig. 1.

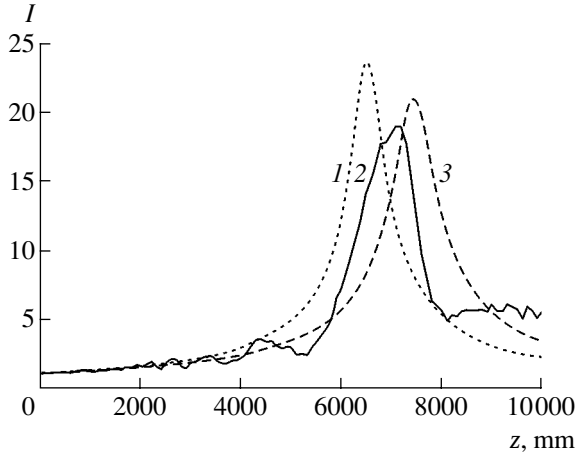

Fig. 1. Transmitted X-ray beam intensity profiles on the axis behind a parabolic refractive lens for a narrow incident 12.4-keV coherent beam: (*1*) single planar parabolic lens with a 40 μm thickness jump (corresponding to the exact phase shift); (*2*) kinoform lens with a reduced phase shift (35 μm thickness jump); (*3*) single planar parabolic lens with a reduced curvature of the central part (corresponding to that of lens *2*).

1063-7850/05/3104-0314$26.00 © 2005 Pleiades Publishing, Inc.

Consider a kinoform lens in which layers with thicknesses δd corresponding to phase shifts $n2\pi$ (where n is an integer) for a given wavelength λ are removed in the peripheral parts:

$$\delta d = n\lambda \cdot 2/(1-\varepsilon). \quad (4)$$

Calculations performed for a kinoform lens profile with a single phase shift corresponding to two wavelengths (equivalent to a thickness of about 40 μm) showed that the intensity at the focus increases by approximately 15% for the given parameters of the lens and the beam. In these calculations, the profile of the lens thickness variation was smoothened on a 0.1 μm scale.

In order to estimate the sensitivity of the system with respect to deviations of the lens thickness from the exact value given by expression (4), we have performed analogous calculations for a thickness jump reduced to 35 μm. The beam intensity variation on the axis behind the lens is in this case depicted by curve *2* in Fig. 1. For comparison, curve *3* shows the transmitted intensity for a parabolic lens with reduced curvature of the central part. As can be seen in curve *2*, there appear clear oscillations in the intensity (which were practically insignificant when the lens thickness jump corresponded to condition (4)). The intensity at the focus is 25% lower as compared to that for a kinoform lens with exact 4π phase shift.

Similar results were obtained upon modeling of the X-ray beam transmission through a system of 20 kinoform lenses with 40-μm-thick gaps. In this system, the intensity at the focus increases by a factor of 5, while the focal distance decreases by a factor of 20, which is in agreement with the geometrical optics approximation. Symmetric violation of the conditions of phase matching on the left and right edges of the central zone also leads to oscillations in the transmitted beam intensity on the lens axis in the far field. However, the most significant changes are still observed in the near field behind the lens.

Figure 2 shows the pattern of transmitted intensity variations inside a multielement lens. A region of smooth thickness variation in this case is observed at a distance of 51 μm from the lens axis. As can be seen, there also appears a trough in the radiation intensity distribution at the edge of the central region, where the lens thickness is large. This trough is related to absorption in the medium. At a greater distance from the edge, the intensity exhibits peaks. At the lens output, these peaks form a pattern characteristic of the diffraction at the screen edge. However, the appearance of such oscillations cannot significantly influence the beam formation in a compact device (such as a planar fern lens) with small extension along the axis [5], since these features occur (even at the lens exit) far from the edge of the first diffraction zone. However, in an extended X-ray lens composed of kinoform elements, the appearance of diffraction maxima at the edge of a high-order diffraction band may impose increased requirements on the accuracy of system adjustment relative to the beam. The beam intensity distribution in the focal spot behind the multielement lens has a simple structure and is close to a Gaussian profile in the transverse direction.

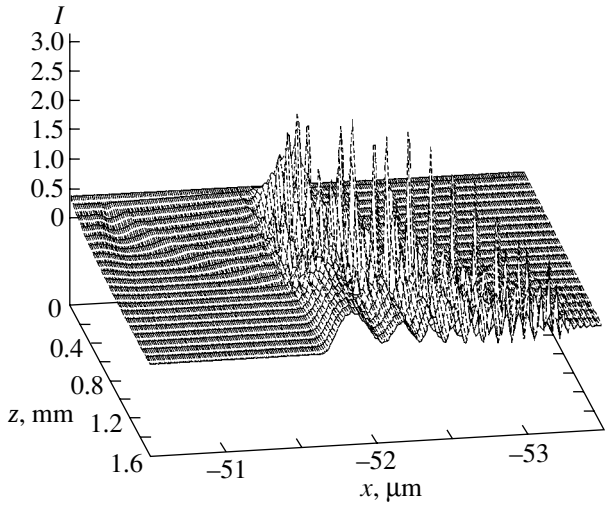

Fig. 2. X-ray beam intensity variation dynamics at a distance of 51 μm from the axis behind a multielement kinoform lens (20 elements with 40-μm gaps).

Thus, analysis of the diffraction model of an X-ray refractive kinoform lens shows that a sharp edge between the 0th and 1st diffraction bands leads to the appearance of fringes in the near-field intensity distribution. In the far field, the influence of this discontinuity is smoothened. At the same time, insufficiently accurate phase matching in the kinoform lens may significantly reduce the radiation intensity at the focus even in comparison to the parabolic lens. In the case of a partly coherent X-ray beam, these effects are less pronounced. Based on the results of this investigation, we may conclude that kinoform lenses can be used to increase the X-ray transmission through focusing systems.

REFERENCES

1. A. Snigirev, V. Kohn, I. Snigireva, and B. Lengeler, Nature **384** (7), 49 (1996).
2. B. Cedeström, R. Cahn, M. Danielsson, *et al.*, Nature **404**, 951 (2000).
3. Yu. I. Dudchik, N. N. Kol'chevskiĭ, and F. F. Komarov, Pis'ma Zh. Tekh. Fiz. **24** (24), 19 (1998) [Tech. Phys. Lett. **24**, 954 (1998)].
4. V. G. Kohn, Pis'ma Zh. Éksp. Teor. Fiz. **76**, 701 (2002) [JETP Lett. **76**, 600 (2002)].
5. I. Snigireva, A. Snigirev, C. Rau, *et al.*, Nucl. Instrum. Methods Phys. Res. A **467**–**468**, 982 (2001).
6. T. A. Bobrova and L. I. Ognev, Preprint No. IAE-6051/11 (Kurchatov Institute of Atomic Energy, Moscow, 1997); physics/9807033.

Translated by P. Pozdeev

Technical Physics Letters, Vol. 31, No. 4, 2005, pp. 316–318. Translated from Pis'ma v Zhurnal Tekhnicheskoĭ Fiziki, Vol. 31, No. 8, 2005, pp. 6–11.

On the Mechanism of Formation of Fullerenes and Carbon Nanotubes

M. V. Krasin'kova* and A. P. Paugurt

Ioffe Physicotechnical Institute, Russian Academy of Sciences, St. Petersburg, 194021 Russia

** e-mail: marina.shuv@mail.ioffe.ru*

Received July 14, 2004

Abstract—A possible mechanism of the formation of fullerenes and carbon nanotubes is proposed that is based on the notion of the strongly correlated state of π electrons in these materials (as well as in graphene layers). The presence of this state, in which the π electron densities on both sides of the carbon framework tend to be equal, decreases the energy of the system and stabilizes the carbon structure modifications under consideration. It is suggested that the graphene layer fragments considered as the initial material are polarized under the action of positive ions of inert gases or transition metals. This polarization leads to a redistribution of π electrons between the two sides of the initially planar graphene layer, which violates the equality of electron densities. As a result, the layer exhibits bending, which leads to the restoration of this equality. Under conditions of the strongly correlated π electron state, polarization not only modifies the state of hybridization of the polarized carbon atoms, but also leads to the formation of localized singlet pairs of π electrons (localized π-bonds). These changes maintain and additionally stabilize the curved structure upon termination of the polarizing action. © *2005 Pleiades Publishing, Inc.*

Many papers have been devoted to the search for mechanisms responsible for the formation of fullerenes and carbon nanotubes (CNTs) [1–3]. This interest is related primarily to the broad prospects for application of these materials in various fields of technology, in particular, nanoelectronics, as well as in biology and medicine. The most widely used method for the synthesis of fullerenes and CNTs is based on the electric arc discharge between graphite electrodes in an inert gas atmosphere. However, since the useful product yield is rather low, much research effort is devoted to increasing this yield; and this goal is difficult to achieve in the absence of knowledge about the mechanisms underlying the formation of carbon modifications under consideration. The elucidation of such mechanisms remains an important task.

It has been found that certain assumptions concerning the formation of fullerenes and CNTs can be made based on analysis of the behavior of π electrons in such structures, with allowance for a strong Coulomb repulsion between these electrons and their participation in the resonance π-bond formation, rather than within the traditional approach based on the model of molecular orbitals. In other words, the behavior of π electrons must be described using an approach somewhat analogous to that used for the description of the electron structure of benzene and certain other aromatic compounds [4–6].

According to this approach, π electrons exhibiting strong Coulomb repulsion (estimated for benzene at 10 eV [4, 5]) tend to locate on atomic orbitals at maximum distances from each other. Then, side-lobe overlap of the atomic $2p_z$ orbitals of carbon atoms (similar to that in benzene [6]) induces spin ordering, whereby the spins of π electrons in the neighboring atoms are oriented in the opposite directions. Under these conditions, all electrons with spins aligned in the same direction must occur on one side of the carbon framework, while electrons with the opposite spin orientation will occur on the other side. Thus, allowance for both the Coulomb repulsion between electrons and their involvement in π-bonding leads to the notion of a strongly correlated state of π electrons in these materials, which implies both spatial and spin ordering of electrons. However, it should be noted that the correlated state of π electrons in the new structural modifications of carbon and in graphene is different from that in benzene, since each π electron in the former structures is correlated with three neighboring π electrons, rather than with two as in benzene. This implies that some of the collective motions possible in benzene [5] are prohibited due to spin ordering in graphene, fullerenes, and CNTs.

The aforementioned strong Coulomb repulsion leads to the equality of π electron densities on both sides of the carbon framework, which stabilizes the structures (planar in graphene and curved in fullerenes and CNTs). In accordance with these notions, the new carbon modifications can form via a mechanism that favors curvature of the graphene layer fragments under external action as a result of the redistribution of π electrons between two sides of the layer. The curvature favors leveling of the electron densities as well as the attainment of a new stable state for the bent fragment.

1063-7850/05/3104-0316$26.00 © 2005 Pleiades Publishing, Inc.

It should be noted that we speak here of the deviation from planarity for small fragments of the graphene layer, involving only several carbon hexagons, that is, we consider the initial stage of the nucleation of fullerenes and CNTs.

One possible external factor acting upon the fragments of a graphene layer and inducing redistribution of the π electron density between two sides of the carbon framework is polarization under the action of positively charged ions possessing a high polarizing ability. The role of such ions can be played by positively charged helium ions and by doubly charged transition metal ions. The latter ions, capable of generating a stronger polarizing field, are necessary for the formation of nanotubes from graphene fragments involving a greater number of carbon hexagons.

Polarization of the graphene layer leads to deformation (elongation) of the $2p_z$ orbital of a polarized carbon atom in the direction of action of the polarizing force. This is accompanied by hybridization of this orbital with the other ones corresponding to a higher energy level. The closest energy level of a carbon atom to which a π electron can pass under the action of a polarizing force is the $2p_z \cdot 3s$ hybrid level, which is situated above the $2p_z$ level but below the $3s$ level.

Because of the strongly correlated state (primarily due to the spin ordering), the transition of one π electron to the $2p_z \cdot 3s$ hybrid level must be accompanied by the excitation of one of the three neighboring π electrons (having opposite spins and occurring on the opposite side of the carbon framework) to a similar hybrid level. This results in the formation of a singlet electron pair (i.e., a localized π-bond between the corresponding adjacent carbon atoms). The simultaneous "escape" of two π electrons from the correlated state, with the formation of a singlet pair in one polarization event, ensures the maintenance of the correlated state for all other π electrons, on the one hand, and makes the redistribution of π electrons irreversible upon termination of the polarizing action, on the other hand. Indeed, return to the previous distribution would require energy for the breakage of the π-bond.[1]

Now let us consider the experimental data, which might provide evidence for the proposed mechanism of formation of the new carbon modifications. First, it was suggested and then demonstrated that the initial materials for the formation of fullerenes and CNTs are graphene layer fragments [7, 8]. The proposed mechanism also considers graphene fragments as initial elements of the new carbon modifications. Second, the most effective method for the synthesis of fullerenes and CNTs is based on the electric arc discharge [3], in which the graphene layer fragments interact with positively charged ions of inert gases (such as helium or argon). Third, the introduction of transition metals (Fe, Co, Ni, etc.) into cathode materials increases the yield of CNTs [9, 10]. In the arc plasma, these metals occur in the form of positively charged ions with various degrees of ionization. The transition metal ions can effectively perform the same function of polarizing graphene layer fragments as do the inert gas ions.

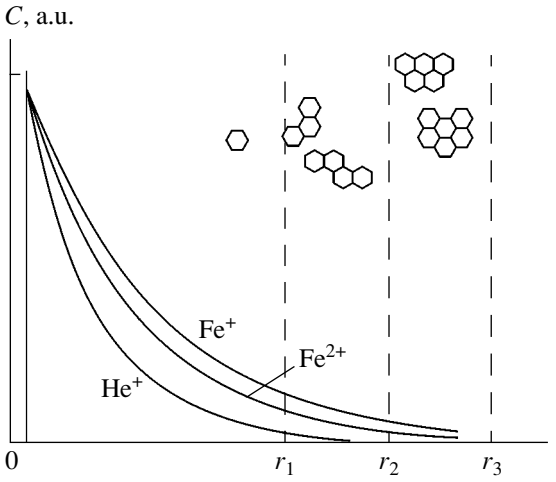

Schematic diagram showing the regions of existence of the graphene fragments and positive ions in the arc discharge plasma. The profiles of He^+, Fe^{2+}, and Fe^+ ion densities are plotted according to the ionization potentials of the corresponding atoms [12]. The regions (r_1–r_2) and (r_2–r_3) correspond to the possible formation of fullerenes and CNTs, respectively; note that the former region corresponds to a rather low density of positive ions, while the latter region contains almost no such ions.

The above considerations show that the electric arc discharge apparently provides all the conditions necessary for the synthesis of new carbon modifications via the proposed mechanism. However, this mechanism stipulates an effective interaction between the graphene layer fragments and the positive ions, whereas the efficiency of this interaction in conventional electric arc discharge reactors is by no means sufficiently high. As can be seen from data presented in the figure, the regions of existence of the graphene layer fragments and positively charged ions (characterized by different temperatures) in such systems are spatially separated. In order to provide for more effective interaction, measures must be taken so that these regions will overlap to a greater extent. The importance of the overlap of these

[1] In order to estimate the energy scale of these interactions, a change in the system energy can be evaluated using data on the polarization-induced variations in the multiplicity of bonds. For example, polarization of a graphene fragment consisting of two hexagons (leading to the nucleation of a fullerene structure) decreases the angle between C–C bonds from 120° to 108° (i.e., to the angle in pentagon). This bending is accompanied by a change in the multiplicity of four C–C bonds from 1.33 (in graphene) to 1.0, which requires approximately 2.1 eV. The energy spent for the hybridization of orbitals of two carbon atoms is about 3–3.5 eV. These expenditures are partly compensated by an increase in the multiplicity of the C–C bond about which the initial structure is bent: from 1.33 (in graphene) to 2.0 (which corresponds to a ~1.0 eV change in the bond energy). Thus, the estimated energy spent for the polarization is lower than the polarization energy in graphene (7.5 eV).

regions is confirmed by the effective formation of fullerenes and CNTs on the cathode walls [11]. In this case, sputtering of the cathode bombarded by inert gas ions leads to a yield of both carbon atoms (or ions) and clusters, including the graphene fragments, which automatically fall into the region of maximum positive ion density.

Thus, we have proposed a new mechanism for the formation of fullerenes and CNTs within the framework of the model of a strongly correlated state of π electrons. This mechanism is based on a purely electron process of the π electron density redistribution between two sides of an initially plane graphene layer, which results in bending of this layer.

REFERENCES

1. *Carbon Nanotubes: Synthesis, Structure, Properties, and Applications*, Ed. by M. S. Dresselhaus, G. Dresselhaus, and Ph. Avouris (Springer, Berlin, 2001); Top. Appl. Phys. **80** (2001).
2. W. Krätschmer, L. D. Lamb, K. Fostiropoulos, and D. R. Huffman, Nature **347**, 354 (1990).
3. G. A. Dyuzhev, Plasma Devices Op. **10**, 63 (2002).
4. L. V. Iogansen and V. V. Malov, Zh. Fiz. Khim. **52**, 2658 (1978).
5. L. V. Iogansen, Dokl. Akad. Nauk SSSR **189**, 281 (1969) [Sov. Phys. Dokl. **14**, 1071 (1969)].
6. L. V. Iogansen, Zh. Fiz. Khim. **59**, 1952 (1985).
7. L. S. K. Pang, L. Prochazka, R. A. Quezada, *et al.*, Energy Fuels **9**, 38 (1995).
8. A. P. Burden and J. L. Hutchison, Carbon **36**, 1167 (1998).
9. D. S. Bethune, C. H. Kiang, M. DeVries, *et al.*, Nature **363**, 605 (1993).
10. C. Journet, W. K. Maser, P. Bernier, *et al.*, Nature **388**, 757 (1997).
11. T. W. Ebbesen, Annu. Rev. Mater. Sci. **24**, 235 (1994).
12. L. V. Gurvich, G. V. Karachevtsev, V. N. Kondrat'ev, Yu. A. Lebedev, V. A. Medvedev, V. K. Potapov, and Yu. S. Khodeev, *Energy of Chemical Bond Rupture, Ionization Potentials, and Electron Affinity* (Nauka, Moscow, 1974) [in Russian].

Translated by P. Pozdeev

Technical Physics Letters, Vol. 31, No. 4, 2005, pp. 319–321. Translated from Pis'ma v Zhurnal Tekhnicheskoĭ Fiziki, Vol. 31, No. 8, 2005, pp. 12–18.

Kinetics of the Oriented Interaction of Accelerated Particles with Nonchiral Carbon Nanotubes

S. I. Matyukhin[a,*] and S. Yu. Grishina[b]

[a] *Orel State Technical University, Orel, Russia*

[b] *Orel State Agricultural University, Orel, Russia*

** e-mail: sim1@mail.ru*

Received October 28, 2004

Abstract—Kinetics of the channeling of accelerated particles in nonchiral carbon nanotubes (i.e., those with configurations other than armchair and zigzag) has been theoretically studied, with special attention devoted to the oriented motion of positive ions. Based on the stochastic equations of motion inside nanotubes, the Fokker–Planck equation for the function of particle distribution with respect to transverse variables is constructed on the basis of first principles. The solution of this equation provides simple analytical formulas for the radial distribution of moving particles, their distribution with respect to the transverse energy, and the length of particle dechanneling from nonchiral carbon nanotubes. © *2005 Pleiades Publishing, Inc.*

The existing methods of doping fullerenes and carbon nanotubes (CNTs), based predominantly on the introduction of impurities from vapor phase in the course of synthesis [1–3], are characterized by low efficiency and do not admit flexible modification of the doping regime, especially in multistage technological processes. Therefore, development of the methods for obtaining carbon nanostructures containing incorporated ions, atoms, or molecules is among the most important problems of nanotechnologies.

Recently, it was suggested [4–6] that this problem can be solved by doping materials with the aid of accelerated particle beams. Previously, we studied the dynamics of the oriented motion of accelerated particles in nonchiral CNTs (i.e., CNTs with configurations other than armchair and zigzag) [7–9] and established that this motion is quite expediently characterized as proceeding in the channeling mode [10, 11]. Moving in this regime, atomic particles may exhibit scattering on electrons and lose their energy before escaping from the nanotubes (stopping regime [7–9]). Therefore, by using the channeling effect and varying the particle beam energy, it is possible to select the optimum conditions for the ion implantation of dopants into CNTs.

This paper presents the results of our investigation into the kinetics of channeling for accelerated particles in nonchiral CNTs, with special attention devoted to the case of the oriented motion of positive ions.

In the case of ion channeling in nonchiral CNTs, the transverse energy component of the particle energy ($E_\perp$) relative to the nanotube axis and the angular momentum (μ) relative to this axis are the adiabatic invariants [8, 9]. Therefore, the total particle distribution function $\Phi(r, \varphi, \mu, E_\perp; t)$, where r and φ are the transverse polar coordinates of a particle at any time t, can be represented as

$$\Phi(r, \varphi, \mu, E_\perp; t) = \frac{\Phi(\mu, E_\perp; t)}{C(\mu, E_\perp)\sqrt{E_\perp - \frac{\mu^2}{2Mr^2} - U(r)}}. \quad (1)$$

Here, $C(\mu, E_\perp)$ is a normalization factor given by the formula

$$C(\mu, E_\perp) = 2\pi \int\limits_{R(\mu, E_\perp)} \frac{dr}{\sqrt{E_\perp - \frac{\mu^2}{2Mr^2} - U(r)}}; \quad (2)$$

$R(\mu, E_\perp)$ is the region accessible to the motion of particles as determined by the condition

$$E_\perp - \frac{\mu^2}{2Mr^2} - U(r) \geq 0; \quad (3)$$

$U(r)$ is the continuous potential describing the interaction of particles with the CNT walls [7–9], $M \approx Am_p$ is the particle mass, and m_p is the proton mass.

In expression (1), the function $\Phi(\mu, E_\perp; t)$ describes the distribution of particles with respect to slowly varying quantities $E_\perp$ and μ as well as the temporal evolution of this distribution, which is determined by the action of random forces related to a discrete wall structure, thermal oscillations of carbon atoms, and scattering on atomic-shell electrons. The time variation of the

1063-7850/05/3104-0319$26.00 © 2005 Pleiades Publishing, Inc.

function $\Phi \equiv \Phi(\mu, E_\perp; t)$ is described by the Fokker–Planck equation

$$\frac{\partial \Phi}{\partial t} = \frac{\partial}{\partial \mu}\left[A_0 \mu \Phi + \frac{D_0}{\omega_0^2} E_\perp \frac{\partial \Phi}{\partial \mu} + D_0 \mu \frac{\partial \Phi}{\partial E_\perp}\right] + \frac{\partial}{\partial E_\perp}\left[A_0 E_\perp \Phi + D_0 \mu \frac{\partial \Phi}{\partial \mu} + D_0 E_\perp \frac{\partial \Phi}{\partial E_\perp}\right], \quad (4)$$

which is obtained proceeding from, which have first principles using standard methods of the theory of random processes [12–14] based on the stochastic equations of the motion of particles inside CNTs in the harmonic approximation for a given potential $U(r)$. In Eq. (4), ω_0 is the transverse oscillation frequency, A_0 is the drift coefficient, and D_0 is the diffusion coefficient, which are determined entirely by the random forces acting upon channeled particles (ions). The results of our calculations showed that the most significant effect is produced by the random forces related to ion scattering on electrons, so that

$$A_0 \approx \frac{1}{Mv}\left(\frac{dE}{dz}\right)_e, \quad D_0 \approx \frac{m_e v}{M}\left(\frac{dE}{dz}\right)_e, \quad (5)$$

where $(dE/dz)_e$ is the average ion energy losses as a result of this scattering, v is the ion velocity, and m_e is the electron mass.

Equation (4) must be solved for the initial condition $\Phi(\mu, E_\perp; 0) = \Phi_0(\mu, E_\perp)$ and the boundary conditions

$$\Phi(\mu, 0; t) < +\infty, \quad \Phi(\mu, E_{\perp c}; t) = 0. \quad (6)$$

These boundary conditions correspond to a limited flux of particles for $E_\perp = 0$ and imply dechanneling of the particles with a critical transverse energy $E_{\perp c} = E\psi_c^2$, where E is the total particle energy and ψ_c is the critical channeling angle [9].

A solution to Eq. (4) can be obtained using the method of separation of the variables. For ions with the energy $E > 0.5A(m_p/m_e)E_{\perp c}$ (A is the ion mass expressed in amu), which have penetrated to a sufficiently large depth z into the nanotube, the solution can be written as

$$\Phi(\mu, E_\perp; z) \approx C_1\left(1 - \frac{E_\perp + \omega_0\mu}{E_{\perp c} + \omega_0\mu}\right)\left(1 - \frac{E_\perp - \omega_0\mu}{E_{\perp c} - \omega_0\mu}\right)\exp\left(-\frac{z}{R_{ch}(\mu)}\right), \quad (7)$$

where C_1 is the normalization factor determined by the initial distribution of particles,

$$C_1 \approx \frac{27\omega_0}{E_{\perp c}^2}\int_0^{E_{\perp c}} dE_\perp \int_0^{E_\perp/\omega_0} d\mu \Phi_0(\mu, E_\perp) \times\left(1 - \frac{E_\perp + \omega_0\mu}{E_{\perp c} + \omega_0\mu}\right)\left(1 - \frac{E_\perp - \omega_0\mu}{E_{\perp c} - \omega_0\mu}\right), \quad (8)$$

and $R_{ch}(\mu)$ is the dechanneling length for ions with the angular moment μ,

$$R_{ch}(\mu) \approx A\frac{m_p}{m_e}\frac{E_{\perp c}^2 - \omega_0^2\mu^2}{4E_{\perp c}(dE/dz)_e}. \quad (9)$$

As can be seen from expression (9), dechanneling takes place most rapidly for the particles with $\mu \neq 0$. Therefore, at a sufficiently large depth z inside the nanotube, only ions with very small angular moment ($\mu \approx 0$) relative to the CNT axis will be retained, for which

$$\Phi(\mu, E_\perp; z) \approx C_1\left(1 - \frac{E_\perp}{E_{\perp c}}\right)^2 \delta\left(\frac{\omega_0\mu}{E_{\perp c}}\right)\exp\left(-\frac{z}{R_{ch}}\right), \quad (10)$$

where $\delta(\mu)$ is the Dirac delta function. For these ions, the dechanneling length is

$$R_{ch} \approx \frac{Am_p/m_e}{4(dE/dz)_e}E_{\perp c}, \quad (11)$$

and the radial distribution can be found by integrating expression (1) with respect to the transverse variables $E_\perp$, μ, and φ:

$$\Phi(r; z) \approx C_1^*\left(1 - \frac{U(r)}{E_{\perp c}}\right)^{5/2}\exp\left(-\frac{z}{R_{ch}}\right), \quad (12)$$

where C_1^* is determined from the condition of normalization to C_1 given by formula (8) at $z = 0$.

From the standpoint of ion implantation into nonchiral CNTs, the most interesting case corresponds to the channeling of ions with the energies $E \leq 0.5A(m_p/m_e)E_{\perp c}$. These particles rapidly lose their energy in the course of scattering on electrons and practically cannot escape from CNTs, so that their dechanneling length is infinitely large ($R_{ch} \longrightarrow \infty$). The angular moment of such ions vanishes ($\mu \longrightarrow 0$) over the time $\tau \approx Mv(dE/dz)_e^{-1}$. The corresponding distribution with respect to the transverse energy according to Eq. (4) is

$$\Phi(\mu, E_\perp; z) \approx C_0\delta(\mu)\exp\left(-\frac{E_\perp}{T_\perp}\right), \quad (13)$$

which is the Boltzmann distribution with a small transverse temperature

$$T_\perp \approx \frac{2m_e}{Am_p}E \quad (14)$$

and a normalization C_0 factor determined by the initial distribution $\Phi_0(\mu, E_\perp)$:

$$C_0 \approx \frac{1}{T_\perp}\int_0^{E_{\perp c}} dE_\perp \int_0^{E_0/\omega_0} d\mu \Phi_0(\mu, E_\perp). \quad (15)$$

The radial distribution of particles corresponding to the energy distribution (13) is

$$\Phi(r; z) \approx C_0^* \mathrm{erf}\left(\sqrt{\frac{E_{\perp c} - U(r)}{T_\perp}}\right)\exp\left(-\frac{U(r)}{T_\perp}\right), \quad (16)$$

where C_0^* is determined from the condition of normalization to C_0 given by formula (15) at $z = 0$.

Thus, the results presented above show that nonchiral CNTs are most effectively implanted using ion beams with the energies $E \le 0.5A(m_p/m_e)E_{\perp c}$. If the angle between the beam direction and the nanotube axis is below the critical value ψ_c [7–9], the ions move in the channeling mode and their distribution with respect to the transverse energy is described (irrespective of the initial distribution) by a Boltzmann function (13) with a small transverse temperature (14), while the radial distribution is described by function (16).

If the nanotube length L is equal to or greater than the characteristic value $L_0 \approx E(dE/dz)_e^{-1}$, the channeled particles rapidly lose energy in the course of scattering on electrons and are retained inside CNTs with the formation of endohedral structures (channeling in the stopping regime [7–9]). Otherwise, for $L < L_0$, the channeled particles are transmitted via CNTs without stopping. The output beam divergence $\beta \approx \sqrt{T_\perp/E} = \sqrt{2m_e/(Am_p)} \approx 3.3 \times 10^{-2}/\sqrt{A}$ is determined only by the transverse temperature (14) and is independent of the initial beam divergence. In this regime, the ion beam is focused by relatively short CNTs [7–9].

Acknowledgments. The work was supported by the Russian Foundation for Basic Research (project no. 03-03-96488).

REFERENCES

1. A. V. Eletskiĭ, Usp. Fiz. Nauk **170**, 113 (2000) [Phys. Usp. **43**, 111 (2000)].
2. *Proceedings of the International Winter School on Electronic Properties of Novel Materials: Molecular Nanostructures*, Ed. by H. Kuzmany, R. Siegmar, and M. Michael (World Scientific, Singapore, 1998).
3. *Science and Application of Nanotubes*, Ed. by D. Tomanek and R. J. Enbody (Kluwer, New York, 2000).
4. V. V. Rozhkov and S. I. Matyukhin, in *Proceedings of the 15th International Conference on Physics of Radiation Phenomena and Radiation Science, Kharkov, 2002*, p. 277.
5. S. I. Matyukhin, in *Proceedings of the 1st All-Russia Conference on Physicochemical Processes in Condensed State and on Interfaces, Voronezh, 2002*, p. 217.
6. S. I. Matyukhin, in *Proceedings of the International Conference on Chemistry of Solids and Modern Micro- and Nanotechnologies, Stavropol, 2002*, p. 77.
7. S. I. Matyukhin and S. Yu. Grishina, in *Proceedings of the 15th All-Russia Symposium on Actual Chemical Physics, Moscow, 2003*, p. 71.
8. S. I. Matyukhin and S. Yu. Grishina, in *Proceedings of the 12th International Conference on Radiation Physics and Chemistry of Condensed Matter, Tomsk, 2003*, p. 344.
9. S. I. Matyukhin and S. Yu. Grishina, Pis'ma Zh. Tekh. Fiz. **30** (20), 76 (2004) [Tech. Phys. Lett. **30**, 877 (2004)].
10. J. Lindhard, Mat.-Fys. Medd. Dan. Vid. Selsk. **34** (14), 49 (1965).
11. Y.-H. Ohtsuki, *Charged Beam Interaction with Solids* (Taylor and Francis, London, 1983).
12. A. S. Bakaĭ, G. Ya. Lyubarskiĭ, and V. V. Rozhkov, Zh. Tekh. Fiz. **35**, 1525 (1965) [Sov. Phys. Tech. Phys. **10**, 1183 (1965)].
13. V. V. Rozhkov, Phys. Status Solidi B **5**, 463 (1979).
14. C. W. Gardiner, *Handbook of Stochastic Methods for Physics, Chemistry, and the Natural Sciences* (Springer-Verlag, Berlin, 1983).

Translated by P. Pozdeev

Technical Physics Letters, Vol. 31, No. 4, 2005, pp. 322–324. Translated from Pis'ma v Zhurnal Tekhnicheskoĭ Fiziki, Vol. 31, No. 8, 2005, pp. 19–23.

Thermal Ionization of Amines Controlled by the Electric-Field-Driven Transport of Alkali Metal Cations

M. V. Knat'ko, M. N. Lapushkin*, and V. I. Paleev

Ioffe Physicotechnical Institute, Russian Academy of Sciences, St. Petersburg, 194021 Russia

** e-mail: lapushkin@ioffe.rssi.ru*

Received December 2, 2004

Abstract—A method for controlling the yield of ionized products from a heterogeneous reaction of amines on the surface of an Na_xAu_y alloy is proposed, which is based on the effect of a weak electric field on the diffusion of Na^+ ions. © *2005 Pleiades Publishing, Inc.*

Investigations into methods of controlling the rates of chemical reactions are of interest from the standpoint of basic knowledge and have important practical applications. This is also valid for the control over heterogeneous reactions proceeding between particles of various natures occurring on solid surfaces. By studying the possibility of controlled variation of the rates of physicochemical processes in the adsorbed layer in the simplest model systems, it is possible to obtain important information concerning the development of effective methods for the control over heterogeneous reactions in complicated technological processes. Such a model system was realized in our study of the coadsorption of alkali metal atoms and amine molecules on the surface of gold–alkali metal alloys.

Investigations of the surface ionization of alkali metal atoms adsorbed on a heated surface of gold showed that adsorbate–substrate interaction leads to the formation of surface alloys with the composition Alk_xAu_y (Alk = Na, K, Cs) [1–6]. This Alk_xAu_y alloy exhibits the properties of a wide-bandgap semiconductor with the forbidden band width reaching 2.6–2.8 eV [1, 7]. These Alk_xAu_y films are thermally stable in vacuum and exhibit significant thermal destruction only upon heating to $T > 1250$ K. At $T > 600$ K, the alloy film begins to emit Alk^+ ions (both in the case of alkali metal supply from an external source and in the course of intrinsic thermionic emission) [2, 5]. The ion current can be controlled by stimulating the escape of alkali metal atoms at the surface, for example, by irradiating the emitter surface with photons possessing an energy $h\nu > 2.6$ eV [2, 8].

The coadsorption of Na atoms and diethylamine ($M = (C_2H_5)_2NH$) molecules on a heated Na_xAu_y alloy surface activated by oxygen is accompanied by the thermodesorption of polyatomic ions. The mass spectrum of desorbed species reveals the products of decomposition of M molecules and their associates with Na, H_2O, and O_2 [9]. The thermodynamically equilibrium process of the surface ionization of M molecules on "pure" and oxidized metals has been studied in sufficient detail [10, 11]. A comparison of the thermodesorption mass spectra and the temperature dependences of ion currents shows that polyatomic ions appear in the alloy film as a result of a heterogeneous process involving sodium [9], rather than due to surface ionization.

In order to elucidate the role of the charged state of adsorbed alkali metal species in the heterogeneous reactions involving organic compounds, we have first studied the processes leading to the appearance of Na^+ ions on the alloy surface [12]. It was found that a thin (not exceeding five monolayers) dielectric film of Na_xAu_y hinders tunneling electron exchange between adatoms and the substrate and prevents the establishment of charge equilibrium in this adsorption system. The Na^+ ions appear due to a multistage process involving the diffusion transfer of Na adatoms inside the alloy, ionization of the part of these atoms reaching the alloy–gold interface, electron transition to the metal, and reverse diffusion of Na^+ ions to the surface, rather than as a result of the surface ionization process. Based on these results, a method was developed for controlling the yield of Na^+ ions at the alloy film surface by applying a weak electric field affecting the transport of ions in the alloy [12].

Then, using a controlled variation of the surface concentration of sodium, we elucidated the role of the charged state of adsorbed alkali metal species in heterogeneous reactions of M molecules on the Na_xAu_y film surface, which are accompanied by the desorption of polyatomic ions. For this purpose, we changed the surface concentration of sodium in the adlayer using two methods: (i) photostimulated escape of neutrals and ions at the surface [2, 8] and (ii) electric-field-driven

1063-7850/05/3104-0322$26.00 © 2005 Pleiades Publishing, Inc.

transport of Na^+ ions from the volume to the surface of the alloy film. The experimental procedure and conditions were analogous to those described previously [2, 4–9, 12].

The typical results presented in Fig. 1 show that the yield of the reaction products (M–H) formed upon hydrogen detachment from the M molecules is uniquely determined by the concentration of sodium in the surface layer, which is changed via irradiation of the emitter by light with a quantum energy $h\nu > 2.6$ eV. Sodium species do not enter into the detected ions $(M–H)^+$ and play the role of active centers in the heterogeneous process under consideration. Since the emergence of the alkali metal at the surface is related to the photoinduced decomposition of the alloy in the near-surface layer of the film, this action may change the densities of both neutral and charged components in the total sodium flux to the surface. Then, a question arises concerning the role of each component in the heterogeneous reaction and in the ionization of the reaction products.

An answer to this question is provided by the results of investigation of the influence of the electric-field-driven transport of sodium cations on the process under consideration (Fig. 2). A comparison of the behavior of the emission currents of Na^+ and $(M–H)^+$ ions leads to the conclusion that Na^+ ions occurring on the alloy film surface are in fact the active centers responsible for the course of chemical reactions and the ionization of reaction products. Apparently, when an amine molecule and a nitrogen ion meet in the adlayer, the free electron of an electron pair localized at the nitrogen atom of amine passes to the ion that initiates the decomposition of M molecules with the detachment of H atoms or CH_3 radicals. The experiments showed that the emission of associated ions varies synchronously with the yield of Na^+ ions at the surface. This is evidence that Na^+ ions play the role of the reaction centers in the associated heterogeneous processes leading to the emission of complex ions such as $[(C_2H_5)_2N(CH_2)_nNa]^+$, $[C_2H_5(CH_2)_nNHONa]^+$, and $[C_2H_5(CH_2)_nNHNa]^+H_2O$, where the index n varies within the interval $1 \le n \le 8$. The determining role of the alkali metal ions in reactions on the gold surface suggests that photostimulated decomposition of the Na_xAu_y alloy leads to the formation of Na^+ ions. The photoinduced rupture of Na–Au bonds is accompanied by electron transfer from a part of Na atoms to the conduction band of the semiconducting alloy and by the appearance of free Na^+ ions. The escape of these free ions at the surface accounts for the coincidence of the shapes of Na^+ and $(M–H)^+$ ion currents in Fig. 1.

The role of oxygen in the observed increase in ion emission [9] reduces to cleaning the surface from residual hydrocarbons that are not involved in the ion formation reactions but hinder these reactions. The method developed in this study can be used in investigations of ion transport in membranes and ion exchangers [13, 14].

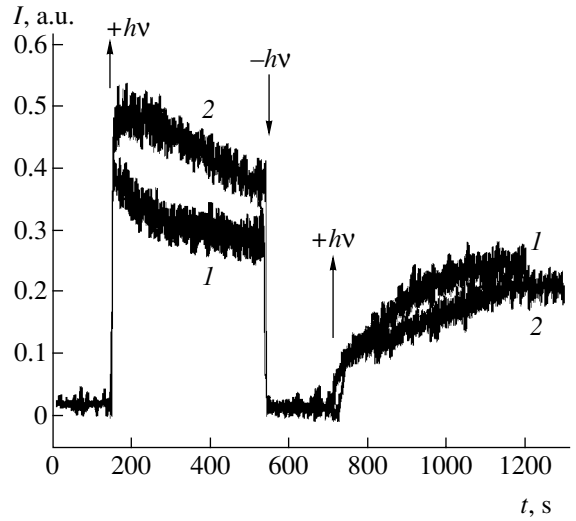

Fig. 1. Experimental time series of the ion thermodesorption current (T = 1100 K) from an emitter illuminated at $h\nu > 2.6$ eV: (*1*) Na^+; (*2*) $(C_4H_{10}N)^+$.

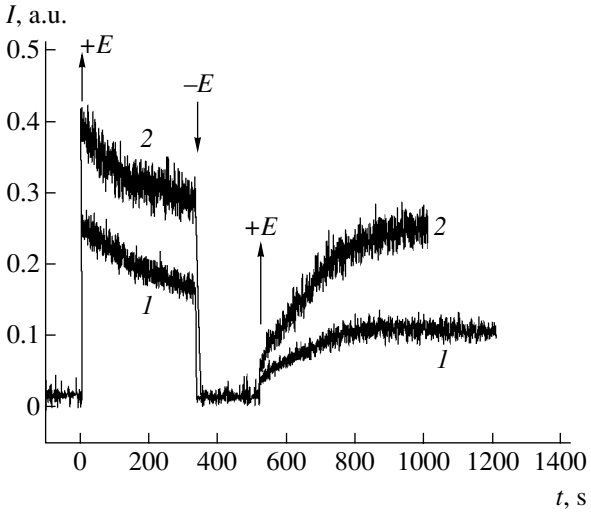

Fig. 2. Experimental time series of the ion thermodesorption current (T = 1100 K) from an emitter exposed to an external electric field accelerating ions ($E \sim 1 \times 10^3$ V/cm^2): (*1*) Na^+; (*2*) $(C_4H_{10}N)^+$.

Acknowledgments. This study was supported by the federal program “Surface Atomic Structures” (project no. 1152).

REFERENCES

1. W. E. Spicer, A. H. Sommer, and J. G. White, Phys. Rev. **115**, 57 (1959).
2. E. Ya. Zandberg, M. V. Knat’ko, V. I. Paleev, *et al.*, Pis’ma Zh. Tekh. Fiz. **21** (19), 15 (1995) [Tech. Phys. Lett. **21**, 774 (1995)].

3. M. V. Knat'ko, M. N. Lapushkin, and V. I. Paleev, Pis'ma Zh. Tekh. Fiz. **24** (10), 48 (1998) [Tech. Phys. Lett. **24**, 390 (1998)].
4. M. V. Knat'ko, V. I. Paleev, and E. Ya. Zandberg, Phys. Low-Dimens. Semicond. Struct. **7**–**8**, 27 (1996).
5. M. V. Knat'ko, V. I. Paleev, and M. N. Lapushkin, Phys. Low-Dimens. Semicond. Struct. **5**–**6**, 85 (1998).
6. M. V. Knat'ko, M. N. Lapushkin, and V. I. Paleev, Phys. Low-Dimens. Semicond. Struct. **9**–**10**, 85 (1999).
7. M. V. Knat'ko, M. N. Lapushkin, and V. I. Paleev, Zh. Tekh. Fiz. **68** (10), 108 (1998) [Tech. Phys. **43**, 1235 (1998)].
8. M. V. Knat'ko, V. I. Paleev, and M. N. Lapushkin, Zh. Tekh. Fiz. **68** (10), 104 (1998) [Tech. Phys. **43**, 1231 (1998)].
9. M. V. Knat'ko, M. N. Lapushkin, and V. I. Paleev, Zh. Tekh. Fiz. **74** (7), 99 (2004) [Tech. Phys. **49**, 905 (2004)].
10. E. Ya. Zandberg and U. Kh. Rasulev, Usp. Khim. **51**, 1425 (1982).
11. U. Kh. Rasulev and E. Ya. Zandberg, Prog. Surf. Sci. **28** (3–4), 181 (1988).
12. M. V. Knat'ko, M. N. Lapushkin, and V. I. Paleev, Zh. Tekh. Fiz. **75** (4), 109 (2005) [Tech. Phys. **50**, 498 (2005)].
13. A. B. Yaroslavtsev, Usp. Khim. **66**, 641 (1997).
14. A. B. Yaroslavtsev, V. V. Nikonenko, and V. I. Zabolotskiĭ, Usp. Khim. **72**, 438 (2003).

Translated by P. Pozdeev

Technical Physics Letters, Vol. 31, No. 4, 2005, pp. 325–328. Translated from Pis'ma v Zhurnal Tekhnicheskoĭ Fiziki, Vol. 31, No. 8, 2005, pp. 24–31.

Criteria for the Optimization of Parameters of a Multibunch Scheme of Wakefield Acceleration

I. L. Sheinman* and A. D. Kanareykin

St. Petersburg State Electrotechnical University, St. Petersburg, 197376 Russia

** e-mail: isheinman@yandex.ru*

Received November 2, 2004

Abstract—We propose criteria for the optimization of a wakefield acceleration scheme in a dielectric-lined waveguide structure, which is aimed at increasing the efficiency of energy transfer from the driving to witness (driven) electron bunches with simultaneous increase in the accelerating field gradient. It is suggested to use a multimode acceleration structure excited by a train of short electron bunches profiled in a special manner. The proposed scheme provides for a maximum energy transformer ratio simultaneously with an increase in the wakefield as compared to the values typical of the traditional linear acceleration scheme. *© 2005 Pleiades Publishing, Inc.*

The technology of dielectric wakefield electron accelerators employing the Vavilov–Cherenkov effect is one of the most promising directions in the development of high-field-gradient structures for modern linear accelerators, and it has been extensively studied in recent years [1–10]. The main element of such an accelerating structure is a cylindrical metal waveguide filled with a dielectric and having an axial vacuum channel. A short (1–4 mm) driving electron bunch possessing a large charge (20–100 nC) and traveling along the channel generates a TM_{01} wakefield mode of the Cherenkov radiation with a longitudinal electric field component. The subsequent high-energy witness (driven) electron bunch with a small charge, following the former bunch with a certain delay selected so as to fit to the accelerating phase of the wakefield, is accelerated by this field up to an energy of 0.1–1 GeV [1–3]. This principle of acceleration was successfully demonstrated in experiments carried out using the Argonne Wakefield Accelerator (AWA) [1] at the Argonne National Laboratory (USA).

The factors of key importance in wakefield acceleration are the increase in the energy transformer ratio R and the accelerating wakefield E^+, which are the parameters characterizing the efficiency of the acceleration process [4–7]. The R value is defined as the ratio of the maximum electron energy increment in the witness bunch to the maximum electron energy loss in the driving bunch.

The traditional wakefield accelerator implements a collinear scheme, in which the driven and driving electron bunches travel along the same axis. However, collinear systems are characterized by limited total energy increment for the driven bunch. In accordance with the wakefield theorem [6], electrons in the driven bunch cannot increase their energy by an amount exceeding doubled electron energy in the driving bunch. Accordingly, wakefield accelerators implementing the scheme with electron bunches moving along the same axis (with a symmetric driving bunch) have $R \le 2$.

Figures 1a and 1b show diagrams of the two multibunch schemes suggested to increase the energy trans-

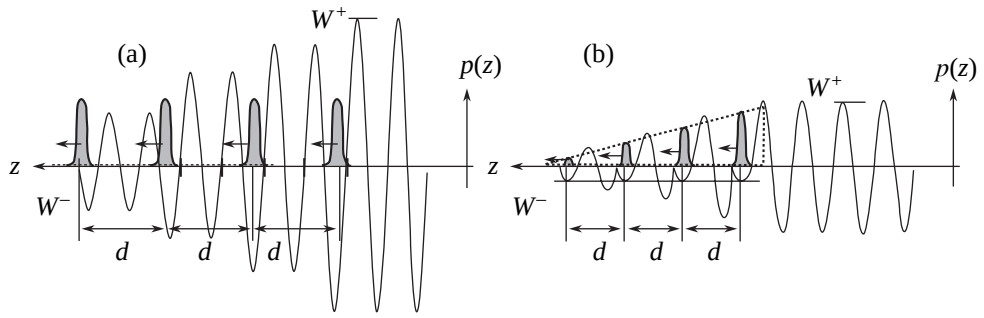

Fig. 1. Multibunch wakefield acceleration schemes: (a) the FBT scheme providing for the maximum accelerating field E^+; (b) the RBT scheme ensuring the maximum energy transformer ratio R. See text for explanations.

1063-7850/05/3104-0325$26.00 © 2005 Pleiades Publishing, Inc.

former ratio and the accelerating wakefield. In order to provide for $R > 2$, it was suggested [8, 9] to use a train of Gaussian bunches with a period of d (Fig. 1b) having a triangular envelope (ramped bunch train, RBT). The charge in this train varies from a minimum for the first bunch to a maximum for the last bunch, as depicted by the dashed line in Fig. 1b. As can be seen from this figure, the four leading bunches in the train are subjected to the action of a relatively low retarding field of the same amplitude. A high efficiency of energy transfer from the train of driving bunches to the field in the RBT mode is achieved at the expense of increasing distance traveled by these bunches.

Another scheme, employing a flat bunch train (FBT), provides for an increase in the accelerating field (Fig. 1a). This scheme is based on the coherent interference of fields generated by bunches in the train. The retarding fields acting upon the leading bunches rapidly grow with the bunch number in the train (Fig. 1a), but the distance over which the energy is taken is relatively short.

Selection and development of the acceleration scheme depend to a significant extent on the presence of transverse deflecting fields. An analysis of the transverse dynamics for a train of high-current bunches shows that a radial deviation of the beam poses limitations on the distance l traveled by bunches in the waveguide [3, 10]. An excess deviation caused by the deflecting forces results in that the beam interacts with the waveguide wall and further acceleration becomes impossible. Therefore, the transverse instabilities restrict the possibility of gaining energy from the train of driving bunches.

Thus, a problem arises concerning the selection and optimization of the accelerating scheme for a given length of the accelerator. A criterion for the efficiency of such a scheme is the maximum energy $\Delta W^+ = \int e E^+ dl$ transferred to a driven bunch from the train of driving bunches traveling a given distance. Under the condition that the driven bunch occurs at the maximum of the accelerating wakefield, this maximum can be determined as $\Delta W^+ = eE^+l$. On the other hand, the same energy can be determined via the retarding field as $\Delta W^+ = \int e R E_\mathrm{m}^- dl = eRE_\mathrm{m}^- l$, where E_m^- is the maximum absolute value of the retarding field acting upon the driving bunches.

The maximum ΔW^+ value is provided by simultaneous maximization of the R and E_m^- values. For a sufficiently high energy of the driving bunches, such that $W_\mathrm{d} \cong m_0 c^2 \sqrt{l/\lambda}$ (W_d is the starting electron energy in the driving bunch, m_0 is the electron rest mass, c is the velocity of light, and λ is the wakefield wavelength), the maximum retarding field can be determined from the condition of maximum possible energy gained from the driving bunches: $E_\mathrm{m}^- \approx \alpha W_\mathrm{d}/(el)$. The coefficient α, which falls in the interval 0.2 to 0.9, characterizes the fraction of the driving bunch energy that can be transferred to the wakefield under given experimental conditions. This coefficient is determined by the deflecting fields leading to the development of transverse instabilities, the accuracy of beam introduction into the axial channel of the waveguide, and the adjustment of the focusing system of the accelerator.

For the maximum retarding field (corresponding to the given accelerator length), the given starting energy, and the maximum possible charge of the driving bunches, the problem reduces to finding the optimum bunch train ensuring the maximum energy transformer ratio R.

Consider a system of charges comprising N driving bunches with the charges $q_1, q_2, \ldots, q_N$ spaced from each other by the distances $d_1, d_2, \ldots, d_{N-1}$, respectively, and a witness bunch with the charge $q \ll q_i$, spaced by d from the last driving bunch. The field acting upon the jth bunch is $E_j = \sum_{i \le j} q_i f(\Delta\zeta_{i,j})$, where $\Delta\zeta_{i,j}$ is the distance between the ith and jth bunches and f is a function describing the structure of a wakefield generated in the waveguide by a unit charge.

The longitudinal wakefield in a dielectric accelerating waveguide structure excited by an axial current distribution in a single bunch approximation was mathematically simulated using the analytical theory developed in [5]. In most cases, the experimental electron bunches can be described by a normal charge density distribution in the space. The electric field of such a Gaussian bunch can be determined by taking an integral convolution of the field of a point charge with a charge distribution in the bunch:

$$f(\zeta) = \begin{cases} \sum_{n=0}^{\infty} \left(\Psi_{E_{zn}}(f_n, r) \frac{1}{\sigma\sqrt{2\pi}} \int_{-\infty}^{\zeta} \exp\left(-\frac{\zeta^2}{2\sigma^2}\right) \right. \\ \left. \times \cos(k_{zn}(s-\zeta)) ds \right), \quad |\zeta| \le 3\sigma, \\ \sum_{n=0}^{\infty} \Psi_{E_{zn}}(f_n, r) \exp\left(\frac{-k_{zn}^2\sigma^2}{2}\right) \cos(k_{zn}\zeta), \\ |\zeta| > 3\sigma, \end{cases}$$

where σ is the mean-square bunch length, $\zeta = z - Vt$ is the distance behind the bunch, $k_{zn} = \omega_n/(\beta c)$ is the longitudinal component of the wave vector of the wakefield, ω_n are the eigenfrequencies of the waveguide (dependent on the waveguide geometry and dielectric properties), and $\Psi_{E_{zn}}(\omega_n, r)$ are the coefficients dependent on the waveguide geometry, the dielectric permittivity, and the initial position of the electron bunch.

Introducing the notation $a_0 = f(0)$, $a_{ij} = f(\sum_{k=i}^{j-1} d_k)$, and $a_{i,N+1} = f(d + \sum_{k=i}^{j-1} d_k)$ ($i = 1, 2, \ldots, N$; $j = 1, 2, \ldots, N$), it is possible to express the retarding fields acting upon the driving bunches as $E_j^- = \sum_{i=1}^{j} q_i a_{ij}$, and the field accelerating the witness bunch, as

$$E^+ = \sum_{i=1}^{N} q_i a_{i,N+1} + qa_0 \approx \sum_{i=1}^{N} q_i a_{i,N+1}.$$

In experiment, the charge of the driving bunches is limited by the technical possibilities of the accelerating setup and cannot exceed a certain maximum value Q_m. Accordingly, the total charge of the bunch train is restricted to $Q_\mathrm{S} \le NQ_\mathrm{m}$. Therefore, the problem of optimization of the charge distribution in a train of driving bunches used in a multibunch accelerating scheme reduces to maximization of the linear form E^+ under the conditions

$$0 \le \left|E_j^-\right| \le E_\mathrm{m}^-, \quad 0 \le q_i \le Q_\mathrm{m}, \quad \sum_{i=1}^{N} q_i \le Q_\mathrm{S}. \qquad (1)$$

As was noted above, the FBT scheme based on a coherent interference of the fields of driving electron bunches is used for obtaining maximum accelerating fields acting upon the witness bunch (Fig. 1a). At the same time, the maximum retarding field acting upon the last driving bunch also reaches the largest value. In order to decrease the maximum retarding field and simultaneously obtain the maximum accelerating field, we suggest a modified FBT (FBTM) scheme with the last driving bunch charged to $q_N = Q_\mathrm{m}$ and the charges of preceding driving bunches decreased in accordance with conditions (1). In this case, $E^+ = Q_\mathrm{m} a_{N,N+1} + \sum_{i=1}^{N-1} q_i a_{i,N+1}$ and the conditions imposed on the charges of driving electron bunches are given by the following inequalities:

$$\sum_{i=1}^{N-1} q_i a_{i,N} \le E_m^- - Q_\mathrm{m} a_0,$$

$$\sum_{i=1}^{N-1} q_i \le Q_\mathrm{S} - Q_\mathrm{m}.$$

The boundaries of applicability of the FBTM scheme of wakefield acceleration in a multibunch regime are determined by the conditions $a_0 Q_\mathrm{m} \le E_\mathrm{m}^- \le (a_0 + \sum_{i=1}^{N-1} a_{i,N}) Q_\mathrm{m}$.

In the aforementioned RBT scheme used to provide for the maximum energy transformer ratio, every next driving bunch is placed at the maximum of the electric field generated by the preceding bunches (rather than at the minimum of this field as in the FBT scheme), so as to ensure that all bunches will occur in the same retarding field (with allowance for the self-field). As a result, the total wakefield generated by the driving bunches increases as

$$E^+ = \sum_{\substack{i=1,\\ a_{i,N+1}>0}}^{N-1} q_i a_{i,N+1} - \sum_{\substack{i=1,\\ a_{i,N+1}<0}}^{N-1} q_i \left|a_{i,N+1}\right|. \qquad (2)$$

In order to further increase the accelerating field, we suggest a modified RBT (RBTM) scheme, in which the last bunch has $q_N = Q_\mathrm{m}$, the charges of preceding bunches entering into expression (2) with the plus sign are increased, and the charges of preceding bunches entering into expression (2) with the minus sign are decreased (beginning with the end of the train), so that the conditions (1) remain valid. In this case, the conditions imposed on the charges of driving electron bunches are given by the inequalities

$$\sum_{i=1}^{N-1} q_i \le Q_\mathrm{S} - Q_\mathrm{m},$$

$$\left| \sum_{\substack{i=1,\\ a_{i,N}>0}}^{K} q_i a_{i,N} - \sum_{\substack{i=1,\\ a_{i,N}<0}}^{K} q_i \left|a_{i,N}\right| \right| \le E_\mathrm{m}^-,$$

where $K = 1, 2, \ldots, N$.

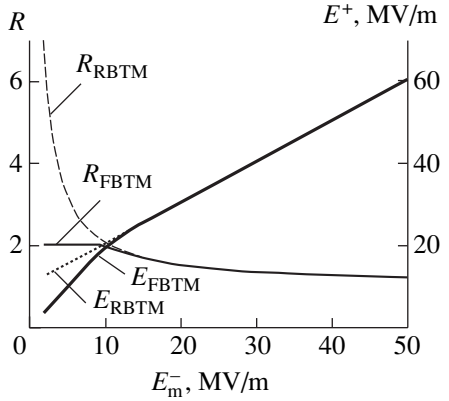

Fig. 2. The results of model calculations of the accelerating wakefield E^+ and the energy transformer ratio R as functions of the maximum retarding field E_m^- for the proposed FBTM and RBTM schemes.

Figure 2 shows the results of calculations of the accelerating wakefield and the energy transformer ratio for the FBTM and RBTM schemes with the optimum trains of four driving electron bunches as functions of the retarding field strength. The fundamental waveguide frequency was 13.625 GHz ($\lambda = 0.022$ m); the relative mean-square bunch length, $\sigma/\lambda = 0.15$; the starting energy of driving bunches, $W_\mathrm{d} = 150$ MeV; the maximum bunch charge, $Q_\mathrm{m} = 100$ nC; and the total

charge of the bunch train, $Q_S = NQ_m$. As can be seen from these data, the RBTM scheme is advantageous in cases of small retarding fields ($E_m^- < 15$ MV/m) and large accelerator lengths, while the FBTM scheme is expedient in cases of large retarding fields ($E_m^- > 35$ MV/m); in the region of intermediate fields (15 MV/m $< E_m^- <$ 35 MV/m), the two schemes are equally effective. In the limiting cases of minimum and maximum retarding fields, the results of our calculations coincide with those obtained using algorithms developed for the RBT and FBT schemes. It should be noted that the introduction of the limitation concerning the total train charge, $Q_S < NQ_m$, leads to an additional decrease in the accelerating field strength and the energy transformer ratio in the region of small Q_S.

Using several wakefield accelerator units possessing maximum field gradients and high energy transformer ratios, it is possible to reach the maximum possible values of the total energy increment for the particles accelerated for a given total acceleration pathlength.

Acknowledgments. This study was supported by the Ministry of Education of the Russian Federation and the Committee on Science and High School of St. Petersburg (project no. PD02-1.2-104) and by the US Department of Energy (SBIR grant no. DE-FG02-02ER83418).

REFERENCES

1. W. Gai, P. Schoessow, B. Cole, *et al.*, Phys. Rev. Lett. **61**, 2756 (1988).
2. W. Gai, in *Proceedings of the 11th Advanced Accelerator Concepts Workshop (AAC-2004), Long Island, 2004.*
3. W. Gai, A. D. Kanareykin, A. L. Kustov, and J. Simpson, Phys. Rev. E **55**, 3481 (1997).
4. J. Power, W. Gai, and P. Schoessow, Phys. Rev. E **60**, 6061 (1999).
5. J. G. Power, W. Gai, and A. Kanareykin, in *Proceedings of the 9th Advanced Accelerator Concepts Workshop (AAC-2000), Santa Fe, 2000*; http://gate.hep.anl.gov/awa/
6. K. Bane, T. Weiland, and P. Wilson, AIP Conf. Proc. **127**, 875 (1985).
7. K. L. Bane, P. Chen, and P. B. Wilson, IEEE Trans. Nucl. Sci. **32**, 3524 (1985).
8. E. M. Laziev, V. M. Tsakanov, and S. S. Vahanian, Preprint No. PhI-1040(3) (Yerevan Physics Institute, Yerevan, 1988).
9. S. S. Vaganyan, E. M. Laziev, and V. M. Tsakanov, Vopr. At. Nauki Tekh., Ser.: Yad. Fiz. Issled., No. 7, 15 (1990).
10. A. Kanareykin, W. Gai, J. G. Power, and P. Schoessow, in *Proceedings of the 11th Advanced Accelerator Concepts Workshop (AAC-2004), Long Island, 2004.*

Translated by P. Pozdeev

Technical Physics Letters, Vol. 31, No. 4, 2005, pp. 329–331. Translated from Pis'ma v Zhurnal Tekhnicheskoĭ Fiziki, Vol. 31, No. 8, 2005, pp. 32–37.

Effect of the Dynamic Redistribution of Impurities on the Grain-Boundary Friction in Nanocrystalline Materials

V. G. Kul'kov

Moscow Power Engineering University (Volzhskiĭ Branch), Volzhskiĭ, Volgograd oblast, Russia

e-mail: vfmei@viz.ru

Received November 18, 2004

Abstract—A relaxation process involving the redistribution of impurity atoms along the grain boundaries in a nanocrystalline material under the action of a variable external load is considered. The frequency spectrum of internal friction in this system, which is found by solving the barodiffusion equation, has a peak shape. The intensity of this spectral peak is estimated. © *2005 Pleiades Publishing, Inc.*

From the standpoint of mechanical spectroscopy, a specific feature of nanocrystalline materials is the much higher background level of internal friction as compared to that in the usual polycrystalline state [1]. This is related to the fact that a relatively large fraction of atoms in nanocrystalline substances occur in the grain-boundary phase. The mechanisms of oscillation damping in such materials are related to peculiarities of the grain-boundary slip, diffusion creep, and rotational deformation processes. The nanometer dimensions of grains may significantly enhance some effects, which are very weak and not practically manifested in polycrystalline samples with a relatively large grain size.

Let us consider a contribution to the internal friction that is related to diffusion jumps of an impurity adsorbed (segregated) at the grain boundaries in a nanocrystalline material. The material structure will be modeled by a periodic system of cubic grains with an edge length of R, occurring in close contact with each other. The x_0 coordinate axis is oriented along the diagonal of a cube face, and the z axis is directed along the cube edge perpendicular to this face (Fig. 1). Such simplified models are frequently used for the description of various properties of nanocrystalline materials [2, 3]. Let a variable shear stress $\sigma(t) = \sigma_0\exp[i(\omega t - \varphi)]$ act on the model crystal along the x_0 axis in the x_0z plane. As a result, normal compressive stresses $\sigma_n(t) = \pm\sigma(t)$ arise on the faces of grains making the angles $\pm\pi/4$ with the x_0 axis. These stresses violate the equilibrium and induce the diffusion flows of vacancies between adjacent regions of the grain boundaries. In what follows, we will ignore diffusion inward the grains, as well as the grain-boundary diffusion along the cubic faces perpendicular to the z axis. This approximation is acceptable, for example, when (i) real grains are elongated in the z axis direction, when (ii) a constant compressive stress acting along this direction exponentially decreases the grain-boundary diffusion coefficient [4], and when (iii) the corresponding grain boundaries are of a special type. With allowance for the system homogeneity in the z direction, the problem of diffusion on this single tilted grain boundary is one-dimensional relative to the x axis.

An excess (relative to equilibrium) concentration C of vacancies on a boundary segment under the action of the harmonic external load is described by the equation

$$\frac{\partial C(x,t)}{\partial t} = D_b\frac{\partial^2 C(x,t)}{\partial x^2} + A\exp(i\omega t), \qquad (1)$$

where D_b is the grain-boundary diffusion coefficient for the vacancies and A is the constant factor. The second term in the right-hand part of Eq. (1) describes a periodic source of vacancies. Note that the phase of this source differs by φ from the phase of the applied stress. A solution of this diffusion problem with zero bound-

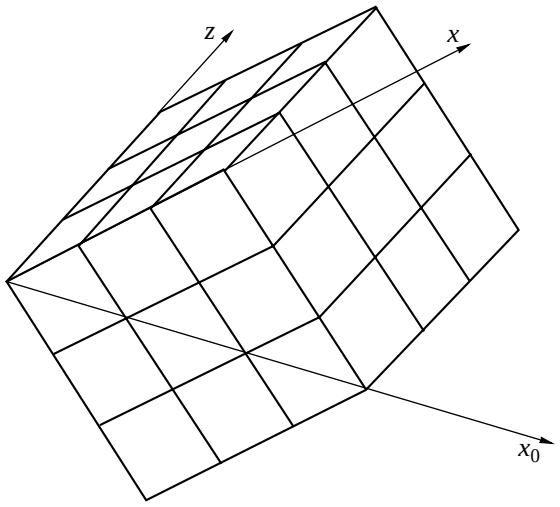

Fig. 1. Schematic diagram showing the model nanocrystalline structure and the orientation of axes.

1063-7850/05/3104-0329$26.00

ary conditions (determined by the symmetry) has been found using the method described in [5].

In the case of low values of the applied stress obeying the condition $\sigma_n\Omega/kT \ll 1$ (where Ω is the atomic volume), the excess density of vacancies is a linear function of the normal stress on the boundary segment. Under these conditions, the normal stress distribution on this segment is given by the expression

$$\sigma_n(x, t) = \frac{\pi\sigma_0}{2}\left(\sum_m \frac{\sin\frac{\pi m x}{R}}{m^4 + Z^2}\left(m\cos(\omega t) + \frac{Z}{m}\sin(\omega t)\right)\right) \times\left(\left(\sum_m \frac{1}{m^4 + Z^2}\right)^2 + \left(\sum_m \frac{Z}{m^2(m^4 + Z^2)}\right)^2\right)^{-1/2}, \quad (2)$$

where

$$Z = \frac{\omega R^2}{\pi^2 D_b}, \quad \tan\varphi_m = \frac{\omega R^2}{D_b\pi^2 m^2}, \quad m = 1, 3, 5, \ldots .$$

The impurity atoms are redistributed under the action of a periodic normal stress (2) developed on the inclined boundary segments. For these segments, the equation of barodiffusion can be written as follows [6]:

$$\frac{\partial C'(x, t)}{\partial t} = D'\frac{\partial^2 C'(x, t)}{\partial x^2} - D_1\frac{\partial\sigma_n(x, t)}{\partial x}\frac{\partial C'(x, t)}{\partial x} - D_1\frac{\partial^2\sigma_n(x, t)}{\partial^2 x}C'(x, t), \quad (3)$$

where $C'(x, t)$ is the concentration of impurity atoms at the boundary, D' is the grain-boundary diffusion coefficient for the impurity, $D_1 = D'\Omega/kT$ is the barodiffusion coefficient, and Ω is the partial volume (or volume per atom). Let us represent the impurity concentration as a sum of the equilibrium value and a variable part: $C'(x, t) = C'_e + C'_n(x, t)$. For a small applied stress (obeying the condition presented above), the variable part is small compared to the equilibrium part and, hence, we can ignore the second term on the right-hand side of Eq. (3) and put $C'(x, t) = C'_e$ in the third term. A solution of the modified Eq. (3) with zero boundary conditions for $C'_n(x, t)$ on the boundary segment yields

$$C'_n(x, t) = \frac{C'_e R^2\Omega\sigma_0\omega}{2\pi D_b kT}\sum_m\left[\frac{m}{\sqrt{m^4 + Z'^2}\sqrt{m^4 + Z^2}} \times\left(\left(\sum_m \frac{1}{m^4 + Z^2}\right)^2 + \left(\sum_m \frac{Z}{m^2(m^4 + Z^2)}\right)^2\right)^{-1/2} \times\exp(i(\omega t - \varphi_m - \psi_m))\sin\frac{\pi m x}{R}\right]; \quad Z' = \frac{\omega R^2}{\pi D'}. \quad (4)$$

The diffusion width of the boundary depends on the excess impurity concentration relative to that in the bulk of the grain. This excess value varies with the solid solution concentration as $\Delta\delta/\delta = \lambda C'_n/n_0$, where $\lambda = (n_0/a)(\partial a/\partial C')$ is a dimensional factor determined from the concentration dependence of the lattice parameter of the solution, and $n_0 = \Omega^{-1}$ is the number of atoms per unit volume of the matrix. The solution concentration C' is defined as the number of impurity atoms per unit volume. Differentiating the above expression with respect to time and taking into account relation (4), we obtain a formula for the velocity of the mutual displacement of grains along the x axis: $v = (\lambda\delta/3\sqrt{2}\,n_0)(\partial C'_n(x, t)/\partial t)$.

The energy loss for a single grain face is given by the expression

$$\Delta W_1 = R\int_0^{R}\int_0^{2\pi/\omega} \mathrm{Re}(\sigma(t))\mathrm{Re}(v(x, t))\,dx\,dt \quad (5)$$

and the maximum elastic energy stored in the grain volume R^3 is $W = R^3\sigma_0^2/2G$, where G is the shear modulus. The internal friction per grain, defined with allowance for the contribution from each face, is $Q_1^{-1} = \Delta W_1/2\pi W$. This eventually yields

$$Q^{-1} = \frac{\pi^3\lambda G\Omega^2\delta C'_e}{4\sqrt{2}RkT}\left(\left(\sum_m \frac{1}{m^4 + Z^2}\right)^2 \times\left(\sum_m \frac{Z}{m^2(m^2 + Z^2)}\right)^2\right)^{-1}\sum_m \frac{Z'}{(m^4 + Z'^2)(m^4 + Z^2)}. \quad (6)$$

Note that expression (6) describes only relaxation of the grain-boundary distribution of the impurity without a contribution of the background internal friction.

Figure 2 shows the frequency spectrum of the impurity-related internal friction $F(Z)$ (representing the terms in expression (6) dependent on Z, which is proportional to the frequency) for $Z' = Z$. Let us estimate the peak amplitude for the values of parameters typical of metals in the nanocrystalline state: $\delta/R = 0.02$; $C'_e/n_0 = C'_e\Omega = 0.01$; $G\Omega/kT_m = 50$ [4]; $T/T_m = 0.5$; $\lambda = 0.7$ [7]. Substituting these values into expression (6), we obtain $Q^{-1} \sim 4\times10^{-2}$. It should be noted that this is an upper estimate, while real values are lower because of smaller dimensional factors and grain-boundary shear moduli. Experimental observation of the peak of grain-boundary friction may encounter difficulties related to a very high level of the background internal friction [1]. A mechanism responsible for the appearance of this peak is analogous to the well-known Gorsky relaxation [8] related to the diffusion of impurity atoms in an inhomogeneously extended material. The

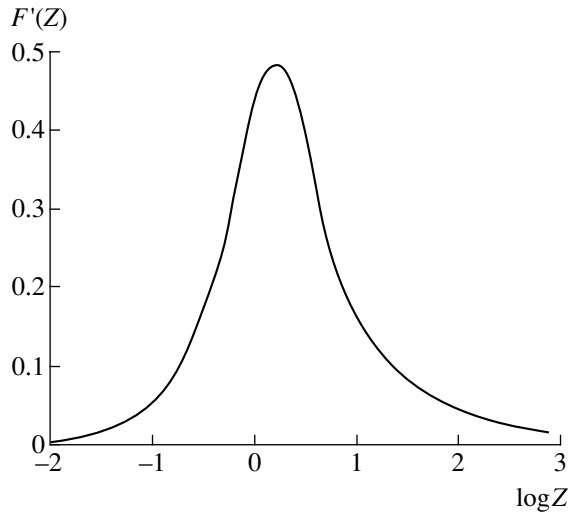

Fig. 2. The frequency spectrum of the impurity-related internal friction.

difference is that diffusion according to the Gorsky relaxation mechanism proceeds in the entire sample volume (involving distances on the order of the sample size), whereas in the proposed model, the diffusion process involves only the grain-boundary region (with a diffusion length being on the order of the grain size). This circumstance accounts for the much shorter relaxation time in the latter case.

REFERENCES

1. A. I. Gusev, Usp. Fiz. Nauk **168**, 55 (1998) [Phys. Usp. **41**, 49 (1998)].
2. M. Yu. Gutkin and I. A. Ovid'ko, Usp. Mekh. **2** (1), 68 (2003).
3. J. Wang, D. Wolf, S. R. Phillpot, and H. Gleiter, Nanostruct. Mater. **6**, 747 (1995).
4. V. N. Chuvil'deev, *Nonequilibrium Grain Boundaries in Metals: Theory and Application* (Fizmatlit, Moscow, 2004) [in Russian].
5. V. G. Kul'kov, in *Abstracts of the 24th Russia School on Science and Technology Problems, Yekaterinburg, 2004*, pp. 58–60.
6. V. A. Putilin and A. V. Kamashev, Pis'ma Zh. Tekh. Fiz. **23** (5), 84 (1997) [Tech. Phys. Lett. **23**, 205 (1997)].
7. *Method of Internal Friction in Physical Metallurgy: A Handbook*, Ed. by M. S. Blanter and Yu. V. Piguzov (Metallurgiya, Moscow, 1991) [in Russian].
8. A. S. Nowick and B. S. Berry, *Anelastic Relaxation in Crystalline Solids* (Academic Press, New York, 1972).

Translated by P. Pozdeev

Technical Physics Letters, Vol. 31, No. 4, 2005, pp. 332–335. Translated from Pis'ma v Zhurnal Tekhnicheskoĭ Fiziki, Vol. 31, No. 8, 2005, pp. 38–46.

Josephson Parameters of Bicrystal Junctions of a New Type Based on Metal Oxide Semiconductors

I. V. Borisenko, A. V. Shadrin, G. A. Ovsyannikov*, I. M. Kotelyanskii, and F. V. Komissinski

Institute of Radio Engineering and Electronics, Russian Academy of Sciences, Moscow, 125009 Russia
Chalmers University of Technology, 41296, Göteborg, Sweden
** e-mail: gena@hitech.cplire.ru*
Received September 7, 2004

Abstract—We have studied symmetric bicrystal Josephson junctions of a new type based on metal oxide superconductors in which the base planes are misoriented relative to the [100] direction by an angle within 22°–28°. These junctions exhibit record high values of the critical parameters at $T = 77$ K: the critical current density reaches $I_C = (2–5) \times 10^5$ A/cm^2 and the characteristic voltage is $V_C = I_C R_N = 0.6–0.9$ mV. The properties of the new junctions have been determined for the first time under the influence of monochromatic microwave radiation in the millimeter wavelength range and have been studied as functions of the magnetic field and temperature. The observed dependences of the critical current and the Shapiro step height on the electromagnetic field amplitude agree well with the theoretical predictions according to the resistive shunted junction model of the Josephson junction. The new junctions can be used in real superconducting devices operating at liquid nitrogen temperatures. © *2005 Pleiades Publishing, Inc.*

According to the existing theoretical models of the Josephson junction [1–4], the critical frequency f_C is related to the characteristic voltage $V_C = I_C R_N$ (I_C is the critical current and R_N is the normal resistance) by the Josephson formula $f_C = 2eV_C/h$ and is determined by the order parameter Δ of superconductors forming the junction. In the case of junctions based on metal oxide superconductors with high critical temperatures (T_C = 90 K) and the superconducting order parameter amplitude $\Delta_0/e \approx 20$ mV, the V_C value must already be on the order of several millivolts at liquid nitrogen temperature. In practice, the maximum characteristic voltages up to $V_C \approx 300$ μV were obtained using the bicrystal Josephson junctions on $SrTiO_3$ substrates [5].[1]

Recently, it was reported [7, 8] that a special modification of the topology of bicrystal substrates used for the deposition of metal oxide superconductor films allows the V_C to be increased to about 1 mV. However, no evidence was presented in [7, 8] to confirm that the observed dc parameters (I_C, R_N) are consistent with the dynamic (microwave) characteristics of the junctions. Such data are necessary, since a small coherence length ($\xi_0 \approx 2$ nm) in the base plane of metal oxide superconductors results in that a superconducting current passing through shorted paths with the lengths above ξ_0 does not produce the ac Josephson effect [9, 10]. As a result, the high V_C values obtained from the results of I_C and R_N measurements may not correspond to the dynamic characteristics of the junctions, such as the Josephson generation amplitude, phase dependence of the critical current, and microwave impedance.[2]

This Letter reports on the results of investigations into the dc and dynamic (microwave) parameters of junctions grown on substrates made of neodymium gallate ($NdGaO_3$), a material characterized by low dielectric losses in the millimeter wavelength range.

The samples were prepared on bicrystal substrates with a topology different from the standard variant, according to which the base planes are misoriented by rotation relative to the [001] direction in the metal oxide superconductor crystal structure (rotational or planar bicrystal junctions, PBJs). Our bicrystal substrates were manufactured so that the base planes would make an angle with the [100] direction (tilted bicrystal junctions, TBJs). The orientations of the axes of metal oxide superconductor crystal structures of the PBJ and TBJ types are shown in Fig. 1. As is known, misorientation of the crystallographic axes of the junction components by the angles α and β relative to the interface normal (in PBJ) or the substrate normal (in TBJ) determines the electric parameters of such junctions [7–10]. A distinctive feature of the TBJ in comparison to the PBJ is relatively weak faceting of the

[1] The values of $V_C \approx 300$ μV were also observed on shunted tunnel niobium junctions at liquid helium temperatures ($T = 4.2$ K) [6].

[2] The V_C values obtained from dc measurements were higher than the values observed in the dynamic regime for the Josephson junctions on the substrate step and the edge junctions [9, 10].

1063-7850/05/3104-0332$26.00 © 2005 Pleiades Publishing, Inc.

metal oxide superconductor film near the bicrystal boundary [7, 8].

The junctions were manufactured on $NdGaO_3$ (NGO) bicrystal substrates. The base plane was (110)NGO, on which (001)-oriented $YBa_2Cu_3O_x$ (YBCO) films can be grown. The conditions of epitaxial growth in the [100]YBCO//[001]NGO system are retained for small tilts of the (110)NGO plane relative to the substrate normal [13].[3] The misorientations of the junction components were $\alpha = \beta = 11°$ and 14° (symmetric TBJs). The epitaxial YBCO films with a thickness of 150 nm were deposited by means of the dc cathode sputtering of a stoichiometric YBCO target in oxygen at a high pressure (3 mbar). The films were deposited onto substrates heated to 780–800°C and then cooled to room temperature for 1.5 h in the oxygen atmosphere. The obtained heteroepitaxial YBCO films had critical temperatures within T_C = 87–89 K.[4] The Josephson bridges across the bicrystal boundary had a width of 4 μm and a length of 10 μm and were formed by high-frequency plasma etching in argon, followed by chemical etching in a 0.5% bromine solution in ethanol [12, 13].

The current–voltage (I–V) curves were measured at various temperatures in a range from 4.2 to 77 K. The measurements were performed in the absence of magnetic field, in a field of up to H = 100 Oe, and on the samples exposed to a monochromatic electromagnetic radiation with a frequency f_e from 30 to 100 GHz. In order to decrease the influence of uncontrolled external fields, the investigation was performed in a screened room, with filtration of the signals in all leads connected to a sample.

The samples of bicrystal Josephson junctions had critical current densities $j_C = (2–5) \times 10^5$ A/cm^2 and characteristic voltages $V_C = I_C R_N$ = 0.6–0.9 mV at T = 77 K. The results of the determination of electric parameters of the Josephson junctions are summarized in the table. As can be seen from these data, the PBJ samples exhibit significantly lower critical characteristics (I_C and V_C at T = 77 K) as compared to the TBJ samples with the same cross section areas. The barrier transparency evaluated for TBJs from the value of $R_N S = (3–7) \times 10^{-9}$ Ω cm^2 [14] (which is close to that for PBJ [13]) and averaged over the momentum directions and junction areas was $D \approx 10^{-1}$.

Figure 2 shows the typical I–V curve of a TBJ sample. The curve corresponds to the hyperbolic law characteristic of a resistive shunted junction model of the Josephson junction, with two channels of the charge transfer: via the current of quasiparticles (V/R_N) and the superconducting current $I_S(\varphi) = I_C \sin\varphi$ [1, 15]. A large (up to 50% of I_C) excess current (deviation from the Ohm law) observed at voltages above 3 mV was indicative of the presence of an additional channel for the forward (nontunneling) charge transfer. The temperature dependence of the critical current (see the left inset in Fig. 2) is close to linear, in contrast to the theoretical dependence for the tunneling junctions based on the s-wave superconductors (SIS junctions) [1], which exhibits saturation at $T < 0.5T_C$. In the process of current transfer in the SIS junctions, an important role is played by Andreev states with the energies ε on the

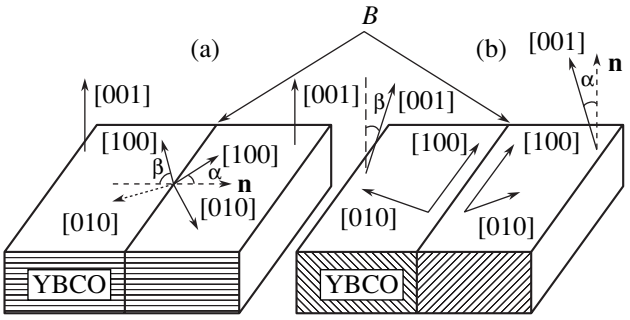

Fig. 1. Schematic diagram showing the bicrystal Josephson junctions of two types: (a) rotational or planar bicrystal junction (PBJ); (b) tilted bicrystal junction (TBJ); B is the bicrystal boundary; dashed lines show the interface normal (PBJ) and the substrate normal (TBJ) directions; cross-hatching indicates the orientation of the metal oxide superconductor layers.

Electric parameters of PBJ and TBJ samples at liquid nitrogen temperature (T = 77 K)

Junction type	α + β (α = β)	Sample no.	I_C, μA	R_N, Ω	V_C, μV
PBJ	24°	J2	70	1.1	77
		J4	140	0.64	90
		J5	200	0.17	34
PBJ	28°	J2	10	3.0	30
		J2	21	3.7	78
		J4	24	3.5	84
		J5	24	3.2	77
TBJ	22°	J1	1250	0.54	675
		J2	1210	0.54	653
		J3	2100	0.43	903
		J4	1300	0.56	728
TBJ	28°	J1	30	6.7	201
		J2	72	3.0	216
		J3	75	4.5	337
		J4	63	4.1	258

[3] Because of a small difference in the crystal lattice parameters along the a and b axes, the epitaxial YBCO films exhibit alternation of the [100] and [010] directions. For certainty, we indicate below only the [100]YBCO direction.

[4] The parameters of YBCO films were substantially similar when the epitaxial layers were grown by laser ablation.

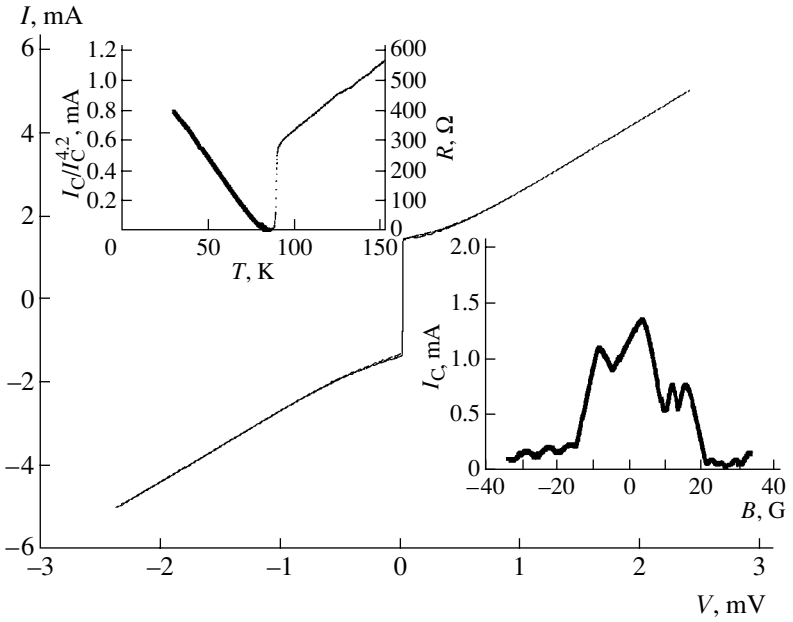

Fig. 2. Typical *I–V* curves of the tilted bicrystal junction (T = 77 K). The insets show the temperature dependence (left) and the magnetic field (T= 77 K) dependence (right) of the critical current.

order of Δ (high-energy Andreev states). In the junctions with direct conductivity, where the superconducting current transfer is determined by low-energy Andreev states ($\varepsilon \ll \Delta$), the $I_C(T)$ function is close to linear in a broad temperature range [1]. In PBJs formed by superconductors with a predominating order parameter of the *d*-wave type (DID junctions) [2–4], both types of Andreev states are involved in the current transfer, their contributions being dependent on the incidence angle of quasi-particle [2–4, 16]. In contrast, the low-energy states are not formed for the orientation of crystallographic axes typical of the TBJs, where one axis in the base plane of the metal oxide superconductor is parallel to the interface normal [2–4, 16].

The difference between the mechanisms of current transfer in PBJs and TBJs is also substantially manifested in the angular dependence of the critical parameters of the bicrystal Josephson junctions. For PBJs, the characteristic voltage V_C exhibits rather weak variation in a large interval of angles up to ±33°, although the normal resistance may exhibit a tenfold increase (see table [8]). It should be noted that, for a misorientation of ±45°, the j_C value significantly decreases and V_C exhibits a tenfold drop to reach 0.5 mV at helium temperatures [17]. For TBJs, the experiments revealed a much stronger angular dependence of V_C, which decreased by a factor of 3 when the misorientation angle was increased by only 6° (see table). This behavior well agrees with the theory [11], which takes into account both the large ratio of the superconducting gap width to the Fermi energy (Δ/E_F) characteristic of metal oxide superconductors and the large anisotropy of the Fermi surface. In the presence of these factors, the quasi-momenta of the incident electron and reflected hole diverge by a certain angle in the course of the Andreev reflection at the intersection of tilted planes. This leads to a violation of the coherence of multiple Andreev reflections and, eventually, to a decrease in the superconducting current. There must be a certain critical misorientation angle at which the critical current rapidly drops to zero, although this sharp variation can be smeared by inhomogeneity of the interface. For the junctions with small misorientation angles ($\alpha + \beta < 13°$), the shape of the observed *I–V* curves differs from hyperbolic and is typical of a viscous flow of the vortex flux [1, 8].

The right inset in Fig. 2 shows the behavior of the critical current as a function of the magnetic field. As can be seen, the $I_C(B)$ function exhibits a maximum at $B = 0$. However, the $I_C(B)$ curve significantly differs from the Fraunhofer profile and is asymmetric, which is typical of the distributed Josephson junctions [1, 15]. Indeed, the Josephson magnetic field penetration depth for $j_C = 3 \times 10^5$ A/cm^2 ($\lambda_J = 0.5$ μm) is significantly smaller than the junction width (4 μm). Thus, our junctions can be considered as distributed already at liquid nitrogen temperature.

In order to determine the difference between the dynamic parameters and the dc characteristics, we have studied the *I–V* curves for a monochromatic microwave radiation $A\sin(2\pi f_e t)$ in the millimeter wavelength range (f_e = 56 GHz). The behavior of the critical current and the Shapiro steps on the electromagnetic wave amplitude well agreed with the theoretical dependences determined for a resistive shunted junction model of the Josephson junction (Fig. 3). The difference between the

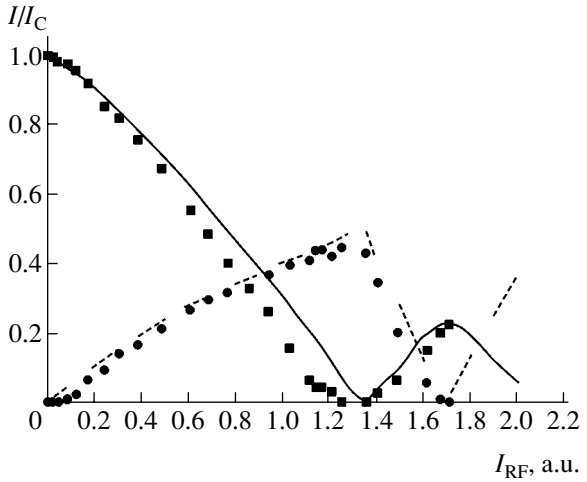

Fig. 3. Experimental plots of the critical current (squares) and the first Shapiro step (circles) versus microwave signal amplitude (at f_e = 56 GHz). Curves show the corresponding theoretical dependences calculated for f_e/f_C = 0.22, $f_C = 2eI_CR_N/h$, and the I_C and R_N values determined by dc measurements.

experimental value of the maximum normalized first step ($(I_1/I_C)_{max}$ = 0.46) and the theoretical value ($(I_1/I_C)_{max}$ = 0.43) at a normalized frequency of f_e/f_C = 0.23 was about 7%. The fact that the experimental value is higher than the theoretical one indicates that the effective critical current may decrease by 7% as a result of the inhomogeneous current distribution. It should be noted that the absence of subharmonic Shapiro steps (at $V = hf_e/2en$) and the zero minimum values of $I_C(P_e)$ and $I_1(P_e)$ are indicative of the purely sinusoidal character (the absence of higher $\sin(n\varphi)$ harmonics) of the dependence of the superconducting current on the phase difference [18].

At lower (helium) temperatures, the excess current exhibits growth, although the junctions have very high values of the characteristic voltage V_C (up to 16 mV). However, the use of such junctions in practical systems is hindered by the significant deviation of their behavior from that according to the resistive shunted junction model. Thus, despite the presence of the excess current, the *I–V* curves show a good correspondence between the dynamic (Josephson) and dc parameters of the TBJ samples at liquid nitrogen temperature (77 K). The high characteristic voltage (V_C > 0.6 mV) observed in more than 70% of the samples studied suggests that these junctions are very promising elements for both high- and low-frequency superconducting electronics.

Acknowledgments. The authors are grateful to A. Golubov, Yu.V. Kislinskiĭ, K.I. Constantinian, V.K. Kornev, and M.I. Faleĭ for their help in experiment and fruitful discussions.

This study was supported in part by the International Scientific-Technological Center (grant no. 2369), the European Community INTAS Program Foundation (grant nos. 01-0809 and 01-0249), the Russian Foundation for Basic Research (project no. 04-02-16818a), and the Presidential Program of Support for Leading Scientific Schools in Russia (project no. NSh-1344.2003.2).

REFERENCES

1. K. K. Likharev, Rev. Mod. Phys. **51**, 101 (1979).
2. R. A. Riedel and P. F. Bagwell, Phys. Rev. B **57**, 6084 (1998).
3. Yu. S. Barash, Phys. Rev. B **61**, 678 (2000).
4. Y. Tanaka and S. Kashiwaya, Phys. Rev. B **53**, R11957 (1996).
5. L. R. Vale, R. H. Ono, and D. A. Rudman, IEEE Trans. Appl. Supercond. **7**, 3193 (1997).
6. P. Koshelets and S. V. Shitov, Supercond. Sci. Technol. **13**, R53 (2000).
7. U. Pope, Y. Y. Divin, M. I. Faley, *et al.*, IEEE Trans. Appl. Supercond. **11**, 3768 (2001).
8. Y. Y. Divin, I. M. Kotelyanskii, P. M. Shadrin, *et al.*, in *Abstracts of the 6th European Conference on Applied Superconductivity, Sorrento, 2003*, p. 166.
9. A. D. Mashtakov, G. A. Ovsyannikov, I. V. Borisenko, *et al.*, IEEE Trans. Appl. Supercond. **9**, 3001 (1999).
10. H. Hilgenkamp and J. Mannhart, Rev. Mod. Phys. **74**, 485 (2002).
11. A. Golubov and F. Tafuri, Phys. Rev. B **62**, 15200 (2000).
12. I. K. Bdikin, P. B. Mozhaev, G. A. Ovsyannikov, *et al.*, Fiz. Tverd. Tela (St. Petersburg) **43**, 1548 (2001) [Phys. Solid State **43**, 1611 (2001)].
13. A. D. Mashtakov, K. I. Constantinian, G. A. Ovsyannikov, and E. A. Stepantsov, Pis'ma Zh. Tekh. Fiz. **25** (7), 1 (1999) [Tech. Phys. Lett. **25**, 249 (1999)].
14. F. V. Komissinskii, G. A. Ovsyannikov, and Z. G. Ivanov, Fiz. Tverd. Tela (St. Petersburg) **43**, 769 (2001) [Phys. Solid State **43**, 801 (2001)].
15. K. K. Likharev and B. T. Ulrich, *Systems with Josephson Junctions: Basic Theory* (Mosk. Univ., Moscow, 1978) [in Russian].
16. I. V. Borisenko, K. I. Constantinian, Yu. V. Kislinskii, and G. A. Ovsyannikov, Zh. Éksp. Teor. Fiz. **126**, 1402 (2004) [JETP **99**, 1223 (2004)].
17. F. Tafuri *et al.*, Supercond. Sci. Technol. **12**, 1007 (1999).
18. G. A. Ovsyannikov, I. V. Borisenko, K. I. Constantinian, *et al.*, Pis'ma Zh. Tekh. Fiz. **25** (11), 65 (1999) [Tech. Phys. Lett. **25**, 913 (1999)].

Translated by P. Pozdeev

Technical Physics Letters, Vol. 31, No. 4, 2005, pp. 336–338. Translated from Pis'ma v Zhurnal Tekhnicheskoĭ Fiziki, Vol. 31, No. 8, 2005, pp. 47–51.

Luminescence Intensity Monitoring in a MOS Tunnel Structure with Inhomogeneous Thickness of the Insulator

S. E. Tyaginov[a], N. Asli[b], M. I. Vexler[a], A. F. Shulekin[a,*], P. Seegebrecht[b], and I. V. Grekhov[a]

[a] *Ioffe Physicotechnical Institute, Russian Academy of Sciences, St. Petersburg, 194021 Russia*
[b] *Lehrstuhl für Halbleitertechnik, Technische Fakultät der Universität Kiel, D-24143 Kiel, Germany*
** e-mail: shulekin@pop.ioffe.ru*

Received December 2, 2004

Abstract—The electroluminescence (EL) time series in a metal–oxide–semiconductor tunnel structure of the Al/SiO_2/*p*-Si type have been measured. It is demonstrated that analysis of the EL curves in some cases provides more correct information about the state of the oxide layer as compared to that obtained from the results of electric current monitoring. © *2005 Pleiades Publishing, Inc.*

Metal–oxide–semiconductor (MOS) structures, including those with a tunnel-thin (2- to 3-nm-thick) SiO_2 layer, are conventionally tested by method of dc stress at a constant current J or a constant applied voltage V, whereby the response signal is measured in the form of $V(t)$ or $J(t)$, respectively [1, 2]. An analysis of these time series allows the process of oxide degradation to be studied in detail and, in particular, the soft breakdown events to be detected [2].

However, the purely electric diagnostics of soft breakdown in MOS structures can be somewhat complicated when the applied voltage V is relatively large. Indeed, it was demonstrated [3] that the current measured upon breakdown always increases only in the case of sufficiently small voltages ($V \sim 1$ V). In contrast, the current observed at $V \sim 2$–4 V may exhibit a change toward both increase and decrease, since the resistance of damaged regions formed under such conditions can be either lower or higher than the tunnel resistance of the same regions in the initial state. The nontrivial effect, whereby the current J decreases, is more pronounced in the presence of significant variance of the SiO_2 layer thickness [3] because the offset of the charge transfer in the thinnest regions is manifested in the total current. If we assume that several soft breakdown events may take place simultaneously, the local current decay in one site can, in principle, be compensated in another place so that the $J(t)$ measurements will provide no reliable information about the state of the MOS structure tested.

In this context, it may be of interest to use monitoring of the luminescence intensity in MOS tunnel structures as a means of additional diagnostics with respect to soft breakdown, since a sufficiently intense electroluminescence (EL) in MOS diodes with 20–30 Å thick oxide is observed precisely in the interval of applied voltages $V \sim 3$ V (with plus on the substrate) [4, 5]. This luminescence is related to the relaxation of hot electrons injected into silicon (see the energy diagram in the inset to Fig. 1). The emission spectrum is rather broad and exhibits a short-wavelength edge at $\hbar\omega = E + E_g$, where E is the energy acquired by electrons upon injection and E_g is the bandgap width [5]. The shape of the EL spectra observed in undamaged MOS structures is independent of the SiO_2 layer thickness, and the quantum yield $dP_{le}(E, \hbar\omega)/d[\hbar\omega]$ (defined as the number of

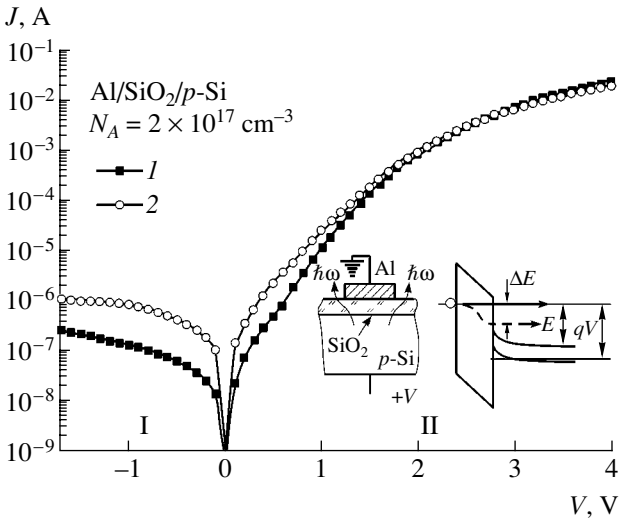

Fig. 1. The typical current-voltage characteristics of (*1*) fresh and (*2*) damaged MOS tunnel structure of the Al/SiO_2/*p*-Si type, in which the oxide breakdown led to vanishing of the visible luminescence from the sample ($E \sim qV - E_g$ prior to breakdown). The inset shows the structure and the energy band diagram of the MOS diode sample. Regions I and II correspond to the deep depletion and accumulation regimes, respectively.

1063-7850/05/3104-0336$26.00 © 2005 Pleiades Publishing, Inc.

photons in the energy interval $\hbar\omega \ldots \hbar\omega + \delta[\hbar\omega]$ generated by one hot electron) increases with the energy E [5]. Breakdown in the oxide leads to a decrease in the energy of electrons injected in the damaged region (see the inset to Fig. 1). Therefore, the intensity of photon emission at any given energy $\hbar\omega$ normalized to the current, $I^{\hbar\omega}/J$, will decrease upon breakdown of the MOS structure.

Thus, by monitoring $I^{\hbar\omega}(t)$ at a constant bias voltage V, it is possible to detect soft breakdown events as manifested by sharp drops in the $I^{\hbar\omega}/J$ ratio. In this approach, the time series of the EL intensity, $I^{\hbar\omega}(t)$, is analogous to the current time series in the traditional approach. The EL measurements should be performed in the spectral range $E_g \ll \hbar\omega < E + E_g$. However, it should be noted that even strongly damaged regions may contribute to the emission at $\hbar\omega \sim E_g = 1.12$ eV, so that it is expedient to select $\hbar\omega$ closer to the short-wavelength edge.

In order to verify the proposed method based on the LE intensity monitoring, we have studied the samples of MOS tunnel diodes of the $Al/SiO_2/p$-Si type (see the inset to Fig. 1) with a nominal oxide layer thickness of 25 Å and an rms deviation $\sigma_d \sim 3$–4 Å. According to modern technology standards [6], this degree of oxide thickness inhomogeneity is considered large, but the diode samples showed satisfactory and reproducible electrical characteristics (Fig. 1). Since round aluminum contacts (with an area of 10^{-3} cm^2) were nontransparent, the emitted light was collected from a peripheral region of the structure. The EL intensity $I^{\hbar\omega}$ was monitored using the highly sensitive setup described in [7], which is specially designed for the measurement of emission spectra of MOS structures.

It should be noted that the visible EL from the samples of MOS diodes rather frequently vanished upon overloading. At the same time, the I–V curves exhibited no radical changes; in particular, they retained the asymmetry between the forward and reverse branches (Fig. 1). This observation provides evidence for the above assumption that the EL intensity may be more sensitive than the current with respect to the state of the MOS structure.

Figure 2 shows a typical example of the EL intensity monitored at $\lambda = 620$ nm ($\hbar\omega = 2.00$ eV) and presents the corresponding plot of $I^{\hbar\omega}(t)/J(t)$. As can be seen, the $I^{\hbar\omega}$ curve exhibits both smooth and sharp variations with time. Smooth changes reflect an increase in the tunneling current related to the generation and recharge of the surface states, which is especially clearly manifested immediately upon bias voltage application to the sample. Note that these LE intensity variations are quantitatively more pronounced than variations in the current (the $I^{\hbar\omega}/J$ ratio increases). This behavior is related to the fact that a change in the current upon degradation of the oxide takes place more rapidly at the periphery (from which the response signal is taken) than on the average over the entire sample.

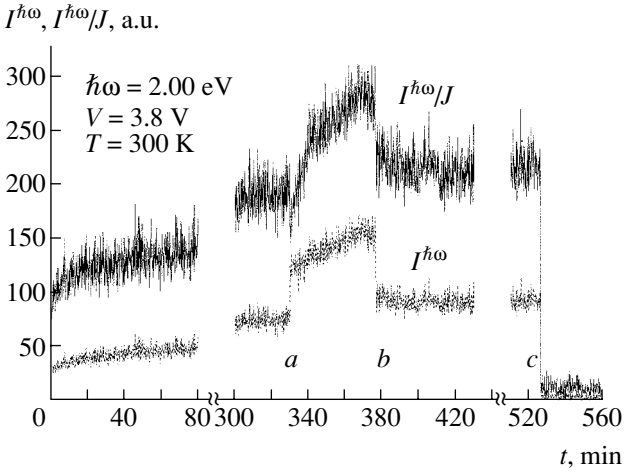

Fig. 2. The most informative fragments of experimental time series of the EL intensity $I^{\hbar\omega}(t)$ and the $I^{\hbar\omega}(t)/J(t)$ ratio for an MOS tunnel structure of the $Al/SiO_2/p$-Si type. Points a–c correspond to soft breakdown events (the current J exhibited growth at point a, drop at point b, and an increase within several percents at point c).

The jumplike changes in the EL intensity, which are also clearly seen in Fig. 2, are probably related to the oxide breakdown events. Note that the $I^{\hbar\omega}$ curve exhibits both upward and downward jumps, while the $I^{\hbar\omega}(t)/J(t)$ ratio always drops down irrespective of the direction of current variation caused by the breakdown: upward (such as at point a in Fig. 2) or downward (point b in Fig. 2). The drop at point a is somewhat masked by the subsequent smooth increase. Point c in Fig. 2 corresponds to the aforementioned event, whereby the EL almost completely vanishes. Analogous results were obtained when the EL monitoring was performed closer to the short-wavelength edge of the spectrum ($\hbar\omega = 3.02$ eV), but the measurements were complicated because of a lower emission intensity.

To summarize, we proposed and verified a method for monitoring the state of the oxide layer in MOS tunnel structures based on the measurement of time series of the EL intensity along with the current time series. It was demonstrated that the EL intensity curves are not less informative than the current time series measured according to the traditional method. The proposed technique may be of interest for oxide state monitoring at relatively high bias voltages in MOS structures with inhomogeneous thickness of the insulating layer.

Acknowledgments. The authors gratefully acknowledge financial support from the Program "Physics and Technology of Low-Dimensional Structures," the Presidential Program of Support for Leading Scientific

Schools in Russia (project no. NSh-758.2003.2), the Soros Foundation, and the Russian Science Support Foundation.

REFERENCES

1. R. Degraeve, in *Proceedings of the 9th European Symposium on Reliability of Electron Devices, Failure Physics and Analysis, Leuven, 1998.*
2. M. Houssa, N. Vandewalle, T. Nigam, *et al.*, Tech. Dig. Int. Electron Devices Meet., 909 (1998).
3. A. F. Shulekin, S. E. Tyaginov, R. Khlil, *et al.*, Fiz. Tekh. Poluprovodn. (St. Petersburg) **38**, 753 (2004) [Semiconductors **38**, 724 (2004)].
4. E. Cartier, J. C. Tsang, M. V. Fischetti, and D. A. Buchanan, Microelectron. Eng. **36**, 106 (1997).
5. N. Asli, M. I. Vexler, A. F. Shulekin, and P. Seegebrecht, Semicond. Sci. Technol. **18**, 147 (2003).
6. H. S. Momose, S. Nakamura, T. Ohguro, *et al.*, IEEE Trans. Electron Devices **45**, 691 (1998).
7. N. Asli, PhD Thesis (Kiel Univ., Kiel, 2004).

Translated by P. Pozdeev

Technical Physics Letters, Vol. 31, No. 4, 2005, pp. 339–340. Translated from Pis'ma v Zhurnal Tekhnicheskoĭ Fiziki, Vol. 31, No. 8, 2005, pp. 52–56.

Current–Voltage Characteristics of Thin-Film Gas Sensor Structures Based on Tin Dioxide

V. V. Simakov, O. V. Yakusheva, A. I. Grebennikov, and V. V. Kisin*

Saratov State Technical University, Saratov, Russia
"Synthesis" Company, Saratov, Russia
** e-mail: kisin@sstu.ru*

Received November 25, 2004

Abstract—The experimental current–voltage (*I–U*) curves of thin-film structures based on tin dioxide (SnO_2) exhibit nonlinearity in the range of strong applied electric fields. The results of *I–U* measurements are interpreted within the framework of a model that assumes the drift of adsorbed ions over the film surface. The observed phenomenon can be used both for detecting the impurities in air and for recognizing the types of adsorbed species. © *2005 Pleiades Publishing, Inc.*

The phenomenon of adsorption-induced variation in the resistance of thin films of metal oxides is widely used in gas sensors [1, 2]. The miniaturization of such gas sensors leads to an increase in the field strength between electrodes, which stimulates the migration of adsorbed gas species over the surface of the active layer and influences the performance characteristics of the gas sensor [3–5].

This Letter presents the results of investigations of the current–voltage characteristics (*I–U* curves) of the gas sensor structures based on thin films of tin dioxide (SnO_2) exposed to gaseous media of various compositions.

The sample structures were formed on polycrystalline sapphire (Polycor) substrates with platinum electrodes preliminarily deposited via a mask onto the front side. The interelectrode gaps were 50 μm wide. Four heating elements and two thermoresistors were deposited in a similar technological cycle on the rear side of the substrate [6]. A tin dioxide film was deposited above the electrodes by RF magnetron sputtering of an SnO_2/CuO target in an Ar–O_2 atmosphere [7]. The resistance of the film decreased in the presence of reducing gases in the atmosphere [8].

The oxide film thickness was ~1 μm, as measured by an SE-400 15/42 ellipsometer (Sentech Instruments GmbH, Germany). The heaters and thermoresistors were calibrated with the aid of an IR camera of the TH 3100MR type (NEC Instruments Ltd., Japan) and allowed the film temperature to be maintained at 300°C over the entire area with a lateral inhomogeneity not exceeding 5%.

The *I–U* curves were measured using a Keithley Model 2001 digital multimeter (Keithley Instruments Inc., USA) and a Grundig Model PN-300 power supply unit (Grundig Professional Electronic GmbH, Germany) in a range of bias voltages from 0 to 30 V. The measurements were performed in a synthetic air (20.5% O_2 in N_2; Messer Griesheim GmbH, Germany) and in model gas mixtures containing CO or isopropanol (C_3H_7OH) vapor. The gas phase humidity was monitored by a Testo Model 615 hygrometer (Testo AG, Germany) and controlled on a 50% level in all experiments.

Figure 1 shows the typical current–voltage characteristics of the sample structures measured in the model gas mixtures. The *I–U* curves were virtually linear in the range of low bias voltages ($U < 5$ V) and were sublinear at higher applied voltages ($U > 5$ V). On a double logarithmic scale, the experimental data could be approximated by two straight segments corresponding to power functions of the type $I = AU^n$, where I is the current, A is a constant factor, U is the bias voltage, and n is the exponent. The A and n values were different in the low- and high-bias ranges.

Figure 2 presents the plots of n versus impurity concentration in the model gas mixture. In the range of low bias voltages, the n value was about unity and it was virtually independent of the type and concentration of impurities. In the range of $U > 5$ V (or the field strengths above 10^3 V/cm), the n value was substantially dependent on the type of reducing species, while the dependence on their concentration was much less pronounced. This feature of the sensor characteristic can be used for recognizing the types of impurities in the gas phase.

The value of the coefficient A in the range of low bias voltages is approximately inversely proportional to the sample resistance: as the impurity concentration in the gas phase increases, the sample resistance decreases (Fig. 1). This behavior is usually employed for determining the impurity content in air [9].

The observed features of the *I–U* curves can be explained by assuming that oxygen species adsorbed on the SnO_2 film surface exhibit charging by capturing

1063-7850/05/3104-0339$26.00 © 2005 Pleiades Publishing, Inc.

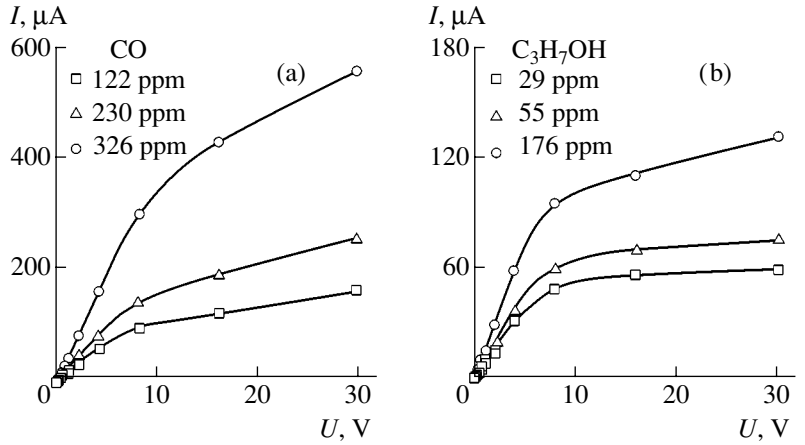

Fig. 1. The typical current–voltage characteristics of the SnO_2 based thin-film gas sensor structures exposed to synthetic air containing various amounts of (a) CO and (b) C_3H_7OH vapor.

electrons from the volume of the film and then drift toward the anode under the action of an applied external field. Reaching the anode, the charged species give electrons back to the film or to the metal contact and exhibit desorption. If the drift time for the adsorbed species moving from the cathode to the anode is shorter than their lifetime on the surface (as in the range of high bias voltages), the adsorbed species accumulate at the anode and induce depletion in this near-electrode region. The current to the anode is mostly transferred by the charges localized on the adsorbed species and by the free carriers generated as a result of desorption of these species. Since the mobility of adsorbed species is lower than that of the free charge carriers and/or the desorption current is relatively weak, a high-ohmic region is formed in the thin-film structure. As a result, the differential resistance of this structure at high bias voltages is lower than that at small voltages.

In conclusion, we have established that experimental *I–U* curves of thin-film structures based on tin dioxide exhibit nonlinearity in the range of strong applied electric fields. The experimental data are interpreted within the framework of a model that assumes the effective drift of adsorbed ions over the film surface under the action of an applied field. The observed phenomenon can be used both for detecting the reducing impurities in air and for recognizing the types of adsorbed species.

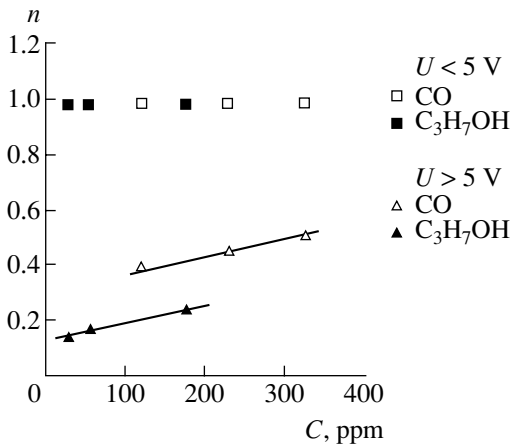

Fig. 2. The plots of n (in $I = AU^n$ relation) versus impurity concentration in synthetic air probed by SnO_2 based thin-film gas sensor.

Acknowledgments. The authors are grateful to Dr. J. Goschnick and Dr. I. Kiselev (Institut für Instrumentelle Analytik, Karlsruhe, Germany) for their help and fruitful cooperation.

This study was supported by the Ministry of Education of the Russian Federation (project nos. PD02-2.7-42) and the Foundation for Assistance to Small Innovative Enterprises (contract no. 2539p/4926). One of the authors (V.V.S.) gratefully acknowledges the support via grant from DAAD (Germany).

REFERENCES

1. K. D. Schierbaum, J. Geiger, U. Weimar, and W. Göpel, Sens. Actuators B **13**, 143 (1993).
2. J. H. W. de Wit, J. Solid State Chem. **8**, 142 (1973).
3. M. Liess, Thin Solid Films **410**, 183 (2002).
4. C. Nayral, E. Viala, V. Colliere, *et al.*, Appl. Surf. Sci. **164**, 219 (2000).
5. C. Cane, I. Gracia, A. Gotz, *et al.*, Sens. Actuators B **65**, 244 (2000).
6. S. Ehrmann, J. Jungst, and J. Goschnik, Sens. Actuators B **66**, 43 (2000).
7. V. V. Kissine, S. A. Voroshilov, and V. V. Sysoev, Thin Solid Films **348**, 304 (1999).
8. V. V. Sysoev, N. I. Kucherenko, and V. V. Kisin, Pis'ma Zh. Tekh. Fiz. **30** (18), 14 (2004) [Tech. Phys. Lett. **30**, 759 (2004)].
9. *Handbook of Machine Olfaction: Electronic Nose Technology*, Ed. by T. Pearce, S. Schiffman, T. Nagle, and J. Gardner (Wiley–VCH, Weinheim, 2003).

Translated by P. Pozdeev

Technical Physics Letters, Vol. 31, No. 4, 2005, pp. 341–342. Translated from Pis'ma v Zhurnal Tekhnicheskoĭ Fiziki, Vol. 31, No. 8, 2005, pp. 57–61.

Polyimide Membranes Formed on a Metal Grid Matrix by the Langmuir–Blodgett Method

V. V. Luchinin*, S. I. Goloudina, V. M. Pasyuta, M. F. Panov, I. V. Gofman, V. P. Sklizkova, and V. V. Kudryavtsev

St. Petersburg State Electrotechnical University, St. Petersburg, 197376 Russia
Institute of Macromolecular Compounds, Russian Academy of Sciences, St. Petersburg, 199004 Russia
** e-mail: lb_lab@cmid.ru*
Received December 9, 2004

Abstract—An ultrathin polyimide membrane network has been formed for the first time on a metal grid matrix using the Langmuir–Blodgett method. The ratio of the membrane thickness to the grid mesh reaches 1 : 1000.

The strong prospects for the application of polyimide (PI) films prepared using the Langmuir–Blodgett (LB) method are related primarily to the possibility of obtaining ultrathin polymer layers (with thicknesses ranging from 0.5 to 100–300 nm) possessing high thermal stability and mechanical strength [1]. The LB films are usually applied onto the surface of solid inorganic substrates and, less frequently, onto polymeric materials [2]. It is also of considerable general and applied interest to obtain and study strong ulrathin PI membranes supported by grids or by substrates with micron holes. Using such membranes, it is possible to create new and develop the existing micromechanical devices, such as microvalves, micropumps, acoustic microconverters, and optical and chemical microsensors.

The PI-based LB films are usually prepared as follows. In the first step, the film of an amphiphilic prepolymer is obtained by the LB method on a solid substrate. Then, the film is subjected to thermal or chemical cyclization (imidization), which results in the PI structure formation [3].

The aim of this study was to obtain a network of nanometer-thick membranes of a rigid-chain PI on "hollow" substrates representing metal grids of micron mesh size. Important specific features of the rigid-chain PI based on 3,3',4,4'-diphenyltetracarboxylic acid dianhydride and *o*-tolidine (DP–*o*TD) are the high thermal stability (a 5% weight loss at 560°C) and low temperature expansion coefficient (0.5×10^{-5} K^{-1}). The LB films were obtained using a prepolymer representing an alkylammonium salt of DP–*o*TD polyamic acid with two molecules of tertiary amine (*o*,*o*',*o*''-trihexadecanoyltriethanolamine) per monomer unit of the polymer chain. The prepolymer monolayers and LB films were prepared and their properties were studied in a special setup designed and constructed at the St. Petersburg State Electrotechnical University [4].

The results of our previous investigations showed that the selected prepolymer forms stable monolayers composed of densely packed polymer chains on the surface of water. Investigation of the polyamic acid salt monolayers transferred onto (100)-oriented singe crystal silicon substrates showed that the process was of the *Y* type [5] and the transfer coefficient was 1.0–1.1 for the surface pressure in the monolayer ranging within 25–35 mN/m.

The networks of ultrathin PI membranes were formed on nickel grids for electron microscopy with a 40×40 μm mesh size and a thickness of 7 μm. In the first step, 50, 100, or 200 monolayers of the prepolymer were transferred onto the grids at a surface pressure in the monolayer of 30 mN/m. The grid velocity in the course of the monolayer transfer was 0.2 cm/min. The *Y*-type process was characterized by a transfer coefficient of 0.9–1.0. In order to determine the film thickness, the prepolymer monolayers were transferred under the same conditions onto Si(100) single crystal substrates. In this case, the monolayer transfer coefficient was 1.0–1.1. Then, the film thickness on the silicon surface was determined with the aid of ellipsometry. The measurements were performed in air using an LEF-101 ellipsometer equipped with a laser source operating at a wavelength of 632.8 nm. The film thickness was calculated using the Holmes method within the framework of a single-layer model.

The LB films of the prepolymer transferred onto the metal grid were examined in an optical microscope. It was established that 95% of the grid cells over a total area of about 1 cm^2 are covered by the film (Fig. 1). The samples of prepolymer films on the grid and on silicon were simultaneously heated to various temperatures (200, 250, 300, 325, 350, 375, and 400°C). Figure 2 shows a plot of the calculated thickness of one monolayer in a film heated to various temperatures. As can be seen, the monolayer thickness in the LB film of the prepolymer decreases from 2.9 to 0.7 nm upon heating to

1063-7850/05/3104-0341$26.00

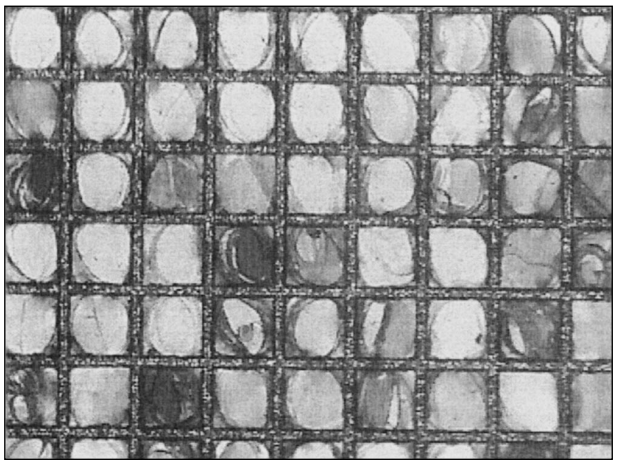

Fig. 1. Microphotograph of a 200-monolayer LB film of a polyamic acid salt prepolymer on a nickel grid with a 40 × 40 μm mesh size.

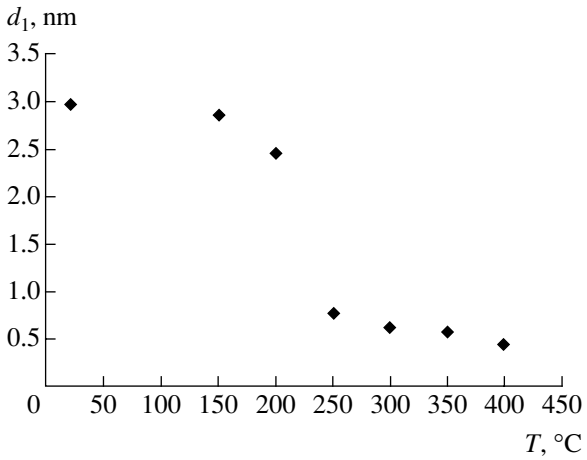

Fig. 2. A plot of the calculated monolayer thickness d_1 in an LB film on a silicon substrate versus imidization temperature *T*.

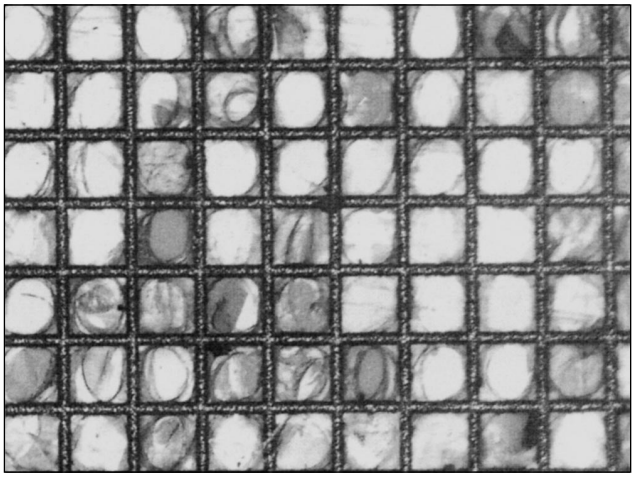

Fig. 3. Microphotograph of a 200-monolayer-thick PI membrane on a nickel grid with a 40 × 40 μm mesh size.

250°C, which is evidence of a complete removal of the tertiary amine component. As the temperature is increased from 250° to 400°, the monolayer thickness changes rather insignificantly and eventually reaches 0.44 nm. This value corresponds to the diameter of the PI DP–*o*TD chain, which is evidence for the formation of a dense package of polymer chains in the LB film.

Microscopic examination of the LB films on the grid showed that the film was retained on 90–95% of the grid cells over a total area of 1 cm^2 after thermal treatment at 200, 250, and 300°C (Fig. 3). Thus, the film integrity was virtually not affected by the significant shrinkage of the film as a result of removal of the tertiary amine with aliphatic chains. At the same time, heating above 300°C led to breakage of the films on the grid. This is probably related to stresses arising in the film in the course of formation of a dense package of polymer chains.

Judging by the data for the control films transferred onto silicon substrates, the thicknesses of 50-, 100-, and 200-monolayer films formed on the grid upon heating to 300°C must be 35, 70, and 140 nm, respectively. However, the micrograph presented in Fig. 3 shows that the film thickness was not the same in all cells of the grid.

Since water adsorbed on the surface of membranes may significantly influence their characteristics, we have measured the contact angle for water on the surface of PI films formed on silicon substrates. The obtained values (80–90°C) are indicative of highly hydrophobic properties of the surface of PI DP–*o*TD films.

To summarize, we have experimentally demonstrated the possibility of forming nanometer-thick polymeric films of thermally and chemically stable rigid-chain PI on "hollow" metal grid matrices with the ratio of the membrane thickness to the grid mesh reaching 1 : 1000.

Acknowledgments. This study was supported by the Russian Foundation for Basic Research (project no. 02-03-32683) and the Presidential Program of Support for Leading Scientific Schools in Russia (project no. NSh-1824.2003.3).

REFERENCES

1. M. I. Bessonov, M. M. Koton, V. V. Kudryavtsev, and A. A. Laius, *Polyimides: A Class of Thermally Stable Polymers* (Nauka, Leningrad, 1983), p. 72 [in Russian].
2. G. A. Polotskaya, V. P. Sklizkova, S. I. Goloudina, *et al.*, in *Proceedings of the 4th International Symposium on Molecular Order and Mobility in Polymer Systems, St. Petersburg, 2002*, p. 125.
3. M. Suzuki, M. Kakimoto, T. Konishi, *et al.*, Chem. Lett., 395 (1986).
4. V. M. Pasyuta and S. I. Goloudina, Peterburg. Zh. Elektron., No. 4, 71 (2001).
5. S. I. Goloudina, V. P. Sklizkova, V. M. Pasyuta, *et al.*, Poverkhnost, No. 10, 93 (2003).

Translated by P. Pozdeev

Technical Physics Letters, Vol. 31, No. 4, 2005, pp. 343–345. Translated from Pis'ma v Zhurnal Tekhnicheskoĭ Fiziki, Vol. 31, No. 8, 2005, pp. 62–66.

Macrokinetic Description of the Elimination of Volatile Organic Impurities from Gases Using Plasmachemical Methods

E. V. Kolman and I. E. Filatov*

Institute of Electrophysics, Ural Division, Russian Academy of Sciences, Yekaterinburg, Russia

** e-mail: fil@iep.uran.ru*

Received November 30, 2004

Abstract—We present a mathematical model describing the elimination of volatile organic impurities from gases by plasmachemical methods and formulate criteria for the purification of a medium from an impurity. Comparison of the developed theory to experimental data on the styrene conversion in ionized air shows adequacy of the description. Using the proposed model, it is possible to generalize data obtained for the gas mixtures of various compositions with allowance for the method of activation employed in each particular case. A change in the reaction order with respect to the eliminated component is demonstrated. The obtained relations provide a basis for the development of effective methods of eliminating toxic compounds from waste gases.

Introduction. Interest in the investigation of conversion of volatile organic compounds in the gas phase is related to the diversity of chemical processes involving such compounds and their high lability in non-thermal plasma. Volatile organic compounds enter as components in waste gases of various chemical technologies. The problem of air purification from toxic organic impurities can be successfully solved using physical methods [1] that employ various plasmachemical reactions leading to the conversion of impurities in ionized air. Unfortunately, mathematical modeling of the process of organic impurity elimination from a gaseous medium is hindered by the substantially nonequilibrium character of such processes and by the lack of data on the conversion rate constants. Additional difficulties are related to the variety of methods used for the generation of plasma, which complicates the correct comparison of various processes with respect to energy efficiency.

This paper presents a theoretical description of the elimination of volatile organic impurities from gases by plasmachemical methods. The proposed formal approach reflects the conversion of an impurity compound on the whole and takes into account the main interaction directions, not separating particular chemical reactions.

Mathematical model. Consider a gaseous system comprising a mixture of two components: a medium (e.g., air) and an impurity (a compound to be eliminated). The energy introduced in the medium leads to the generation of active species participating in plasmachemical reactions, which are jointly referred to below as pseudoreagents. The chemical processes in the system under consideration are described by the following system of differential equations:

$$\begin{cases} \dfrac{d[X]}{dW} = -\sum\limits_{i=1}^{N} k_{1i}[X]^a[R_i]^b, \\ \dfrac{d[R_i]}{dW} = k - \sum\limits_{i=1}^{N} k_{1i}[X]^a[R_i]^b - \sum\limits_{i=1}^{N} k_{2i}[R_i]^b \\ - \sum\limits_{i=1}^{N}\sum\limits_{j=1}^{N} k_{3ij}[A_j]^c[R_i]^b, \\ \dfrac{d[A_j]}{dW} = \sum\limits_{i=1}^{N} k_{1i}[X]^a[R_i]^b - \sum\limits_{i=1}^{N}\sum\limits_{j=1}^{N} k_{3ij}[A_j]^c[R_i]^b, \end{cases} \quad (1)$$

where $[X]$, $[R]$, and $[A]$ are the concentrations of the impurity, the pseudoreagent, and the reaction product, respectively; N is the number of distinguished processes; a, b, and c are the reaction orders with respect to the impurity, the pseudoreagent, and the reaction product, respectively; k is the rate constant of pseudoreagent production; k_{1i}, k_{2i}, and k_{3ij} are the coefficients characterizing various energy contributions to the process under consideration; and W is the energy deposited per unit volume of the gas. In this study, we restrict consideration to the following processes: impurity elimination at a rate constant k_1 (representing the total coefficient for all processes of interaction between the impurity and the pseudoreagent); pseudoreagent production at the expense of the energy introduced into the system at a rate constant of k; and two channels of

1063-7850/05/3104-0343$26.00 © 2005 Pleiades Publishing, Inc.

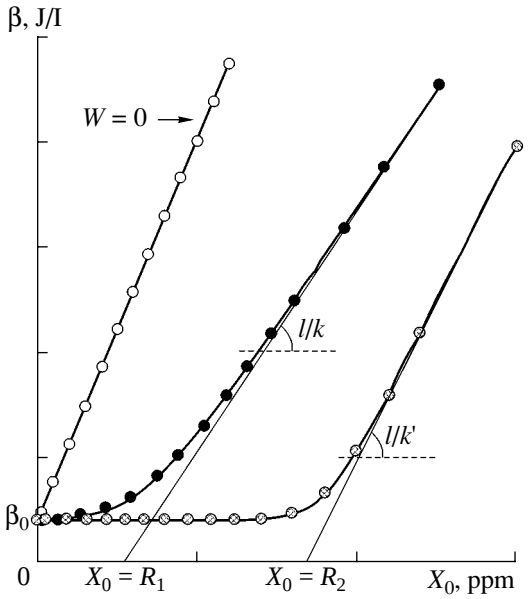

Fig. 1. Theoretical plots of the characteristic energy β versus initial concentration of the eliminated impurity.

pseudoreagent consumption—the main (impurity elimination) and the side (interaction with the medium components)—at a total rate constant of k_2. Under stationary conditions, the pseudoreagent concentration is maintained at constant, so that

$$\begin{cases} \dfrac{dX}{dW} = -k_1 RX, \\ \dfrac{dR}{dW} = k - k_1 RX - k_2 R = 0. \end{cases} \tag{2}$$

The solution of this system of equations is given by the relation

$$X_0 - X + \frac{k_2}{k_1}\ln\frac{X_0}{X} = kW, \tag{3}$$

where X_0 is the initial impurity concentration. The explicit expression for the impurity concentration is $X = (k_2/k_1)A$, where

$$A = \text{Lambert}W\left(\frac{k_1}{k_2}X_0\exp\left(\frac{k_1}{k_2}(X_0 - kW)\right)\right),$$

$$\text{Lambert}W(x)\exp(\text{Lambert}W(x)) = x.$$

An attempt at a kinetic description of the processes in a gaseous system was undertaken in [2], where consideration was restricted to a single (preferred) channel of the consumption of radicals—active species generated by a streamer crown discharge reactor. The main criterion of the efficiency of the impurity elimination process is the characteristic energy β with respect to the eliminated impurity (expressed in joules per liter) defined as

$$\beta = \frac{1}{d\left(\ln\dfrac{X_0}{X}\right)/dW} = \frac{k_2(1+A)}{kk_1},$$
$$\beta_0 = \lim_{X_0 \to 0}\beta = \frac{k_2}{kk_1} = \frac{1}{\alpha k}, \tag{4}$$

where β_0 is the minimum characteristic energy for a given method (which is analogous to the quantity introduced in [2]) and $\alpha = \dfrac{k_1}{k_2}$ is the coefficient characterizing the process direction. The lower the β value, the higher the process efficiency. As the X_0 value increases, the $\beta = \beta(X_0)$ functions transform into a linear dependence with the slope $\gamma = 1/k$ characterizing the efficiency of energy introduction into the system.

Figure 1 shows the theoretical curves of $\beta = \beta(X_0)$. As can be seen, the reaction order with respect to the eliminated compound changes at $X_0 \approx R$, where $R = kW$ is the formal reagent concentration. Different slopes of the curves corresponding to various initial impurity concentrations reflect the influence of the method used for the generation of active species.

We propose to characterize the process of impurity elimination from air by the following parameters: $\eta \equiv 1 - \dfrac{X}{X_0}$, which describes the degree of purification, and

$$\varepsilon = \frac{1}{k} - \frac{\beta_0\ln(1-\eta)}{\eta X_0},$$

which shows the energy spent per molecule of the impurity (provided that the reaction mechanism remains unchanged). The deviation of the experimental data from theoretical predictions is indicative of the presence of an alternative mechanism (chain reactions, etc.).

Experiment. In order to qualitatively verify the proposed mathematical model, we have used the experimental data reported in [3] for the experimental conversion of styrene vapor using a pulsed electron beam. The experiments were performed on a setup comprising a laboratory electron accelerator of the RADAN type [4], a gas chamber with a system controlled gas supply, and a streamer crown discharge reactor [3].

As can be seen from the experimental data presented in Fig. 2, the parameter β strongly depends on the initial styrene concentration X_0. These data reflect the main characteristics of the process of styrene conversion and show the region where the reaction order with respect to styrene changes from the first to zeroth. As $X_0 \longrightarrow \infty$, the impurity concentration tends to obey the linear law $X = X_0 - kW$. Different slopes of the linear segments

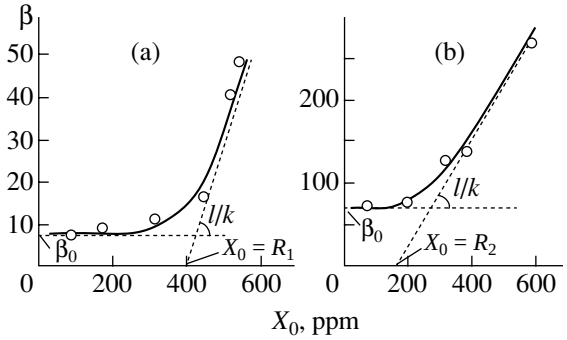

Fig. 2. Experimental plots of the characteristic energy β versus initial concentration of the impurity (styrene vapor) eliminated under the action of (a) a pulsed electron beam and (b) a streamer crown discharge.

$\beta = \beta(X_0)$ at large X_0 correspond to various methods of action upon the system. A comparative analysis of the theory and experiment shows that the proposed model is qualitatively correct. For the quantitative estimates, it is necessary to introduce an additional criterion characterizing the irradiated region of the working volume.

Conclusions. We proposed a mathematical model that correctly qualitatively describes the process of an organic impurity conversion under the action of electron beams and discharges. A set of criteria characterizing the impurity conversion process includes the minimum characteristic energy with respect to the impurity, the efficiency of energy introduction into the system, and the formal reagent concentration. We have also formulated conditions corresponding to a change in the reaction order with respect to the eliminated impurity.

REFERENCES

1. *Non-Thermal Plasma Techniques for Pollution Control*, Ed. by B. M. Penetrante and S. E. Schultheis (Springer-Verlag, Berlin, 1993), NATO ASI Series, Vol. G34, Part A, p. 398; Part B, p. 397.
2. K. Yan, E. J. M. Heesch, A. J. M. Pemen, and P. A. H. J. Huijbrechts, Plasma Chem. Plasma Process. **21**, 107 (2001).
3. Yu. N. Novoselov and I. E. Filatov, Dokl. Akad. Nauk **382** (4), 1 (2002).
4. A. S. El'chaninov, A. S. Kotov, V. G. Shpak, *et al.*, Elektron. Tekh., Ser. 4, No. 2, 33 (1987).

Translated by P. Pozdeev

Technical Physics Letters, Vol. 31, No. 4, 2005, pp. 346–348. Translated from Pis'ma v Zhurnal Tekhnicheskoĭ Fiziki, Vol. 31, No. 8, 2005, pp. 67–73.

Features of the Electromechanical Properties of 0–3 Composites of the $Pb(Zr,Ti)O_3$-Based Ferroelectric Ceramics–Polymer Type

S. V. Glushanin and V. Yu. Topolov*

Rostov State University, Rostov-on-Don, Russia

** e-mail: topolov@phys.rsu.ru*

Received December 7, 2004

Abstract—We have analyzed the experimental concentration dependences of the permittivity $\varepsilon_{33}^{*\sigma}(m_{FC})$ and the piezoelectric coefficient $d_{33}^{*}(m_{FC})$ of 0–3 connectivity composites comprising ferroelectric ceramic inclusions with a volume fraction m_{FC} dispersed in a piezoactive or piezopassive polymer matrix. Both concentration dependences at $0.1 < m_{FC} \le 0.6$ can be interpreted within the framework of a new model of the 0–3 composite representing two systems of inclusions—spherical and cylindrical (elongated in the polarization axis direction). It is established that the elongated inclusions determine to a considerable extent the piezoelectric and dielectric properties of the 0–3 composites of the $Pb(Zr,Ti)O_3$-based ferroelectric ceramics–polymer type with $m_{FC} \ge 0.2$. © *2005 Pleiades Publishing, Inc.*

In recent years, a large number of publications have been devoted to experimental investigations [1–4] and theoretical predictions [5–10] of the effective physical properties of the 0–3 connectivity composites of the ferroelectric ceramic (FC)–polymer type. However, the influence of the evolution of a microstructure on the properties of these materials has not been considered in sufficient detail. As a rule, the elastic, piezoelectric, and dielectric properties of these FC–polymer composites, with the FC components representing perovskitelike ceramics (based on $BaTiO_3$, $Pb(Zr,Ti)O_3$, other compounds of the lead zirconate titanate (PZT) group, etc.), have been described within the framework of models taking into account the interaction of inclusions of a given shape (parallelepiped [6–8], spheroid [8–10]) with the surrounding media. This approach leaves open certain questions concerning the influence of changes in the microstructure (related to an increase in the bulk FC concentration in the composite) on the effective properties of materials. However, the importance of these questions was demonstrated by the results of recent experimental investigations of the relationship between microstructure and electromechanical properties of porous FCs based on $Pb(Zr,Ti)O_3$ [11] and was further confirmed by the results of modeling of the effective properties of piezoactive materials in a broad range of porosity [12].

This paper presents the results of an investigation of the relationship between microstructure and electromechanical properties of the 0–3 connectivity composites of the $Pb(Zr,Ti)O_3$-based FC–polymer type and the interpretation of experimental data [1] in a broad range of the volume fraction of the FC component (m_{FC}).

We have analyzed the concentration dependences [1, 3] reported for the permittivity $\varepsilon_{33}^{*\sigma}(m_{FC})$ of a mechanically free sample and the piezoelectric coefficient $d_{33}^{*}(m_{FC})$ measured at room temperature for the 0–3 connectivity composites comprising $Pb(Zr,Ti)O_3$-based FC dispersed in a polymer matrix based either on a 70/30 mol % copolymer of vinilydene fluoride and trifluoroethylene [P(VDF–TrFE)] (composite I) or on pure poly(vinylidene fluoride) (PVDF) (composite II). This analysis revealed the following features. The behavior of the ratio of permittivities $\beta_\varepsilon = \varepsilon_{33}^{*\sigma}(m_{FC})/\varepsilon_{33}^{*\sigma}(1)$ depending on m_{FC} in the related composites I and II is different, which is explained by the complicated dependence of β_ε on the directional polarization of components and by differences in the technology of sample preparation. Analogous differences are observed for the ratio of piezoelectric constants $\beta_d = d_{33}^{*}(m_{FC})/d_{33}^{*}(1)$. At the same time, the numerical estimations of β_ε and β_d obtained within the framework of the model of 0–3 composites with spherical inclusions [9] for the compositions analogous to I and II

1063-7850/05/3104-0346$26.00 © 2005 Pleiades Publishing, Inc.

showed a good agreement between theory and experiment [1, 3] only for $m_{FC} \le 0.1$.[1]

We believe that the observed difference in the behavior of β_ε and β_d is related to the neglect of certain features of the 0–3 composite microstructure, which become substantial with increasing m_{FC} [15]. Below we will indicate changes in the microstructure which influence the behavior of $\beta_\varepsilon(m_{FC})$ and $\beta_d(m_{FC})$.

It is assumed that composites of the 0–3 connectivity type consist of layers of two types alternating in the direction along the OX_3 polarization axis. Layers of the first type with the relative content $1 - m$ possess a cellular structure and contain a system of isolated spherical inclusions with a rather small volume fraction n_0. In layers of the second type with the relative content m, the spherical inclusions approach each other to form a structure resembling a cylindrical rod (see the inset to Fig. 1), which favors polarization of the composite. The electromechanical properties of such structures are considered as practically coinciding with those of the pure FC, since the volume fraction of the polymer component is small and the FC inclusions form continuous chains aligned in the OX_3 axis. The volume fraction n_1 of the FC rods in these layers may vary from 0 to $\pi/4$ (the maximum value corresponds to the area of a circle inscribed into a square on the X_1OX_2 plane to the area of this square). The volume fraction of the FC in the composite under consideration is $m_{FC} = n_1 m + n_0(1 - m)$, and the effective electromechanical properties are determined using a three-step procedure. First, averaging with respect to n_0 is performed using formulas from [16]; then, averaging with respect to n_1 is carried out using formulas from [17]; finally, averaging with respect to m is performed using formulas from [18], which yields the complete set of elastic, piezoelectric, and dielectric constants of the given 0–3 connectivity composite (Fig. 1) with the symmetry group ∞mm.

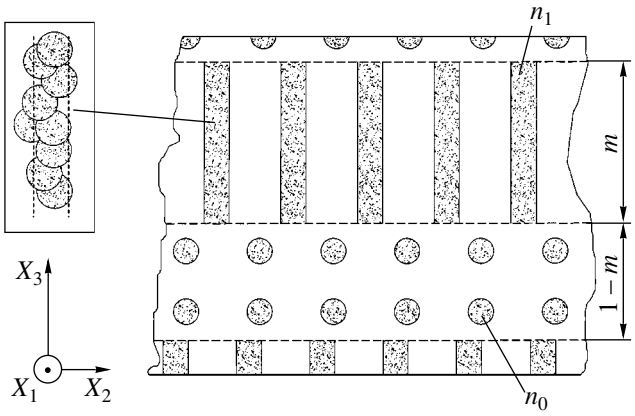

Fig. 1. Schematic diagram of the structure of 0–3 connectivity composites of the FC–polymer type: m is the relative content of layers containing FC rods (with an FC volume fraction n_1 in these layers); $1 - m$ is the relative content of layers containing FC spheres (with an FC volume fraction n_0 in these layers); the inset shows a fragment of the rod consisting of a large number of closely spaced spherical FC inclusions.

Figure 2 shows the results of calculations of the $\beta_\varepsilon(m_{FC})$ and $\beta_d(m_{FC})$ values in comparison to the corresponding experimental data for the composite I. The presence of two piezoactive components (Figs. 2a and 2b) favors variation of the piezoelectric coefficient $d_{33}^*(m_{FC})$ in a broad interval, which is explained by the opposite signs of the piezoelectric coefficients of components ($\operatorname{sgn} d_{33}^*(0) = -\operatorname{sgn} d_{33}^*(1)$ [1, 13, 14]) and by the electromechanical interaction of components. At the same time, the permittivity $\varepsilon_{33}^{*\sigma}(m_{FC})$ varies in virtually the same manner (Figs. 2a and 2c) irrespective of the piezoelectric activity of the polymer component. A comparison of the calculated and measured values of β_ε and β_d leads to a conclusion concerning the important role of elongated FC inclusions (layers with the volume fraction m in Fig. 1) as the factor determining both concentration dependences $\varepsilon_{33}^{*\sigma}(m_{FC})$ and $d_{33}^*(m_{FC})$ of the 0–3 composite I. Even for an FC volume fraction $m_{FC} = 0.2$–0.3, the density of such inclusions may reach $n_1 \approx 0.3$–0.4 for $m \approx 0.5$–0.7. As the m_{FC} increases to 0.6, m grows to 0.9–0.95 and the composite structure approaches that of the 1–3 connectivity type. Lower m values corresponding to the experimental data for β_ε and β_d for the composite with a piezopassive polymer matrix at $m_{FC} \ge 0.3$ (Figs. 2c and 2d), as well as a lower correlation between m values corresponding to β_ε and β_d for the composite with $n_1 = \text{const}$, are indirectly indicative of less favorable polarization conditions in this material as compared to the composite with a

[1] It should be noted that the available literature contains no complete sets of electromechanical constants for PZT-based FCs (PKI 502, APC 850) or 70/30 mol % P(VDF–TrFE), the components of composites studied in [1, 3]. For this reason, our calculations were performed using the experimental room-temperature data reported for PZ 27 (an FC of the Navy II type belonging to the same group as PKI 502) [13] and 75/25 mol % P(VDF–TrFE) [14]. The ratios of $d_{33}^*(1)/\varepsilon_{33}^{*\sigma}(1)$, $d_{33}^*(0)/d_{33}^*(1)$, and $\varepsilon_{33}^{*\sigma}(0)/\varepsilon_{33}^{*\sigma}(1)$ calculated using the data for PZ 27 and 75/25 mol % P(VDF–TrFE) [13, 14] are close to the experimental values for the samples studied in [1]. Previously, Nan and Weng [5] attempted to interpret the experimental data for $\varepsilon_{33}^{*\sigma}(m_{FC})$ and $d_{33}^*(m_{FC})$ reported in [1] using the values of constants for PZT-7A and P(VDF–TrFE) (without indication of the molar ratio of the comonomers). However, the parameters presented in [5] for the polymer matrix significantly differ from those for 75/25 mol % P(VDF–TrFE) [14] (in particular, the elastic moduli differ by a factor of about two). We believe that this accounts for significant discrepancies between calculated [5] and experimental [1] values of $d_{33}^*(m_{FC})$ of the 0–3 composite I for $m_{FC} \ge 0.15$.

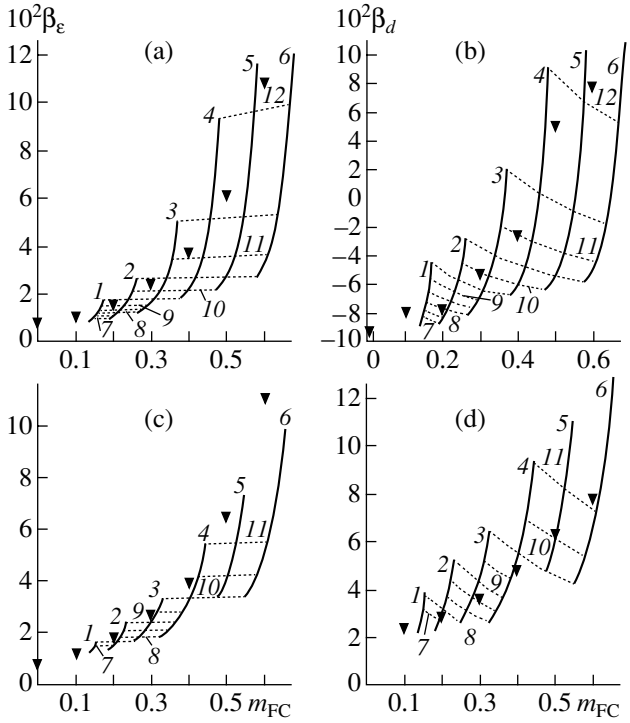

Fig. 2. Concentration dependences of (a, c) $10^2\beta_\varepsilon$ and (b, d) $10^2\beta_d$ calculated for the 0–3 composite PZ 27–75/25 mol % P(VDF–TrFE) with the components polarized (a, b) in the same direction (piezoactive polymer) and (c, d) in the opposite direction (piezopassive polymer); n_0 = 0.10; n_1 = 0.20 (*1*), 0.30 (*2*), 0.40 (*3*), 0.50 (*4*), 0.60 (*5*), 0.70 (*6*); m = 0.45 (*7*), 0.55 (*8*), 0.65 (*9*), 0.75 (*10*), 0.85 (*11*), 0.95 (*12*); triangles represent experimental data for β_ε and β_d from [1].

piezoactive polymer matrix. It should also be pointed out that composite I with a maximum volume FC fraction $m_{FC} \approx 0.6$ studied in experiment displayed no FC inclusions continuously arranged throughout the sample along the polarization axis (i.e., 0–3 connectivity was observed [1]).

Thus, the results of our investigation provide evidence that the new model can be used for the description of electromechanical properties of 0–3 connectivity composites in terms of the volume fractions of components. The calculated values and the comparative analysis of theory and experiment indicate that the interval of FC volume fractions $0.2 \le m_{FC} \le 0.6$ corresponds to a higher sensitivity of both piezoelectric and dielectric properties along the polarization axis with respect to parameters of the system of elongated FC inclusions (Fig. 1). This factor of the microstructure, as well as the piezoelectric activity of the polymer matrix must be taken into account in the creation of new highly effective 0–3 connectivity composites.

Acknowledgments. The authors are grateful to Prof. A.V. Turik (Russia) and to Dr. M. Kamlah (Germany) for their interest in the subject under investigation.

This study was supported in part by the Ministry of Education of the Russian Federation (project no. A04-2.9-141).

REFERENCES

1. K. L. Ng, H. L. W. Chan, and C. L. Choy, IEEE Trans. Ultrason. Ferroelectr. Freq. Control **47**, 1308 (2000).
2. D.-N. Fang, A. K. Soh, C.-Q. Li, and B. Jiang, J. Mater. Sci. **36**, 5281 (2001).
3. E. Venkatragavaraj, B. Satish, P. R. Vinod, and M. S. Vijaya, J. Phys. D: Appl. Phys. **34**, 487 (2001).
4. C. K. Chiang and R. Popielarz, Ferroelectrics **275** (1–4), 1 (2002).
5. C.-W. Nan and G. J. Weng, J. Appl. Phys. **88**, 416 (2000).
6. F. Levassort, V. Yu. Topolov, and M. Lethiecq, J. Phys. D: Appl. Phys. **33**, 2064 (2000).
7. C. R. Bowen and V. Yu. Topolov, Acta Mater. **51**, 4965 (2003).
8. Yu. V. Sokolkin and A. A. Pan'kov, *Electroelasticity of Piezoelectric Composites with Irregular Structure* (Fizmatlit, Moscow, 2003) [in Russian].
9. S. V. Glushanin, V. Yu. Topolov, and A. V. Krivoruchko, Pis'ma Zh. Tekh. Fiz. **30** (20), 69 (2004) [Tech. Phys. Lett. **30**, 874 (2004)].
10. A. V. Turik, A. I. Chernobabov, G. S. Radchenko, and S. A. Turik, Fiz. Tverd. Tela (St. Petersburg) **46**, 2139 (2004) [Phys. Solid State **46**, 2213 (2004)].
11. H. Kara, R. Ramesh, R. Stevens, and C. R. Bowen, IEEE Trans. Ultrason. Ferroelectr. Freq. Control **50**, 289 (2003).
12. A. A. Vorontsov, S. V. Glushanin, V. Yu. Topolov, and A. E. Panich, *Future of Aims for Engineering Science: A Collection of Scientific Works*, Ed. by V. I. Bol'shakov (Gaudeamus, Dnepropetrovsk, 2003), No. 5, pp. 107–114 [in Russian].
13. M. Algueró, C. Alemany, and L. Pardo, J. Am. Ceram. Soc. **87**, 209 (2004).
14. H. Taunaumang, I. L. Guy, and H. L. W. Chan, J. Appl. Phys. **76**, 484 (1994).
15. H. L. W. Chan, Y. Chen, and C. L. Choy, IEEE Trans. Dielectr. Electr. Insul. **3**, 800 (1996).
16. V. Yu. Topolov and S. V. Glushanin, Pis'ma Zh. Tekh. Fiz. **28** (7), 38 (2002) [Tech. Phys. Lett. **28**, 279 (2002)].
17. A. A. Grekov, S. O. Kramarov, and A. A. Kuprienko, Mekh. Kompoz. Mater., No. 1, 62 (1989).
18. L. P. Khoroshun, B. P. Maslov, and P. V. Leshchenko, *The Prediction of Effective Properties for Piezoactive Composite Materials* (Naukova Dumka, Kiev, 1989) [in Russian].

Translated by P. Pozdeev

Technical Physics Letters, Vol. 31, No. 4, 2005, pp. 349–351. Translated from Pis'ma v Zhurnal Tekhnicheskoĭ Fiziki, Vol. 31, No. 8, 2005, pp. 74–78.

The Space Charge Wave Induced Hall Effect

V. V. Bryksin and M. P. Petrov*

Ioffe Physicotechnical Institute, Russian Academy of Sciences, St. Petersburg, 194021 Russia

** e-mail: mpetr.shuv@mail.ioffe.ru*

Received December 14, 2004

Abstract—A mechanism is proposed according to which the Hall effect arises due to the space charge wave rectification in semi-insulating semiconductors. © *2005 Pleiades Publishing, Inc.*

A semi-insulating semiconductor containing a sufficiently large number of trapping centers and placed into an external electric field may feature trap recharge waves, which are essentially space charge waves (SCWs) [1, 2]. In the materials studied, these SCWs appeared as low-frequency oscillations of the charge density with a characteristic spatial period within 5–50 μm and a frequency of 10–1000 Hz. The excitation of such SCWs may be accompanied by their rectification (including spatial and complete rectification) [3–5], which leads to the generation of an alternating current at the SCW frequency and influences the direct current flowing in the sample.

If a sample in which the SCWs are excited and their rectification takes place is exposed to a magnetic field, it can be also expected that (i) a Hall current will arise at the corresponding frequency and (ii) the traditional Hall current (at a zero frequency) will exhibit a change. This ac Hall effect was successfully demonstrated in [6], where neither ac nor dc voltage was applied to a sample, so that the observed effect was related to the induced charge density relaxation oscillations (rather than to the SCW rectification). Accordingly, the observed effect was 10–1000 times smaller than that predicted below.

Consider a scheme for the optical excitation of SCWs and the Hall effect measurements depicted in the figure. In this system, the sample is irradiated by two coherent light beams, one of which is phase-modulated with a frequency of Ω and an amplitude of Θ. The incident beams form the interference pattern oscillating at the frequency Ω relative to the middle position. At a small modulation amplitude Θ, this pattern can be described as

$$\begin{aligned} W(x,t) &= W_0[1 + m\cos(Kx + \Theta\cos\Omega t)] \\ &\cong W_0(1 + m\cos Kx) - \frac{W_0 m\Theta}{2} \\ &\times [\sin(Kx - \Omega t) + \sin(Kx + \Omega t)], \end{aligned} \tag{1}$$

where m is the contrast, W_0 is the average intensity of the incident light beam, and $K = 2\pi/\Lambda$, Λ is the period of the interference pattern. Since the crystals studied are photoconductors, the light action results in the formation of a standing space-charge grating (related to the $W_0 m\cos Kx$ term in Eq. (1)) and two running gratings (related to the last two terms in Eq. (1)), which propagate in the opposite directions.

If the propagation direction, velocity, and period of one of the running gratings coincide with those of an intrinsic SCW mode, the corresponding mode exhibits resonance excitation. The interaction of this SCW with the static space-charge grating is accompanied by spatial rectification, that is, by the appearance of an ac current with a density given by the relation [5]

$$I_1(t) = I_1(\Omega)\cos\Omega t, \tag{2}$$

where

$$\begin{aligned} I_1(\Omega) &= \frac{\sigma E_0 m^2 \Theta\Omega\tau_M d}{2(1+q)} \\ &\times \frac{1}{\sqrt{[(1-\Omega\tau_M d)^2 + \Omega^2\tau_M^2][(1+\Omega\tau_M d)^2 + \Omega^2\tau_M^2]}}. \end{aligned} \tag{3}$$

σ is the specific conductivity of a homogeneously illuminated sample; τ_M is the Maxwell relaxation time; $d = \mu\tau KE_{int}$; μ and τ are the carrier mobility and lifetime, respectively; and q is a parameter taking into account two factors decreasing the effective field inside the crystal. The first factor is related to the possible voltage drop on non-ohmic contacts, while the second corresponds to a voltage drop on the load resistor in the circuit. The q value can be expressed in terms of the calculated field $E_0 = U/L$ and the real internal field E_{int} via the relation $1 + q = E_0/E_{int}$, where U is the bias source voltage and L is the interelectrode distance. According to another (fully equivalent) definition, this parameter can be determined as $q = R_{ef}/R_{cr}$, where R_{ef} is the effec-

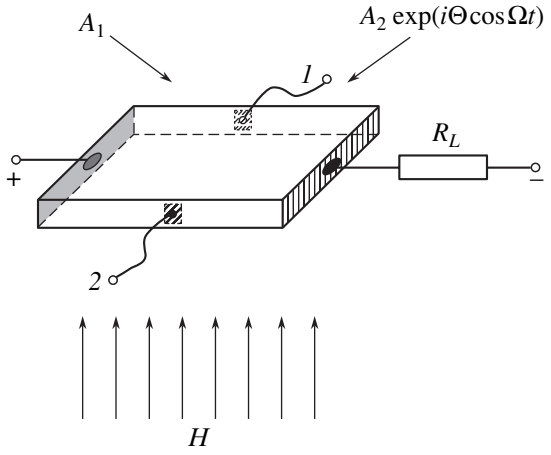

Schematic diagram of a sample for the investigation of SCW-induced Hall effect: R_L is the load resistance in the bias voltage circuit; H is the magnetic field; (*1*, *2*) are the Hall contacts in the open-circuit regime; (A_1, A_2) are the amplitudes of laser beams exciting the SCWs.

tive resistance (including the load resistance R_L and the contact resistance) and R_{cr} is the crystal resistance (in a direction parallel to the applied field). In writing Eq. (2), we omitted (for the sake of brevity) a phase shift between the phase modulation and the $I_1(t)$ signal.

Interaction between the two running SCWs results in their complete rectification, after which the density of a dc current flowing in the sample exhibits a change described by the formula [4]

$$\Delta I_0(\Omega) = \frac{\sigma E_0 m^2 \Theta^2}{8(1+q)^2} \times\left[2 - \frac{1}{(1-\Omega\tau_M d)^2 + \Omega^2\tau_M^2} - \frac{1}{(1+\Omega\tau_M d)^2 + \Omega^2\tau_M^2}\right]. \quad (4)$$

Application of an external magnetic field H gives rise to the Hall emf, which is proportional to a current passing through the sample. The Hall effect is described in terms of the equations for E_H and n_H, which represent linear (with respect to H) Hall's corrections to the internal electric field E_{int} and the electron density n, respectively (see, e.g., [4, Eqs. (5)–(7)]):

$$n_H(x, y, t) = \frac{\tau\varepsilon}{4\pi e}\frac{\partial\Delta\varphi(x, y, t)}{\partial t},$$
$$\mathrm{div}\left(j_H - \frac{\varepsilon}{4\pi}\frac{\partial\nabla\varphi}{\partial t}\right) = 0. \quad (5)$$

Here, ε is the permittivity of the sample, φ is the potential of the magnetic-field-induced internal electric field, and

$$E_H = -\nabla\varphi, \quad j_{xH} = e\mu\left(n_H E_x - n\frac{\partial\varphi}{\partial x}\right),$$
$$j_{yH} = e\mu_{yx} n E_x - e\mu n\frac{\partial\varphi}{\partial y}. \quad (6)$$

In the approximation of $\varphi = U^{(H)}y/h$ (where $U^{(H)}$ is the voltage between the Hall contacts and h is the distance between these contacts), the final expression for the Hall current density (in the complex form) is as follows:

$$j^{(H)}(\Omega) = \frac{H\mu}{c}\frac{1 - i\Omega\tau_M q}{1 + q_H(1 + i\Omega\tau_M)} I(\Omega), \quad (7)$$

where $q_H = R_{LH}/R_{CH}$, R_{LH} is the load resistance in the Hall circuit (not depicted in the figure), $R_{CH} = h/\sigma S$ is the crystal resistance between the Hall contacts, S is the Hall contact area, c is the velocity of light, $I(\Omega) = I_{1C}(\Omega) + \Delta I_0(\Omega)$, and $I_{1C}(\Omega)$ is the complex (rather than real as in formula (3)) ac current amplitude in the bias circuit, which is given by formula (29) in [7]. In the low-frequency limit ($\Omega\tau_M \ll 1$), the real current density in the Hall circuit is

$$I^{(H)}(\Omega, t) = \frac{H\mu}{c}\frac{1}{1 + q_H}[I_1(t) + \Delta I_0(\Omega)]. \quad (8)$$

In the regime of short-circuit in the Hall circuit, $q_H = 0$. In the regime of disconnected Hall contacts ($q_H \longrightarrow \infty$), the real change in the voltage between the Hall contacts $\Delta U^{(H)}(\Omega, t)$ is

$$\Delta U^{(H)}(\Omega, t) = \frac{H\mu h}{c\sigma}[I_1(t) + \Delta I_0(\Omega)]. \quad (9)$$

The above results do not take into account the inhomogeneous distribution of the internal electric field along the x axis in the crystal. This inhomogeneity renders the problem of description of the Hall effect in the crystal substantially two-dimensional, which may lead to the appearance of vortex currents in the presence of a magnetic field. However, our preliminary analysis showed that such effects rather insignificantly influence the phenomena under consideration.

Acknowledgments. This study was supported by the Russian Foundation for Basic Research (project no. 05-02-16494).

REFERENCES

1. R. F. Kazarinov, R. A. Suris, and B. I. Fuks, Fiz. Tekh. Poluprovodn. (Leningrad) **6**, 572 (1972) [Sov. Phys. Semicond. **6** (1972)]; Fiz. Tekh. Poluprovodn. (Leningrad) **7**, 149 (1973) [Sov. Phys. Semicond. **7** (1973)]; Fiz. Tekh. Poluprovodn. (Leningrad) **7**, 688 (1973) [Sov. Phys. Semicond. **7** (1973)].

2. M. P. Petrov, V. V. Bryksin, V. M. Petrov, *et al.*, Phys. Rev. A **60**, 2413 (1999).

3. M. P. Petrov, V. V. Bryksin, H. Vogt, *et al.*, Phys. Rev. B **66**, 085107 (2002).

4. V. V. Bryksin and M. P. Petrov, Fiz. Tverd. Tela (St. Petersburg) **44**, 1785 (2002) [Phys. Solid State **44**, 1869 (2002)].

5. M. P. Petrov, V. V. Bryksin, C. E. Rüter, *et al.*, Phys. Rev. B **69**, 241201(R) (2004).

6. S. L. Sochava and S. I. Stepanov, J. Appl. Phys. **75**, 2941 (1994).

7. V. V. Bryksin, P. Klyainert, and M. P. Petrov, Fiz. Tverd. Tela (St. Petersburg) **45**, 1946 (2003) [Phys. Solid State **45**, 2044 (2003)].

Translated by P. Pozdeev

Technical Physics Letters, Vol. 31, No. 4, 2005, pp. 352–355. Translated from Pis'ma v Zhurnal Tekhnicheskoĭ Fiziki, Vol. 31, No. 8, 2005, pp. 79–87.

Nearly Backward Reflection of Elastic Waves in an Acousto-Optic Crystal of Paratellurite

V. B. Voloshinov*, O. Yu. Makarov, and N. V. Polikarpova

Department of Physics, Moscow State University, Moscow, 119992 Russia

** e-mail: volosh@phys.msu.ru*

Received November 23, 2004

Abstract—Some features of the propagation and reflection of acoustic waves in the *XY* plane of a paratellurite crystal have been studied. It is established that the acoustic waves exhibit an unusual backward reflection from the side crystal facet in the case of glancing incidence onto the crystal–vacuum interface. The experimental results are in good agreement with theoretical predictions. © *2005 Pleiades Publishing, Inc.*

Acousto-optic interactions are widely used in both basic science and technological applications in the schemes of beam control. The advantages of acousto-optic beam control are high efficiency, fast response, and broad functional possibilities [1–4]. In recent years, acousto-optic devices have also found applications in new, rapidly developing fields such as telecommunication networks, spectral filtration for structure imaging and pattern recognition, and some others [3, 4].

Such increasing practical requirements have stimulated the creation of novel acousto-optic devices, for example, tunable acousto-optic filters developed for optimal use. In particular, special narrowband acousto-optic filters for telecommunication networks employ nearly collinear geometry of the acousto-optic interaction in a birefringent crystal [5–9]. Realization of the quasi-collinear diffraction and creation of the quasi-collinear acousto-optic filters are based on the use of acoustically anisotropic materials. The development of such systems encounters certain difficulties related to the insertion of a light beam into the acoustic beam and the alignment of these beams in an acoustic waveguide. Solving this problem necessitates the use of the reflection of acoustic waves from crystal facets [6, 8, 9]. In an anisotropic material, this refection may exhibit quite unusual features.

Collinear acousto-optic filters are traditionally made of materials such as quartz, lithium niobate, paratellurite (TeO_2), calcium molybdate, and some others. However, solving new problems requires using new materials. In particular, much attention is now devoted to the acousto-optic materials effective in the IR range, such as calomel, tellurium, etc. [3–5]. One of the most widely used traditional acousto-optic materials is paratellurite. It should be noted that the aforementioned acousto-optic materials (as well as some others, such as Hg_2Br_2 and Hg_2I_2) are characterized by strongly anisotropic physical properties. The propagation of acoustic and electromagnetic waves in such media is accompanied by very complicated acousto-optic phenomena [10–12], which are interesting from a practical standpoint.

The concept of anisotropy in acousto-optics conventionally implied only the optical anisotropy, whereas the anisotropy of acoustical properties and the related features of acousto-optic interactions were treated rather superficially [1–4]. This approach is by no means justified, because the acoustical anisotropy of new acousto-optic materials can no longer be ignored. As is known from the theory of elasticity, the acoustical anisotropy of a medium is manifested, in particular, in that the group and phase velocity of sound make a nonzero angle with each other [1]. In the crystalline compounds of mercury and tellurium, these angles may reach 60°–70° and above [8, 9, 11, 12]. The acoustical anisotropy is characterized not only by different directions of the group and phase velocity of sound in crystals: it can also lead to very unusual phenomena accompanying the reflection of acoustic waves from crystal facets.

This study was aimed at the elucidation of some laws of the propagation and reflection of acoustic waves in paratellurite crystals, which are characterized by unusual features in the behavior of reflected waves [10]. It was expected that investigations of the reflection of acoustic waves in this anisotropic medium would reveal special geometries of the effective acousto-optic interactions, which will provide for the creation of novel devices [5–9].

The features of acoustic wave propagation were studied in paratellurite (TeO_2) samples cut in the form of a rectangular parallelepiped oriented at an angle α relative to the *X* and *Y* axes. The measurements were performed for a crystal cut so that the incident and reflected waves occurred in the *XY* plane. Figure 1 shows the crystal orientation relative to the *X* and *Y* axes and indicates directions of the group and phase velocity

1063-7850/05/3104-0352$26.00 © 2005 Pleiades Publishing, Inc.

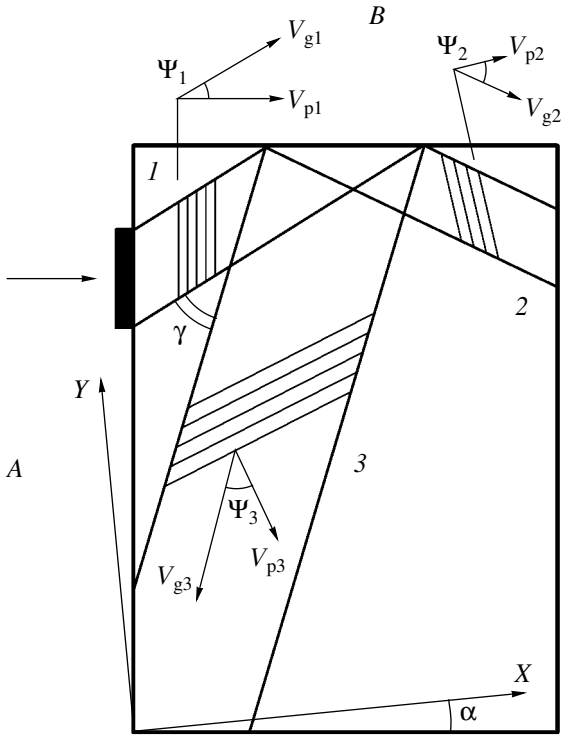

Fig. 1. Schematic diagram showing the reflection of acoustic waves in a paratellurite crystal.

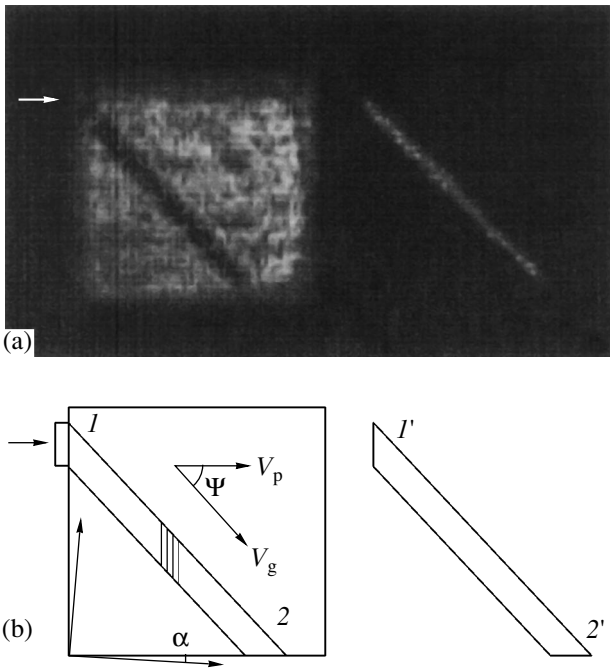

Fig. 2. Imaging of acoustic waves in a TeO_2 crystal (see text for explanations).

of sound (the *Z* axis is perpendicular to the plane of the figure).

A quasi-longitudinal acoustic wave *1* (Fig. 1) was launched into the paratellurite crystal by a lithium niobate piezoelectric transducer fixed on the crystal facet *A*. The acoustical anisotropy of the paratellurite crystal is manifested in that the phase velocity of wave *1* is perpendicular to facet *A*, while the group velocity of this wave makes an angle ψ_1 (acoustic walk-off angle) with the phase velocity. It should be noted that, in the case of the crystal orientation studied, the piezoelectric transducer also launched another wave with the group velocity directed toward the crystal facet opposite to facet *B*. This wave is not involved in the reflection and it is not depicted in Fig. 1. Evidently, the reflection of wave *1* from the crystal facet *B* leads to the appearance of two reflected waves (*2* and *3* in Fig. 1). For wave *2*, the angle between the group (V_{g2}) and phase (V_{p2}) sound velocities is ψ_2; for wave *3*, the angle between the corresponding velocities V_{g3} and V_{p3} is ψ_3. Analysis showed that the angle γ between the energy flows in the reflected acoustic wave *3* and the incident wave *1* can be very small, which makes possible a rather unexpected backward reflection of wave *1*, as is shown in Fig. 1.

The experimental investigation of the reflected acoustic waves was performed by the acousto-optic method of ultrasound imaging, according to which the crystal was illuminated by a broad collimated light beam. The experimental arrangement is schematically shown in Fig. 2b. The measurements were performed on a paratellurite crystal with dimensions $1.8 \times 1.8 \times 0.7$ cm, in which the acoustic wave was propagating in the *XY* plane and the *Z* axis was oriented along the shortest edge. A $Y + 36°$ cut lithium niobate piezoelectric transducer was fixed on a side facet of the crystal by means of cold vacuum welding with an indium solder. The position of the piezoelectric transducer is indicated by the arrow in Fig. 2. The sample crystal was cut so that the transducer plane made an angle of $\alpha = 5°$ relative to the *X* axis. This source excited predominantly a longitudinal component of the acoustic wave in a working frequency range of f = 60–100 MHz. The collimated laser beam with $\lambda = 0.633$ μm was incident onto the sample at angle θ_B, approximately along the *Z* axis of the crystal.

Figure 2a shows photographs of the patterns observed at the output of the crystal; the formation of this image is illustrated by Fig. 2b. The left photograph in Fig. 2a shows the image of the TeO_2 crystal, while the right photograph presents the first-order diffraction pattern. Since the ultrasound energy flux propagated at the angle ψ relative to the acoustic wave front, the diffraction pattern appears as a sloped band repeating the orientation and shape of the sound column in the crystal. As can be seen in Fig. 2a, the light passing through the crystal is in fact diffracted in the +1 order on the inclined sound column, so that point *1* of this column

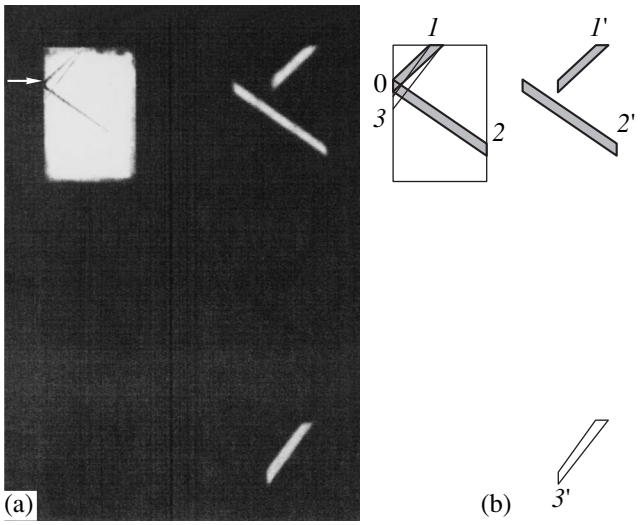

Fig. 3. Imaging of acoustic waves in a TeO_2 crystal (see text for explanations).

corresponds to point *1*' of the diffraction pattern, while point *2* of the sound column corresponds to point *2*' of the diffraction pattern (see Fig. 2b).

As is known, the Bragg angle for the isotropic diffraction is inversely proportional to the phase velocity of the acoustic wave [1–4]:

$$\sin\theta_i = \frac{\lambda f}{2nV}. \quad (1)$$

In acousto-optics, the diffraction angle θ_d is also inversely proportional to the phase velocity of the ultrasound ($\theta_d \sim 1/V$), since $\theta_d = \theta_i$. Therefore, by measuring the angle of light beam deviation and using formula (1), it is possible to determine with a rather high accuracy the phase velocity of sound (V_p) in the crystal [1–4]. The acoustic walk-off angle ψ can be determined from an analysis of the diffraction pattern.

In our experiments, the acoustic walk-off angle between the phase (V_p) and group (V_g) velocities determined directly from the diffraction pattern was $\psi = 47° \pm 2°$, which is in good agreement with the calculated value ($\psi = 46°$). The absolute value of the phase velocity determined using the measured Bragg angle was $V_p = 3.4 \times 10^5$ cm/s (±1%), which also well coincided with the results of calculations ($V_p = 3.45 \times 10^5$ cm/s). Thus, the results of acousto-optic measurements allowed us to determine both the phase velocity of sound (V_p) and the acoustic energy walk-off angle (ψ) in the paratellurite crystal.

The main laws of the backward reflection of acoustic waves in paratellurite single crystals are illustrated in Fig. 3. The experiment was performed in the *XY* plane of the crystal. The acousto-optic cell dimensions in Fig. 3 are 1.8 × 1.2 × 0.7 mm; a lithium niobate piezoelectric transducer was positioned as indicated by the arrow; and the crystal was cut so that the transducer plane made an angle of 5° relative to the *X* axis. The working frequency band of the transducer was f = 120–180 MHz. A broad beam of laser radiation with $\lambda = 0.532$ μm was collimated by a telescope and directed along the *Z* axis of the crystal. The experimental procedure was analogous to that described above (Fig. 2).

The direction of polarization of the intrinsic acoustic modes in the given cut of the TeO_2 crystal does not coincide with the normal to the transducer plane. For this reason, the transducer excited both slow and fast acoustic waves in the crystal. These waves, which can be distinguished in Fig. 3a, are denoted by *1* and *2* in Fig. 3b, illustrating the image formation. Wave *1* has a lower phase velocity as compared to that of wave *2*. Using the experimentally measured Bragg angles for the deviation of waves *1* and *2*, we determined the corresponding phase velocities by formula (1), which yielded $V_{p1} = 2.89 \times 10^5$ cm/s (±1%) and $V_{p2} = 3.44 \times 10^5$ cm/s (±1%). These values well coincide with the results of theoretical calculations: $V_{p1} = 2.88 \times 10^5$ cm/s and $V_{p2} = 3.45 \times 10^5$ cm/s. Using the diffraction pattern presented in Fig. 3a, we also determined the acoustic walk-off angles $\psi_1 = 47° \pm 2°$ (wave *1*) and $\psi_2 = 35° \pm 2°$ (wave *2*). These experimental results for both waves coincide with the calculated values: $\psi_1 = 46°$ and $\psi_2 = 35°$.

As can be seen from Fig. 3, wave *1* is incident onto the upper facet of the paratellurite crystal and, in accordance with Fig. 1, gives rise to two reflected acoustic waves. It was found that the intensity of one of these waves was extremely small as compared to that of the other wave (1 : 100), so that the diffraction of light on this wave was ineffective. The weak wave was detected in experiment, but it is not manifested in the photograph in Fig. 3a because of very low brightness (this wave is also not depicted in Fig. 3b). The stronger reflected wave produced effective light diffraction. This wave is clearly seen in the bottom right angle of Fig. 3a and indicated in Fig. 3b as wave *3*. The phase velocity V_{p3} of this acoustic wave significantly differs from the values of V_{p1} and V_{p2}, which results in a large difference of the Bragg angles for these waves. For this reason, the diffraction field generated by wave *3* is situated at a greater distance from the crystal as compared to the fields of waves *1* and *2*, which is clearly seen in Fig. 3. Using the experimentally measured Bragg angle for the deviation of wave *3*, we determined the corresponding phase velocity of the reflected sound using formula (1), which gave the value $V_{p3} = 1.52 \times 10^5$ cm/s (±1%), practically coinciding with the results of theoretical calculations. Using the photograph of the diffraction pattern, we also determined the angle of spatial separation between the group velocities V_{g1} and V_{g3} for the corresponding waves *1* and *3*. This angle has proved to be $\gamma = 7°$, which almost coincided with the theoretical

value of $\gamma = 7.2°$. Such a small value of this angle confirms the unique backward character of propagation of the reflected wave *3* in the crystal.

Thus, the energy fluxes of the reflected acoustic waves in paratellurite may propagate in rather unexpected directions, which can be determined using the surface of acoustic slow waves of a given material [1, 6–10]. This circumstance has to be taken into account in each particular realization of the acoustic wave reflection in acousto-optic cells [8, 9]. Prototypes of new acousto-optic devices based on paratellurite crystals can be created such that they employ the unique character of the propagation and reflection of acoustic waves in these crystals [9]. For example, the reflection of sound from a large crystal facet can be used in quasi-collinear acousto-optic filters for the insertion of light into the sound column. Investigations of the features of acoustic wave reflection from various crystal facets may also solve the problem of driving the parasitic reflected waves out of the zone of useful acousto-optic interaction. Thus, it is possible to exclude the influence of such parasitic waves on the instrumental function of acousto-optic filters and eliminate the false diffraction maxima.

Acknowledgments. The authors are grateful to V.Ya. Molchanov for his help and useful advice in experiment and for fruitful discussions during the preparation of this paper.

REFERENCES

1. E. Dieulesaint and D. Royer, *Elastic Waves in Solids* (Wiley, New York, 1981).
2. V. I. Balakshiĭ, V. N. Parygin, and L. E. Chirkov, *Physical Principles of Acoustooptics* (Radio i Svyaz', Moscow, 1985) [in Russian].
3. J. Xu and R. Stroud, *Acousto-Optic Devices* (Wiley, New York, 1992).
4. A. Goutzoulis and D. Pape, *Design and Fabrication of Acousto-Optic Devices* (Marcel Dekker, New York, 1994).
5. V. B. Voloshinov, Opt. Eng. **31**, 2089 (1992).
6. C. D. Tran and G.-C. Huan, Opt. Eng. **38**, 1143 (1999).
7. J. Sapriel, D. Charissoux, V. B. Voloshinov, *et al.*, J. Lightwave Technol. **20**, 888 (2002).
8. N. V. Polikarpova and V. B. Voloshinov, Acustica–Acta Acustica **89**, 930 (2003).
9. N. V. Polikarpova and V. B. Voloshinov, Mol. Quantum Acoust. **24**, 225 (2003).
10. M. J. P. Musgrave, Geophys. J. R. Astron. Soc. **3**, 406 (1960).
11. J. C. Kastelik, M. G. Gazalet, C. Drunel, *et al.*, J. Appl. Phys. **74**, 2813 (1993).
12. V. B. Voloshinov, Ultrasonics **31**, 333 (1993).

Translated by P. Pozdeev

Technical Physics Letters, Vol. 31, No. 4, 2005, pp. 356–358. Translated from Pis'ma v Zhurnal Tekhnicheskoĭ Fiziki, Vol. 31, No. 8, 2005, pp. 88–94.

Measuring the Light Beam Intensity Spectrum by Prism Coupling Technique

A. B. Sotsky, A. V. Khomchenko*, A. V. Shul'ga, L. I. Sotskaya, and V. V. Khomchenko

Institute of Applied Optics, National Academy of Sciences of Belarus, Mogilev, Belarus

** e-mail: avkh@physics.belpak.mogilev.by*

Received July 13, 2004; in final form, November 5, 2004

Abstract—A new method for measuring the intensity spectrum of a light beam is proposed, which is based on monitoring the angular dependence of the reflected radiation power in a thin-film structure by prism coupling technique. © *2005 Pleiades Publishing, Inc.*

Integral optical methods of measurement, based on monitoring the spatial distribution of the intensity of radiation reflected from a prism coupler, are usually employed for determining the properties of thin films and media [1, 2]. This paper describes application of the prism coupling technique to measurements of the spatial spectra of the intensity of coherent light beams, which is of key importance for the solution of inverse optical problems [3]. The measurement of such spectra by conventional methods [4–6] is subject to certain limitations related to the aberrations of lens systems [4] or low field intensities [5, 6]. Using the proposed approach, it is possible to lift these limitations by measuring the angular dependence of the total power of a light beam reflected from a prism coupler exciting a planar optical waveguide.

When a planar waveguide is excited via a prism coupler, it is possible to observe the so-called dark *m*-lines in the reflection mode [1]. Figure 1 shows the corresponding angular dependences $S(\gamma)$ of the power of a light beam reflected from a prism coupler in the course of a waveguide mode excitation with the aid of laser beams formed by various optical systems. The substantial differences observed between the $S(\gamma)$ curves obtained when parameters of the same mode are measured using various laser beams suggest a new method for the investigation of light beam characteristics.

Let a planar waveguide be excited by the coherent light beam to be studied (see the inset to Fig.1). The axes of the incident and reflected beams make angles γ relative to the normal to the corresponding side faces of prism *1*. If the exciting light beam is linearly polarized, the distribution of the transverse component of electric field in the plane $Z = 0$ (Fig. 1) can be described as $E_\tau(x, y) = (1 - \chi)\psi(x, y)x + \chi\psi(x, y)y$, where $\chi = 0$ or 1, and x and y are the unit vectors of the coordinate axes. The reflected beam power is measured by photodetector *4*. Denoting by R the characteristic scale of variation of the $\psi(x, y)$ function ($|\nabla\psi| \sim R^{-1}|\psi|$) and taking into account the condition $k_0R \gg 1$ ($k_0 = 2\pi\lambda_0^{-1}$ is the wavenumber of vacuum) usually satisfied in practice, we obtain the following relation for the signal $S(\gamma)$ mea-

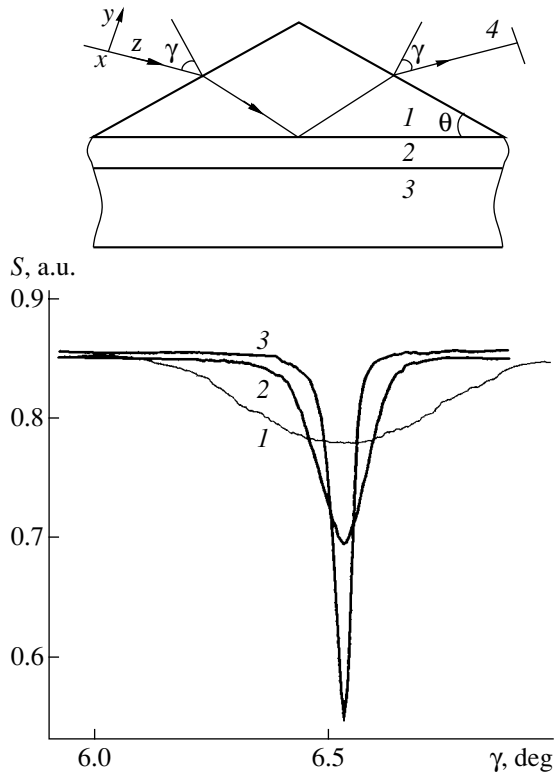

Fig. 1. The $S(\gamma)$ curves measured in a thin-film waveguide structure excited by laser beams with the radii R = 90 (*1*), 140 (*2*), and 450 μm (*3*). The top inset shows a schematic diagram of the measuring device comprising (*1*) a coupling prism, (*2*) a buffer layer, (*3*) a waveguide film, and (*4*) a photodetector.

1063-7850/05/3104-0356$26.00 © 2005 Pleiades Publishing, Inc.

sured by the photodetector under conditions of the resonance waveguide mode excitation [7]:

$$S(\gamma) = T(\gamma)\left\{C_1 + C_2\int_{-\infty}^{\infty} F(\xi)[(\xi+\nu-\gamma)^2+G]^{-1}d\xi\right\}, \quad (1)$$

where C_1 and C_2 are the coefficients dependent on the efficiency of prism coupling to the waveguide and the instrumental constant of the photodetector,

$$T(\gamma) = 16[(1-\chi)(q_1q_2)^2(q_1+q_2)^{-4} + \chi(q_1q_2\varepsilon_p\varepsilon_a)^2(q_1\varepsilon_a+q_2\varepsilon_p)^{-4}],$$

$$F(\xi) = \int_{-\infty}^{\infty}\left|\hat{\psi}(n_x, \sqrt{\varepsilon_a}\sin\xi\right|^2 dn_x,$$

$$q_1 = \sqrt{\varepsilon_p - \varepsilon_a\sin^2\gamma}, \quad q_2 = \sqrt{\varepsilon_a}\cos\gamma,$$

$$\hat{\psi}(n_x, \sqrt{\varepsilon_a}\sin\xi) = \int\int_{-\infty}^{\infty} dxdy\exp(ik_0xn_x + ik_0y\sqrt{\varepsilon_a}\sin\xi)\psi(x,y),$$

$$\nu = \arcsin[\sin\theta\sqrt{\varepsilon_p\varepsilon_a^{-1} - (\mathrm{Re}h)^2(k_0\varepsilon_a)^{-1}} - \cos\theta\mathrm{Re}h(k_0\sqrt{\varepsilon_a})^{-1}],$$

$$N = \sqrt{\varepsilon_p}\cos\nu \times[\cos\theta + \sqrt{\varepsilon_a}\sin\nu\sin\theta(\varepsilon_p - \varepsilon_a\sin^2\nu)^{-0.5}],$$

$$G = [\mathrm{Im}h(k_0N)^{-1}]^2.$$

ε_p and ε_a are the permittivities of the prism and ambient medium, respectively; θ is the angle at the prism base (Fig. 1); h is the complex propagation constant of the leaky mode in the waveguide–prism structure; and ξ is the angular coordinate to which the light beam intensity in the xy plane is related.

The function $F(\xi)$ in relation (1) is defined using the square modulus of the Fourier image $\hat{\psi}(n_x, \sqrt{\varepsilon_a}\sin\xi)$ of the exciting beam. If this Fourier image can be represented as $\hat{\Psi}(x, y) = X(x)Y(y)$, the spectrum of the beam intensity is readily obtained by reconstructing two functions $F(\xi)$ corresponding to the parameter $\chi = 0$ and 1. This situation is characteristic of laser beams and fields of emission from the edge of an optical waveguide. In such cases, it is necessary to perform two sequential measurements for the waveguide mode excited by the beams incident in the mutually perpendicular planes. Then, according to relation (1),

$$F(\xi) = \frac{\sqrt{G}}{2\pi^2C_2}\int\int_{-\infty}^{\infty} dkd\gamma \times\exp[\sqrt{G}|k| + ik(\gamma-\nu-\xi)]\left[\frac{S(\gamma)}{T(\gamma)} - C_1\right]. \quad (2)$$

The distribution $S(\gamma)$ is measured for discrete values of the angle $\gamma = \gamma_j$ ($j = 1, 2, \ldots, m$). Therefore, the integral in formula (2) can be calculated using the interpolation

$$S(\gamma)[T(\gamma)]^{-1} = C_1 + \sum_{l=0}^{n} A_l \times\exp\{-0.5[(\gamma-\gamma_1)V^{-1}]^2\}H_l[(\gamma-\gamma_1)V^{-1}],$$

where γ_1 is the coordinate of the minimum of the function $S(\gamma)$, $H_l[(\gamma-\gamma_1)V^{-1}]$ is the Hermitian polynomial, and C_1, A_l, and V are the constants determined (for a given interpolation order n) by least squares using the measured values of $S(\gamma_j)$. Using formula (2), we eventually obtain

$$F(\xi) = \frac{V\sqrt{2\pi G}}{2\pi^2C_2}\int_{-\infty}^{\infty} dk\sum_{l=0}^{n} A_l(i)^lH_l(kV) \times\exp[\sqrt{G}|k| - 0.5(kV)^2 + ik(\gamma_1-\nu-\xi)]. \quad (3)$$

Since the factor at the integral and the differences $\gamma_1 - \nu$ in the integrand of (3) influence only the normalization of the function $F(\xi)$ and the shift of the coordinate ξ, the information about the measuring device required a priori for the measurement of the intensity spectrum reduces to setting the complex propagation constant h of the excited mode.

The results of verification of the above procedure developed for reconstruction of the function $F(\xi)$ through calculation of the $S(\gamma)$ distribution for various beams in the course of solution of the electrodynamic vector problem [8] showed a high efficiency of the proposed algorithm. It should be noted that the function $\exp[-0.5(kV)^2]$ in expression (3) plays the role of a stabilizing factor, which ensures stability of the function $F(\xi)$ with respect to the noise involved in the determination of $S(\gamma_j)$ values [9]. In particular, the error of reconstruction of the $F(\xi)/F_{max}$ ratio in a 30 dB range with $n = 6$ for Gaussian beams did not exceed 0.1%.

Using the developed approach, we have successfully measured the spectra of spatial frequencies of laser beams formed in various optical systems. The measuring devices had the form of thin-film structures

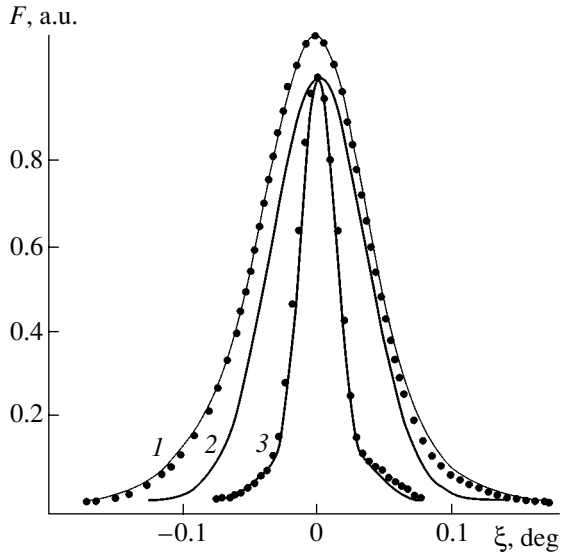

Fig. 2. Angular dependence of the intensity of laser beams with the radii R = 90 (*1*), 140 (*2*), and 450 μm (*3*) reconstructed from the corresponding $S(\gamma)$ curves presented in Fig. 1. Points at the curves *1* and *3* show the experimental data obtained independently by means of the Fourier optics.

obtained by the RF sputter deposition of a waveguide film onto the prism base preliminarily covered by a buffer layer of quartz glass. The measurements of $S(\gamma)$ were performed using a setup described previously [7]. The Gaussian beam of an He–Ne laser with λ = 632.2 nm was incident onto a coupling prism mounted on a rotating table. The optical system allowed light beams with various angular distributions of intensity to be obtained. The angle of beam incidence onto the prism was varied with the aid of a step motor drive that changed the table rotation angle with a step of 9.7×10^{-5} rad. The angular dependence of the reflected light beam power was measured using a photodetector synchronously driven with the aid of another step motor. This detector measured the power of the light beam reflected from the prism coupler at a given angle of incidence, while another detector measured the power of the incident beam. The step motor control unit was synchronized with the channel comparator. The measured signals were digitized and stored in a computer memory. The complex mode propagation constant of the measuring device was preliminarily determined [8] using a laser beam with known intensity spectrum and radius, which yielded $h/k_0 = 1.46623 - i2.96 \times 10^{-6}$.

Figure 2 shows the typical intensity spectra of the beams corresponding to the measured $S(\gamma)$ curves presented in Fig. 1. The correctness of these results was confirmed by comparison with the values obtained using direct photometry in the focal plane of a long-focus (f = 30 cm) objective [4], which are plotted by points in Fig. 2. A comparative analysis of these data shows satisfactory correlation of the results obtained by the two independent methods. The efficiency of the proposed method is illustrated by the results of measurements of the intensity spectrum of a laser beam with the shape deviating from Gaussian (Fig. 2, curve *3*). As can be seen, the proposed approach reveals rather slight changes in the intensity spectra of laser beams and ensures a higher resolution as compared to that provided by the method of Fourier optics, while retaining the required precision. This advantage is especially pronounced in the case of weakly divergent laser beams (Fig. 2, curve *3*).

To summarize, we proposed a new method for measuring the intensity spectrum of a light beam; this method is based on monitoring the angular dependence of the reflected radiation power in a thin-film structure by prism coupling technique. This method can be used for laser beam monitoring and the measurement of the parameters of radiation sources, as well as of optical fibers and waveguides.

REFERENCES

1. P. R. Tien, R. Ulrich, and R. J. Martin, Appl. Phys. Lett. **14**, 291 (1969).
2. S. Monneret, P. Huguet-Chant, and F. Flory, J. Opt. A: Pure Appl. Opt. **2**, 188 (2000).
3. H. P. Baltes, *Inverse Source Problems in Optics* (Springer-Verlag, Berlin, 1978).
4. *Applications of Optical Fourier Transforms* (Academic, New York, 1982).
5. W. Freude and A. Sharma, J. Lightwave Technol. **3**, 628 (1985).
6. N. Gisin, R. Passy, and B. Perny, J. Lightwave Technol. **11**, 1875 (1993).
7. A. V. Khomchenko, A. B. Sotskiĭ, A. A. Romanenko, *et al.*, Pis'ma Zh. Tekh. Fiz. **28** (11), 51 (2002) [Tech. Phys. Lett. **28**, 467 (2002)].
8. A. B. Sotskiĭ, A. A. Romanenko, A. V. Khomchenko, *et al.*, Radiotekh. Élektron. (Moscow) **44**, 687 (1999).
9. A. N. Tikhonov and V. Ya. Arsenin, *Solutions of Ill-Posed Problems* (Nauka, Moscow, 1979; Halsted Press, New York, 1977).

Translated by P. Pozdeev